
Doctoral Dissertations

Student Theses and Dissertations

Spring 2017

Repair of metallic components using hybrid manufacturing

Renwei Liu

Follow this and additional works at: https://scholarsmine.mst.edu/doctoral_dissertations



Part of the [Mechanical Engineering Commons](#)

Department: Mechanical and Aerospace Engineering

Recommended Citation

Liu, Renwei, "Repair of metallic components using hybrid manufacturing" (2017). *Doctoral Dissertations*. 2747.

https://scholarsmine.mst.edu/doctoral_dissertations/2747

This thesis is brought to you by Scholars' Mine, a service of the Missouri S&T Library and Learning Resources. This work is protected by U. S. Copyright Law. Unauthorized use including reproduction for redistribution requires the permission of the copyright holder. For more information, please contact scholarsmine@mst.edu.

REPAIR OF METALLIC COMPONENTS USING HYBRID MANUFACTURING

by

RENWEI LIU

A DISSERTATION

Presented to the Faculty of the Graduate School of the
MISSOURI UNIVERSITY OF SCIENCE AND TECHNOLOGY

In Partial Fulfillment of the Requirements for the Degree

DOCTOR OF PHILOSOPHY

in

MECHANICAL ENGINEERING

2017

Approved
Dr. Liou, Frank, Advisor
Dr. Bristow, Douglas
Dr. Midha, Ashok
Dr. Newkirk, Joseph W
Dr. Pan, Heng

© 2017

Renwei Liu

All Rights Reserved

PUBLICATION DISSERTATION OPTION

This dissertation consists of the following three articles that have been published or submitted for publication as follows:

Pages 6-58 are intended for submission to the Journal of Manufacturing Science and Engineering, ASME.

Pages 59-87 have been accepted for publication for 2016 Annual International Solid Freeform Fabrication Symposium and are intended for submission to Rapid Prototyping Journal.

Pages 88-111 have been accepted for publication in Rapid Prototyping Journal.

All of them have been prepared in the Missouri University of Science and Technology dissertation format.

ABSTRACT

Many high-performance metal parts users extend the service of these damaged parts by employing repair technology. Hybrid manufacturing, which includes additive manufacturing (AM) and subtractive manufacturing, provides greater build capability, better accuracy, and surface finish for component repair. However, most repair processes still rely on manual operations, which are not satisfactory in terms of time, cost, reliability, and accuracy. This dissertation aims to improve the application of hybrid manufacturing for repairing metallic components by addressing the following three research topics. The first research topic is to investigate and develop an efficient best-fit and shape adaption algorithm for automating 3D models' the alignment and defect reconstruction. A multi-feature fitting algorithm and cross-section comparison method are developed. The second research topic is to develop a smooth toolpath generation method for laser metal deposition to improve the deposition quality for metallic component fabrication and repair. Smooth connections or transitions in toolpath planning are achieved to provide a constant feedrate and controllable deposition idle time for each single deposition pass. The third research topic is to develop an automated repair process could efficiently obtain the spatial information of a worn component for defect detection, alignment, and 3D scanning with the integration of stereo vision and laser displacement sensor. This dissertation investigated and developed key technologies to improve the efficiency, repair quality, precision, and automation for the repair of metallic components using hybrid manufacturing. Moreover, the research results of this dissertation can benefit a wide range of industries, such as additive manufacturing, manufacturing and measurement automation, and part inspection.

ACKNOWLEDGMENTS

First and foremost, I would like to express my sincere gratitude to my advisor, Dr. Frank Liou, for his encouragement, insightful guidance, and support during my Ph.D. study at Missouri University of Science and Technology. His diligence and rigorous attitude to research and work will have a significant influence on my life. It has been a privilege and a great honor to have worked with him.

I would also like to extend my appreciation to all my dissertation committee members, Dr. Ashok Midha, Dr. Douglas A. Bristow, Dr. Heng Pan, and Dr. Joseph W Newkirk. Without their guidance and valuable comments, it would have been impossible for me to complete my dissertation.

This dissertation was supported by the Laser Aided Manufacturing Processes (LAMP) Laboratory, and the Intelligent System Center of Missouri S&T, which are gratefully acknowledged.

I would like to express my deep thanks to my lab-mates and friends, Mr. Todd Sparks, Mr. Zhiyuan Wang, Mr. Max Mulholland, Mr. Jingwei Zhang, Mr. Sreekar Karnati, Mr. Lei Yan, Mr. Muqian Wu, Mr. Yunlu Zhang, Ms. Xueyang Chen, and Mr. Xinchang Zhang, for their support during my study in Rolla.

Last but not the least, I wish to extend my special and sincere thanks to my parents, Mr. Jianghua Liu and Ms. Fengying Guo, my fiancée, Flora Feng, and all my family members for their love and unwavering support.

TABLE OF CONTENTS

	Page
PUBLICATION DISSERTATION OPTION.....	iii
ABSTRACT	iv
ACKNOWLEDGMENTS	v
LIST OF ILLUSTRATIONS	ix
LIST OF TABLES	xii
 SECTION	
1. INTRODUCTION.....	1
1.1. BACKGROUND.....	1
1.2. RESEARCH OBJECTIVES	2
1.3. ORGANIZATION OF DISSERTATION.....	4
 PAPER	
I. MULTI-FEATURE FITTING AND SHAPE ADAPTION ALGORITHM FOR COMPONENTS REPAIR	6
ABSTRACT	6
1. INTRODUCTION.....	8
2. RELATED WORKS	10
3. METHODOLOGY	14
3.1. RIGID BODY BEST-FIT	14
3.2. CROSS-SECTIONS AND FEATURES CONSTRUCTION.....	15
3.3. MULTI-FEATURE FITTING ALGORITHM	17
3.3.1. Least Square Method	20
3.3.2. Density-based Outlier Detection.....	23

3.3.3. An Example of Feature-fitting Processes.....	24
3.4. SHAPE ADAPTION ALGORITHM	30
3.4.1. Cross-section Comparison.....	31
3.4.2. Defect Reconstruction.....	34
4. ILLUSTRATIVE EXAMPLES	38
4.1. ILLUSTRATIVE EXAMPLES FOR BROKEN COMPONENTS	38
4.2. ILLUSTRATIVE EXAMPLES FOR DEFORMED COMPONENTS....	46
5. CONCLUSION.....	53
ACKNOWLEDGMENT	55
REFERENCE	56
II. A SMOOTH TOOLPATH GENERATION METHOD FOR LASER METAL DEPOSITION	59
ABSTRACT	59
1. INTRODUCTION.....	60
2. RELATED WORKS	64
3. METHODOLOGY	67
3.1. PROBLEM DEFINITION AND SOLUTION.....	67
3.2. SMOOTH TOOLPATH EXAMPLES	70
4. EXPERIMENTS	73
4.1. VIBRATION TEST.....	73
4.2. LASER METAL DEPOSITION EXPERIMENT.....	76
4.3. MICROSTRUCTURE STUDY	79
5. CONCLUSION.....	83
ACKNOWLEDGMENTS	84

REFERENCES	85
III. STEREO VISION-BASED REPAIR OF METALLIC COMPONENTS	88
ABSTRACT	88
1. INTRODUCTION.....	90
2. METHOD AND PROCESS	94
2.1. OVERVIEW OF AUTOMATED COMPONENT REPAIR PROCESS	94
2.2. STEREO VISION AND CALIBRATION	95
2.3. AUTOMATED DEFECT DETECTION AND ALIGNMENT	98
2.4. ADAPTIVE TOOL PATH GENERATION.....	101
3. EXPERIMENTS	103
3.1. EXPERIMENT SETUP AND RESULT	103
3.2. MICROSTRUCTURE STUDY OF REPAIRED SAMPLES	106
4. CONCLUSIONS AND FUTURE WORK.....	108
ACKNOWLEDGMENT	109
REFERENCE	110
SECTION	
2. CONCLUSION.....	112
VITA	115

LIST OF ILLUSTRATIONS

SECTION	Page
Figure 1.1 Framework of this dissertation	5
PAPER I	
Figure 3.1 Rigid body best-fit	15
Figure 3.2 Cross-sections and features construction	18
Figure 3.3 An example of 2D polygon	19
Figure 3.4 Multi-feature fitting algorithm	20
Figure 3.5 The initial spatial relationship of nominal and worn model's features.....	26
Figure 3.6 An example of feature-fitting algorithm based on least-square and density-based outlier-detection	27
Figure 3.7 The results of using feature-fitting algorithm	30
Figure 3.8 Stages of shape adaption algorithm	32
Figure 3.9 'Point-line-surface' cross-section comparison processes	34
Figure 3.10 An example of cross-section comparison and fracture surface construction.....	35
Figure 3.11 Vertices dilation for fracture surface boundary	36
Figure 3.12 An example of fracture surface boundary dilation	36
Figure 3.13 Mesh trim in Rhino for defect reconstruction	37
Figure 3.14 Mesh trim result for the example of a cone shape	37
Figure 4.1 Bearing house model and cross-sections with features.....	40
Figure 4.2 Model level's feature-fitting for 1D feature—Bearing house	41
Figure 4.3 Cross-section level's feature-fitting—Bearing house.....	41
Figure 4.4 Shape adaption algorithm—Bearing house.....	42
Figure 4.5 Fracture surface dilation—Bearing house.....	42

Figure 4.6 Mesh trim and defect reconstruction—Bearing house	43
Figure 4.7 Curved bladed model, adaptive slicing and feature construction	48
Figure 4.8 Multi-feature fitting results	48
Figure 4.9 Fracture surface construction on nominal blade model	49
Figure 4.10 Fracture surface construction on deformed blade model	49
Figure 4.11 Intersection surface on nominal blade	50
Figure 4.12 Intersection surface on deformed blade	50
Figure 4.13 Intersection surface trim fracture surface on deformed blade	51
Figure 4.14 Intersection surface trim fracture surface on original blade	51
Figure 4.15 Defect reconstruction result for deformed geometry	52

PAPER II

Figure 1.1 Two main toolpath planning strategies in AM	63
Figure 1.2 Feedrate change at turning/corner points	63
Figure 3.1 Problem definition of discontinuous toolpath in AM	68
Figure 3.2 Smooth toolpath pattern for laser metal deposition	71
Figure 3.3 Contour toolpaths by smooth transition with different curve size	71
Figure 3.4 Optimized toolpath using smooth toolpath generation for repair	72
Figure 4.1 The layout of vibration test system	74
Figure 4.2 Tool path for vibration test	74
Figure 4.3 Acceleration measurement plot	75
Figure 4.4 Schematic of the MST-LAMP LMD system	77
Figure 4.5 Experimental results by smooth toolpath generation for laser metal deposition	78
Figure 4.6 Repair experimental results	79

Figure 4.7 View angle for samples	80
Figure 4.8 Sample microstructure of the repaired part	81
 PAPER III	
Figure 2.1 A hybrid manufacturing system: Additive manufacturing and CNC machining	94
Figure 2.2 Process of automated component repair	96
Figure 2.3 Principle of stereo vision.....	97
Figure 2.4 Chessboard viewing at different angels and distances by stereo vision camera with founded corners for calibration	98
Figure 2.5 Automated defect detection in camera coordinate system.....	100
Figure 2.6 Precise scanning with laser displacement sensor and the scanned point cloud of defect area	102
Figure 2.7 Adaptive tool path generation: convex hull extraction of point cloud and raster tool path generation	102
Figure 3.1 Stereo vision-based hybrid manufacturing system.....	104
Figure 3.2 Ti-6Al-4V component be closed in shielding gas mounted on the hybrid manufacturing system.....	105
Figure 3.3 Experimental results by stereo vision-based hybrid manufacturing repair process	105
Figure 3.4 Repaired sample for microstructure study	106
Figure 3.5 Microstructure study of repaired samples.	107

LIST OF TABLES

SECTION	Page
PAPER I	
Table 4.1 Multi-feature fitting and shape adaption algorithm for broken parts.....	44
PAPER II	
Table 4.1 Acceleration measurement result	76
Table 4.2 Parameters for patch deposition.....	78
Table 4.3 Parameters for repair experiment.....	79
PAPER III	
Table 2.1 An example of circle centers detection and 3D measurement by stereo vision	99
Table 3.1 Parameters for laser metal deposition and milling experiment for Ti-6Al-4V component repair	105

SECTION

1. INTRODUCTION

1.1.BACKGROUND

High-performance components such as compressors, blisks, turbines, blades, and airfoils are very expensive because they are typically made from high-value materials (i.e., Ti-6Al-4V and Inconel 718) and involve complex processing during manufacturing. Metallic components may be subject to corrosion, impacts, variable thermal cycles and stresses, or other conditions that could cause defects or cracking during the service life. Fatigue and stress cracks are common initiators of failures that cause high-performance and high-value components to be scrapped. Defects may also occur during the manufacturing process such as milling ball indentation, cutter pull out, etc. Because of the extreme cost of materials and labor for fabricating high-value components, it is necessary to repair those components instead of replacing them. Conventionally, the welding process has been used for repair such as tungsten inert gas (TIG) welding, plasma transferred arc (PTA) welding, electron beam (EB) welding, high velocity oxyfuel (HVOF) thermal spraying technique, and etc. The problems of conventional welding processes and thermal spraying techniques do not allow to control of the deposit of exact materials with low input heat to melt and bond materials to the base metal. Compared with the conventional welding repairing technologies, AM has unique capabilities including low heat input, small heat-affected zone, free-form fabrication, near-net-shape, and so on. Some components such as distortion sensitive components or components made by “non-weldable” materials that previously had to be scrapped because of the lack of a suitable repair technique can now be repaired with AM. Hybrid manufacturing, which includes additive manufacturing (AM)

and subtractive manufacturing, provides greater build capability, better accuracy, and surface finish by combining the benefits of both processes.

Even though hybrid manufacturing provides great capability for free-form fabrication, every repair case is unique. There are different kinds of defects including cracks, corroded surfaces, worn-out surfaces, dents, broken parts, and deformations, depending on the service environment. Meanwhile, there are different kinds of worn components such as turbine blades, compressors, airfoils, molds/dies. The location and geometry of the worn area is even arbitrary for the same kinds of components, and part-to-part variation may occur because of an inaccurate clamping position and different manufacturing tolerances. The uniqueness of each repair case brings challenges to worn component model's alignment, defect reconstruction, toolpath generation and the repair processes automation. Currently, most repair processes still rely on manual operation. Manual operation is not only labor intensive but it is also not satisfactory in terms of time, cost, reliability, and accuracy. This dissertation investigates the key methodologies to improve the use of hybrid manufacturing for repairing metallic components.

1.2.RESEARCH OBJECTIVES

The main objective of this dissertation is to investigate the key technologies to apply and improve hybrid manufacturing processes for metallic component repair. Three tasks are carefully studied to achieve the overall objective.

The objective of the research task one is to reconstruct the defect geometry. Because the geometry of worn components is different and every defect geometry is unique, it is a challenging and important task to develop an efficient and robust algorithm for defect

reconstruction. Actually, there are two sub-tasks for task one. The first subtask is to best-fit the worn component model and its nominal model. Another subtask is to develop the shape adaption algorithm to reconstruct the defect geometry. The focus of research task one is to investigate and develop a general best-fit and shape adaption algorithm for automating the alignment and defect reconstruction for components repair. A multi-feature fitting algorithm is proposed to extract the geometric features to align the 3D worn component and its nominal model. Based on the best-fitted model, a ‘point-line-surface’ fracture surface detection method is proposed to construct the fracture surface, and the surface boundary is dilated to trim the nominal model to obtain defect geometry.

The second research task is to develop a smooth toolpath generation method for laser metal deposition to improve the deposition evenness for metallic component fabrication and repair. The conventional contour and zigzag toolpath pattern for laser metal deposition are not smooth at turn points or corner points. The unsmooth toolpath causes uneven deposition, which brings height variation and porosity problems. A parametric curve equation based on three trigonometric functions is derived and built for arbitrary smooth connections or transitions in toolpath planning and provides constant feedrate for deposition. With the smooth toolpath, deposition idle time is also controlled for each single deposition pass to obtain an even temperature during the whole deposition process.

After worn area modeling and toolpath generation, the third research task is to develop an automated repair process that integrates the hybrid manufacturing process using direct laser metal deposition, CNC machining, and in-process scanning to repair metallic components automatically. The automated repair system could efficiently obtain the spatial

information of a worn component for defect detection, alignment, and 3D scanning with the integration of stereo vision and a laser displacement sensor.

The outcomes of the above research tasks are expected to advance the knowledge of applying and improving hybrid manufacturing processes for metallic component repair. The technical developments may benefit not only the area of component repair using hybrid manufacturing, but also other areas such as additive manufacturing, manufacturing and measurement automation, and part inspection.

1.3.ORGANIZATION OF DISSERTATION

In this dissertation, three major research and developments are presented and organized as shown in Fig. 1.1. These three papers cover three stages of the component repair: worn area modeling, path planning, and system integration and automation. Paper I focuses on the best-fit and shape adaption algorithm design and development for defect reconstruction. This paper presents the principles, methodologies and implementation of a new multi-feature fitting algorithm for best-fit and a cross-section comparison algorithm for defect reconstruction. After defect geometry reconstruction, the next stage is toolpath generation for repair. Paper II aims to develop a smooth toolpath generation method for laser metal deposition to improve the deposition quality for metallic component repair and direct metallic component fabrication. General problem definition is investigated and smooth toolpath solution is derived and built. Paper III aims to investigate repair system integration and automation using hybrid manufacturing. A stereo vision-based hybrid (additive and subtractive) manufacturing process using direct laser metal deposition, CNC machining, and in-process scanning to repair metallic components automatically. The

focus of this task is to realize automated alignment between the workpiece and hybrid manufacturing system and adaptive tool path generation that can repair metallic components after a single setup.

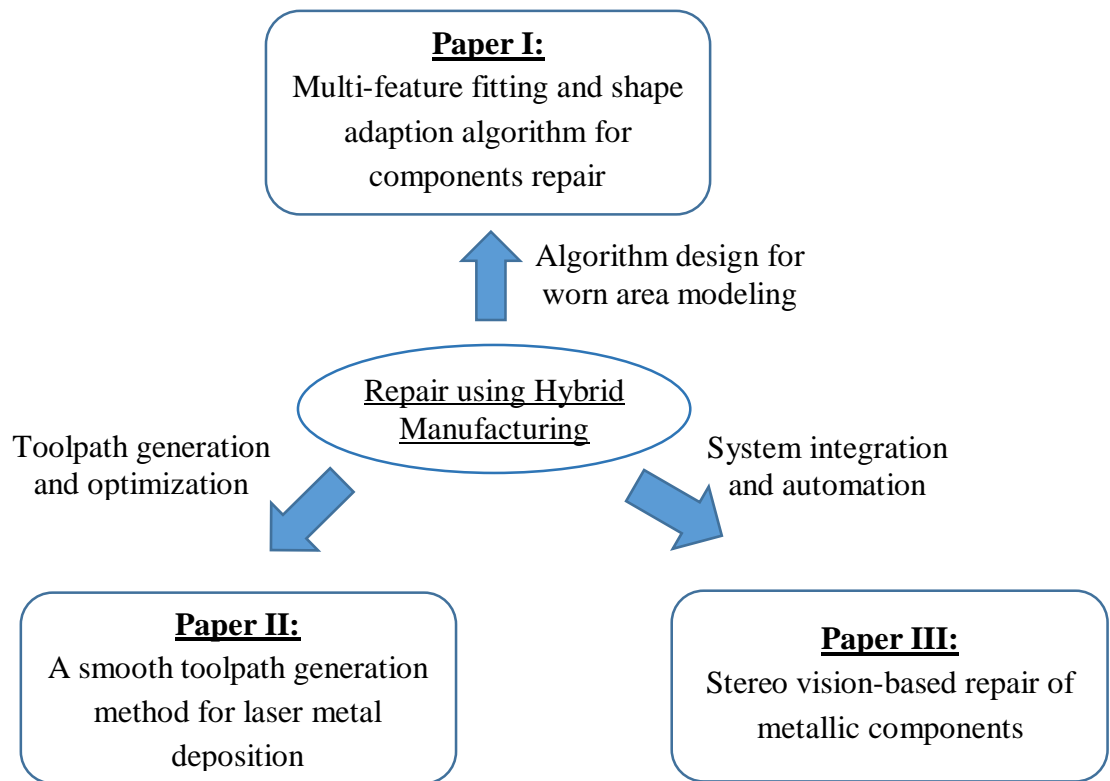


Figure 1.1 Framework of this dissertation

PAPER

I. MULTI-FEATURE FITTING AND SHAPE ADAPTION ALGORITHM FOR COMPONENTS REPAIR

Renwei Liu, Zhiyuan Wang, Todd Sparks, Frank Liou

Department of Mechanical and Aerospace Engineering,
Missouri University of Science and Technology, Rolla, Missouri 65409

ABSTRACT

In recent years, the usage of additive manufacturing (AM) provides new capabilities for component repair, which include low heat input, small heat-affected zone, freeform near-net-shape fabrication. Because the geometry of each worn component is unique, automated repair processes is a challenging and important task. The focus of this paper is to investigate and develop a general best-fit and shape adaption algorithm for automating the alignment and defect reconstruction for components repair. The basic principle of using features for rigid-body best-fitting is analyzed and a multi-feature fitting method is proposed to best-fit the 3D mesh model of a worn component and its nominal component. Depending on the geometry, model level's feature fitting can work solely or be combined with cross-section level's feature fitting to align the worn component model and its nominal model using features from the cross-sections of the 3D model. Since the features from the defect area will disturb the feature-fitting result when applying the least-square method, the feature-fitting algorithm in this paper couples the least-square method

and a density-based outlier detection method. These two methods run alternately to gradually approach the best-fit result and eliminate the disturbance caused from the defect geometry. The shape adaption algorithm is used to do cross-section comparison and defect reconstruction based on the best-fitted 3D model. A ‘point-line-surface’ fracture surface detection method is proposed to construct fracture surface and the fracture surface boundary is dilated to trim the nominal 3D model to obtain defect geometry. Illustrative examples with typical components and different kinds of defects are used to demonstrate the flexibility and capability of using multi-feature fitting and shape adaption algorithm developed in this paper. For broken components, different feature-fitting strategies are used for symmetric components such as the bearing house model and turbine rotor model, and for non-symmetric components such as bracket. For the deformed geometry, adaptive slicing is used for the curved blade feature construction. The adaptive slicing can be potentially used for the non-complete geometry’s feature construction. As for the shape adaption, intersection surface on the nominal model and deformed model is used to obtain the deformed geometry and missed geometry for defect reconstruction.

Keywords: Multi-feature Fitting, Shape Adaption, Best-fit, Repair, Additive Manufacturing

1. INTRODUCTION

Parts machined from high-performance metals are very expensive (e.g., titanium alloys and nickel-based alloys), especially large and high-performance materials. Many users of high-performance metal parts, such as the aerospace industry, the mold/die casting industry, and heavy machinery consumers, extend the service of these damaged parts by employing repair technology. Conventional technologies for repairing metallic components are welding-based processes and thermal spraying techniques such as tungsten inert gas [1], electron beam welding [2], high velocity oxyfuel thermal spraying [3]. However, conventional repair techniques cannot deposit exact material to the worn area, and they produce a lot of heat and cause high residual stresses, distortion and heat-related effects in the base metal. AM has unique capabilities such as low heat input, a small heat-affected zone, free-form fabrication, and a near-net-shape. Some components such as distortion sensitive components or components made by “non-weldable” materials that previously had to be scrapped because of the lack of a suitable repair technique can now be repaired with AM [4]. However, most of the repair processes rely on manual operations that are not satisfactory in terms of time, cost, reliability, and accuracy [5].

Automated worn area modeling is a main focus in the automated repair process. Because the geometry and location for each worn component is unique, even the types of defects vary from part to part. Current reverse engineering (RE) software cannot solve worn area modeling satisfactorily [6]. After scanning the worn component, the RE software packages [7-11] can transfer digitized data into triangular meshes, reconstructed surface models, or reconstructed 3D solid models. However, worn area modeling requires the nominal CAD model of the original part to be compared to the actual worn component

model so that the minimum steps of depositing and machining can be calculated. In general, worn area modeling can be divided into two steps [5, 12]:

- Best-fit is performed to determine the correlation between the nominal position of the nominal CAD model and the actual model of the worn component. Mathematically, the best-fit algorithms determine the transformation rule for rigid body transformations consisting of translation and rotation in a 3D space. Because the shapes of the nominal part and the actual worn part differ significantly, the best-fitted parts are not ideal matches but are positioned as close as possible.
- Shape adaption is performed to determine the correlation between the nominal shape of the nominal CAD model and the actual model of the worn component. The purpose of shape adaption algorithms is to extract and reconstruct the worn area's geometry after best-fit for adaptive NC paths.

2. RELATED WORKS

The challenge for worn area modeling brings from the uniqueness of each repair case. There are defects such as cracks, corroded surfaces, worn out surfaces, dents, broken parts, and deformations, depending on the service environment. Meanwhile, there are various kinds of worn components, such as turbine blades, compressors, airfoils, and molds/dies. The location and geometry of the worn area is even arbitrary for the same kinds of components, and part-to-part variation may occur due to an inaccurate clamping position and different manufacturing tolerances. Because the geometry of worn components is different and every defect geometry is unique, the main focus for worn area modeling is to develop an efficient and robust algorithm for best-fit and shape adaption.

Zheng [13, 14] proposed a strategy to capture the geometry of the worn area by comparing the point cloud of the worn part with its nominal CAD model. A point-to-surface-best-fit method was adopted to fit the measured point cloud of a worn part with the nominal CAD model surface. The boundary of the worn area was extracted and represented by a polygon to trim the nominal surface and obtain get the worn area's geometry. Finally, a triangular mesh of the worn area's geometry was created to generate an STL file for repair. Avagyan [15] developed a shape-matching approach to search the database for related or identical parts with the purpose of extracting worn area information for repair. It is assumed that a reconstructed worn component model is an input to the system, and a matching algorithm based on the statistical similarity estimation was used to identify candidate models from the database. A viewpoint algorithm was used for the best-fit algorithm to obtain the transformation matrix. A triangle similarity comparison was adopted for the shape comparison algorithm to extract the worn area's geometry. Recently, efforts have

been made towards creating a nominal model directly from the scanned geometry of the worn component for use as the reference model for worn area modeling. Those methods are specifically aimed at repairing gas turbine blades and compressor blades. Because blades are normally made using a casting process, each part has a unique geometry due to small variations in the manufacturing process such as tolerances and in-use damage [16, 17]. Gao et al. [18-21] proposed a defects-free model-based repair strategy to solve the worn area modeling problem for turbine blades. A defect-free polygonal model was obtained by a surface extension method and can be used as nominal geometry to extract the worn area's geometry in [18]. The reconstruction method in [21] resolves this issue by sweeping a surface across the defective region. The sweep is based on the cross-sections lying immediately outside. Because blade geometry is primarily dictated by the cross-section geometry along the longitudinal axis of the blade surface, the sweeping method makes sense for reconstructing its nominal model. The method in [19, 20] reconstructs the actual worn component by fitting a surface that conforms to the blade body over the defective region using the RE software package. Piya [22] adopted the sectional Gauss map concept to generate a series of prominent cross sections (PCS) along the longitudinal axis and then reconstructed the damaged blade surface by interpolation. The intrinsic geometry of the PCS lying in the non-defective region is then extrapolated across the defective region to fill in the voids. A Boolean difference between the original defective model and the final reconstructed model yields a fully parameterized geometric representation of the repair volume. He and Li [23] developed a curved surface extension approach to construct a three-dimensional shape of the worn area in blades using a CCD camera measurement system.

The best-fit approaches used in previous studies did not consider the geometric characteristics of components for geometry reasoning, which makes the best-fit algorithm trivial and inefficient. And point cloud or geometry of defect area also disturbs best-fit result. General observation shows that broken parts and nominal parts share the same geometrical features such as the cross-sectional centroid, or convex-hull centroid in the non-defective area. The transformation matrix obtained from best-fitting these features can be used to best-fit the worn component model and the nominal component model. Since the features from the defective area disturb the best-fit result, this paper proposes a multi-feature fitting algorithm that couples a least-square method and a density-outlier-detection method for best-fit and defect detection. Compared to the ‘point-to-surface’ best-fit [13] or ‘triangle-to-triangle’ best-fit approach [15] in previous researches, the multi-feature fitting algorithm is much more efficient. The shape adaption algorithm is then used to do cross-section comparison and defect reconstruction based on the best-fitted 3D model. The cross-section comparison method detects the fracture segments of the defect area and constructs the fracture surface. Finally, the fracture surface is dilated to trim the nominal model to obtain the accurate defect geometry.

Because RE software packages are widely available for transferring digitized data into triangular meshes, reconstructed surface models, or reconstructed 3D solid models [9-11]. In this paper, it is assumed that the input for worn area modeling are a reconstructed worn mesh model and its nominal mesh model. The remainder of the paper is organized as follows: Section 3 discusses the methodologies of the multi-feature fitting and shape adaption algorithm. A rigid-body best-fit lemma is proposed and discussed in Section 3.1. Processes and methods of building cross-sections and features are explained in Section 3.2

for the input of best-fit algorithm. Section 3.3 explains the least square method and density-based outlier detection method for multi-feature fitting algorithm. Section 3.4 describes the shape adaption algorithm which includes the cross-section comparison for fracture surface construction and dilation for defect reconstruction. Section 4 presents illustrative examples with typical components and different kinds of defects that are used to demonstrate the flexibility and capability of using multi-feature fitting and shape adaption algorithm developed in this paper. Section 4.1 presents various feature-fitting strategies and defect reconstruction for several broken parts models such as the bearing house model, turbine rotor model, and the bracket. Adaptive slicing and various shape adaption process are demonstrated in Section 4.2 for deformed components. Finally, the conclusions, applications, and future work are discussed in Section 5.

3. METHODOLOGY

This section discusses the methodologies of the multi-feature fitting and shape adaption algorithm. It is assumed that the input for worn area modeling in this paper are a reconstructed worn mesh model and its nominal mesh model. Since most of the components have a planar reference surface for alignment or fixture, either for subtractive manufacturing or additive manufacturing. It is also assumed the models used in this paper have planar reference surface for feature extraction.

3.1.RIGID BODY BEST-FIT

As discussed in the introduction, best-fit algorithms determine the transformation rule for rigid body transformations consisting of the translation and rotation in 3D space. Lemma 1 gives a sufficient condition to best-fit two rigid bodies.

Lemma 1: If there are three non-collinear points in these two rigid bodies are best-fitted, it is sufficient to best-fit these two rigid bodies.

Proof: Figure 3.1 shows two identical rigid bodies at two different positions and orientations. Let P_0, P_1, P_2 be three non-collinear points on rigid body (a) with their corresponding points P'_0, P'_1, P'_2 on rigid body (b). First, let rigid body (b) translate and make P_0, P'_0 fitted. After one point is fitted, model (b) has three rotation freedoms to rotate with respect to P'_0 . Then, let P_1, P'_1 be fitted. After two points are fitted, rigid body (b) only has the freedom to rotate with respect to axis $P'_1 - P'_0$. Finally, let P_2, P'_2 be fitted, and note that

P_2' is non-collinear with P_1', P_0' . After three points are fitted, rigid body (b) has no freedom to translate and rotate which means these two rigid bodies are best-fitted.

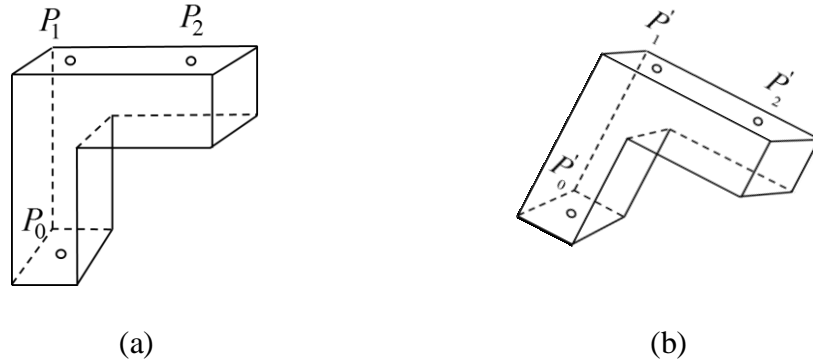


Figure 3.1 Rigid body best-fit

3.2.CROSS-SECTIONS AND FEATURES CONSTRUCTION

Lemma 1 gives the mathematical foundation for the multi-feature fitting algorithm and provides guidance for how to build features for the best-fit algorithm in order to get the best-fit result. This subsection describes the procedures and methods to build cross-sections and features. The following steps explain how to construct cross-sections and features:

Step 1: Select initial slice point p_0 and initial slice direction n_0 . Most of the components have a planar reference surface for alignment or fixture, either for subtractive manufacturing or additive manufacturing. Therefore, the vertices and normal direction on the reference surface can be defined as the initial slice point and initial slice direction. For using the mesh model in this paper, any triangle on the reference surface can be selected to provide initial slice point and slice direction for the slicing process. Figure 3.2 shows the

cross-sections and features construction process for a 3D nominal and worn cone model. As Figure 3.2 (a) and (c) show, a triangle on the bottom surface of a cone shape is selected, a vertex of the selected triangle is defined as the initial slice point, and the opposite direction of the normal direction is defined as the initial slice direction.

Step 2: Construct cross-sections. Slice along the initial slice direction for the whole 3D model. After slicing the first layer, the next slice point will move to $p = p_0 + t * n_0$, where t is the slice layer thickness. The slicing process will achieve a series of cross-sections of the 3D model. For each cross-section, it consists of one or multiple contours. Each contour is a polygon that consists of lines. The cross-sections of the cone shape are shown in Figure 3.2 (b) and Figure 3.2 (d) for the nominal model and the worn component model respectively.

Step 3: Build features. Because the cross-sections of the worn component model could be in an arbitrary position and orientation with respect to the nominal component model, the cross-sections are not useful for the best-fit algorithm directly. From Lemma 1, if the corresponding points of the 3D models could be found for the best-fit algorithm, the models could be best-fitted. In this paper, the features are constructed for corresponding points from cross-sections. They can be, but are not limited to, the centroid of the cross-section CCS , centroid of the convex-hull of the cross-section cch , and the centroid of minimal area bounding-box of the convex-hull cbb . The cross-sections obtained from 3D mesh models consist of contours that are closed polygon; therefore, computing the centroid of the cross-section, convex-hull, and the bounding-box equals to identifying the centroid of a 2D closed polygon. The method of computing the centroid of a 2D polygon was presented in [24]. As described in Figure 3.3, a polygon consisting of line segments

between N vertices will adhere to the following: $P_i = (x_i, y_i), i = 0, \dots, N-1$. If it is a close polygon, $P_0 = P_N$. The centroid of a polygon, which is also known as the “center of gravity” or the “center of mass”, can be calculated using Equation (1):

$$\begin{cases} c_x = \frac{1}{6A} \sum_0^{N-1} (x_i + x_{i+1})(x_i y_{i+1} - x_{i+1} y_i) \\ c_y = \frac{1}{6A} \sum_0^{N-1} (y_i + y_{i+1})(x_i y_{i+1} - x_{i+1} y_i) \end{cases} \quad (1)$$

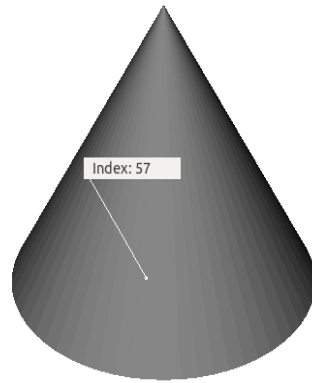
where, $A = \frac{1}{2} \sum_0^{N-1} (x_i y_{i+1} - x_{i+1} y_i)$.

The red dots shown in Figure 3.2 (b) and Figure 3.2 (d) are the features of the nominal component model and worn component model. The convex-hull of a cross-section equals to computing the convex-hull of the 2D points set from the cross-section. The quickhull algorithm for convex hull of a set of points was explained in [25]. The 2D convex-hull is used to find the minimal area bounding box. The method of determining the minimal area bounding-box of 2D closed curve was presented in [26].

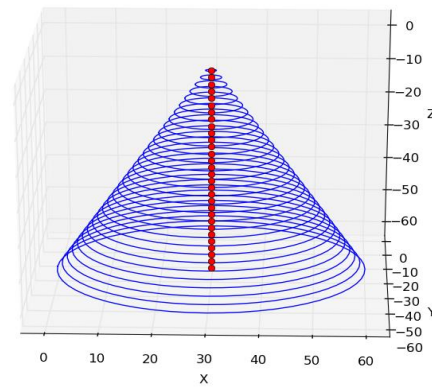
3.3.MULTI-FEATURE FITTING ALGORITHM

This section explains the principle and processes of the multi-feature fitting algorithm. The objective of this algorithm is to best-fit the 3D worn component model with 3D nominal component model through best-fitting the features from their cross-sections. The transformation matrix obtained from feature-fitting is used to best-fit the 3D model. The procedures of the multi-feature fitting algorithm are described in Figure 3.4. Generally speaking, there are two level's feature fitting to obtain the best-fit result: the model level's feature fitting and the cross-section level's feature fitting. The slices and feature

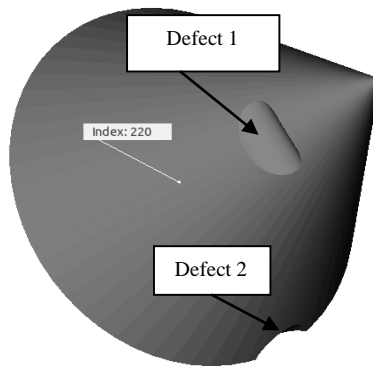
construction process was described in the previous section. At the beginning, the least square method is adopted to best-fit the model level's feature fitting. Because the defect geometry affects the features, the least square method cannot get the best-fit result through one-step calculation. For the least square method to get reasonable best-fit results, the features from the undamaged area of the worn component should be much more than from the damaged area. The acceptable feature-fitting result guarantees the undamaged feature fitted better than the damaged feature. Therefore, the outlier detection method is applied to



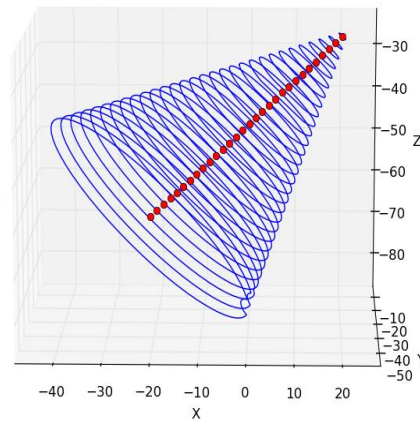
(a) A 3D mesh model of nominal component and face selection



(b) Cross-sections and features of nominal



(c) A 3D mesh model of worn component and face selection



(d) Cross-sections and features of worn model

Figure 3.2 Cross-sections and features construction

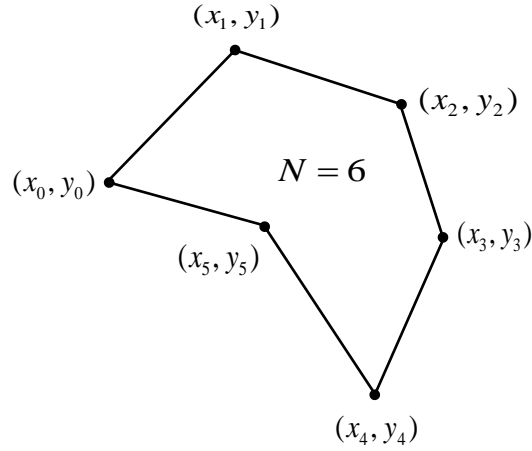


Figure 3.3 An example of a 2D polygon

take out the poorly fitted features. The least square method and the outlier detection method are alternative approaches to find the best-fit result gradually. However, in some cases, the model level's feature fitting is not sufficient to best-fit the model. According to Lemma 1, if the feature from the 3D model is one-dimensional, such as the 3D model's central symmetric or axial symmetric model, the model level's feature fitting may not be sufficient to best-fit the 3D model. For one dimensional features, the cross-section level's feature fitting can be used for further fitting to best fit the 3D model. If the feature for the model level's feature fitting is two-dimensional or three-dimensional, it is sufficient to best-fit the 3D model according to Lemma 1. Finally, if the fitted result is acceptable under tolerance, the best-fit transformation matrix will be obtained. Meanwhile, the outlier detection method filters the features from the defect geometry area, and those points provide the information for defect detection and reconstruction. The following subsection will discuss the least square method and outlier detection method in detail for feature-fitting.

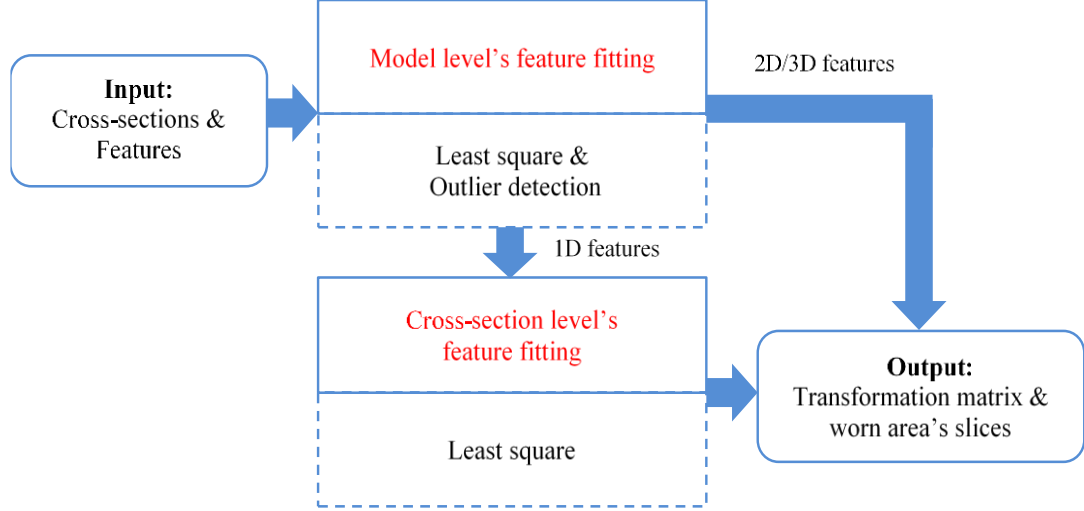


Figure 3.4 Multi-feature fitting algorithm

3.3.1. Least Square Method. Consider a nominal component model's feature consisting of N vertices $P_i^o = (x_i^o, y_i^o, z_i^o)$, $i = 0, \dots, N-1$ and a worn component model's feature consisting of M vertices $P_i^w = (x_i^w, y_i^w, z_i^w)$, $i = 0, \dots, M-1$. Here, $N \geq M$. If $N > M$, the first M feature points from nominal model are used for the calculation, because arbitrary translation can be represented by three translation variables (x, y, z) and arbitrary rotation can be represented by three rotation variables such as the roll-pitch-yaw (ϕ, θ, ψ) [27]. The transformation rules can be defined by Equation (2):

$$T = T_{trans} * T_{z,\phi} * T_{y,\theta} * T_{x,\psi} \quad (2)$$

The least square method determines (x, y, z) and (ϕ, θ, ψ) to build transformation matrix so that the worn model's feature best fits the nominal model's feature.

The transformed worn model's feature $P_i^{w'}$ can be obtained by Equation (3):

$$P_i^{w'} = T * \begin{bmatrix} x_i^w \\ y_i^w \\ z_i^w \\ 1 \end{bmatrix} \quad (3)$$

As Equation (4) shows, the objective of best-fit is to minimize the sum of square difference between nominal model's feature and the transformed worn model's feature.

$$\text{Objective: } \min \sum_{i=0}^{M-1} (P_i^o - P_i^{w'})^2 \quad (4)$$

Where,

$$\text{the translate matrix is } T_{trans} = \begin{bmatrix} 1 & 0 & 0 & x \\ 0 & 1 & 0 & y \\ 0 & 0 & 1 & z \\ 0 & 0 & 0 & 1 \end{bmatrix}; \text{ the rotation matrix with respect to z-axis is}$$

$$T_{z,\phi} = \begin{bmatrix} c_\phi & -s_\phi & 0 & 0 \\ s_\phi & c_\phi & 0 & 0 \\ 0 & 0 & 1 & 0 \\ 0 & 0 & 0 & 1 \end{bmatrix}; \text{ the rotation matrix with respect to y-axis is } T_{y,\theta} = \begin{bmatrix} c_\theta & 0 & s_\theta & 0 \\ 0 & 1 & 0 & 0 \\ -s_\theta & 0 & c_\theta & 0 \\ 0 & 0 & 0 & 1 \end{bmatrix}; \text{ the}$$

$$\text{rotation matrix with respect to x-axis is } T_{x,\psi} = \begin{bmatrix} 1 & 0 & 0 & 0 \\ 0 & c_\psi & -s_\psi & 0 \\ 0 & s_\psi & c_\psi & 0 \\ 0 & 0 & 0 & 1 \end{bmatrix}; \text{ and the transformation matrix}$$

$$\text{is } T = \begin{bmatrix} c_\phi c_\theta & -s_\phi c_\psi + c_\phi s_\theta s_\psi & s_\phi s_\psi + c_\phi s_\theta c_\psi & x \\ s_\phi c_\theta & c_\phi c_\psi + s_\phi s_\theta s_\psi & -c_\phi s_\psi + s_\phi s_\theta c_\psi & y \\ -s_\theta & c_\theta s_\psi & c_\theta c_\psi & z \\ 0 & 0 & 0 & 1 \end{bmatrix}.$$

According to Lemma 1, if the model level's features is one dimensional, the model level's feature-fitting may not be sufficient to best-fit the model, such as in the outside

symmetric geometry with inner holes. The unit vector of the direction along the model level's features is defined as $V_m = (u, v, w)$. The cross-section level's feature-fitting is to best-fit the features from the cross-section based on rotating the features with respect to the vector V_m at a certain angle φ . In this paper, a nominal cross-section and its corresponding worn cross-section after the model level's feature-fitting is selected for the cross-section level's feature fitting. Consider the features from nominal cross-section is a set of points $PC_i^o = (x_i^o, y_i^o, z_i^o)$, $i = 0, \dots, N-1$, the features from a worn cross-section is a set of points $PC_i^w = (x_i^w, y_i^w, z_i^w)$, $i = 0, \dots, M-1$. The cross-section can be from defect areas or an undamaged area's geometry. The transformed worn model's feature $PC_i^{w'}$ can be obtained by Equation (5):

$$PC_i^{w'} = T_{V_m} * \begin{bmatrix} xC_i^w \\ yC_i^w \\ zC_i^w \\ 1 \end{bmatrix} \quad (5)$$

As Equation (6) shows, the least square method for cross-section level's feature-fitting is define as to minimize the sum of square distance of transformed worn cross-section feature point $PC_i^{w'}$ to nominal cross-section feature points set PC^o . The distance between PC_i^o to PC^o is define as the minimal distance between each PC_i^o to PC_i^w .

$$\text{Objective: } \min \sum_{i=0}^{M-1} (PC_i^{w'} - PC^o)^2 \quad (6)$$

Where,

$$T_{V_m} = \begin{bmatrix} c_\varphi + u^2(1 - c_\varphi) & uv(1 - c_\varphi) - ws_\varphi & uw(1 - c_\varphi) + vs_\varphi & 0 \\ uv(1 - c_\varphi) + ws_\varphi & c_\varphi + v^2(1 - c_\varphi) & vw(1 - c_\varphi) + us_\varphi & 0 \\ uw(1 - c_\varphi) - vs_\varphi & vw(1 - c_\varphi) + us_\varphi & c_\varphi + w^2(1 - c_\varphi) & 0 \\ 0 & 0 & 0 & 1 \end{bmatrix}.$$

The matrix for a rotation by an angle of φ about an axis in the direction of V_m is [28].

3.3.2. Density-based Outlier Detection. Features from the damaged area disturbs the results of best-fitting the worn model's feature to the nominal model's feature when applying the least square method, and since there are more features from the undamaged area than damaged area, the features of the undamaged area fit better than the damaged area. Therefore, density-based outlier detection method [29] is adopted in this paper to take out the relative poorly fitted features to minimize the disturbances from features of the damaged area. The first calculation using the least square method be used to find the distance between each corresponding features $D_i = P_i^o - P_i^w$, $i = 0, \dots, M - 1$. Therefore, the density-based outlier detection method is for the set of features' distance $\{D_i\}_{i=0}^{M-1}$. The following steps explain the method used in this paper for outlier detection. The principle is to calculate each point's relative density and the greater than outlier threshold seen as outliers:

Step 1: Calculate the reach-distance between each feature point D_i to other points in the dataset $\{D_i\}_{i=0}^{M-1}$.

Step 2: Calculate the global reachability density of each feature point using below Equation (7):

$$Grd(D_i) = 1 / \left(\frac{\sum_{o \in \{D_i\}_{i=0}^{M-1}} reach_dist(D_i, o)}{M - 1} \right) \quad (7)$$

Step 3: Calculate global outlier factor (GOF) scores using Equation (8):

$$Gof(D_i) = \left(\frac{\sum_{o \in \{D_i\}_{i=0}^{M-1}} \frac{Grd(o)}{Grd(D_i)}}{M-1} \right) \quad (8)$$

Step 4: If GOF score is greater than outlier threshold, it is outliers.

3.3.3. An Example of Feature-fitting Processes. This subsection uses an example to demonstrate the processes of the feature-fitting algorithm. The features of the cone shape are constructed as explained in Section 1. The initial spatial relationship of nominal and worn model's features are shown in Figure 3.5. The red dots represent the features of nominal model and the blue stars represent the features of the worn model. Only the centroid of the cross-section is used as the feature because it is the central symmetric geometry.

At first, the least square method is used to fit the features. The first feature-fitting results in Figure 3.6 (a-1) show that the features of the undamaged area fit better than the features of defect area 1 and defect area 2. After the first feature-fitting, the density-based outlier detection method is used to detect the poorly fitted features. Figure 3.6 (a-2) shows the distance between two corresponding nominal feature to worn feature ranges by about 0.5 mm. The whole feature is not well fitted because of the disturbance from the defect geometry. Three outliers are detected for the first outlier detection and marked as red stars as shown in Figure 3.6 (a-2). According to the outlier detection results, three corresponding feature points are deleted as shown in Figure 3.6 (a-3), and those three points are the features of defect area 1. After taking out the outliers, the distance range between two corresponding features of the nominal and worn models is about 0.2 mm. The new features will be used for the second feature-fitting iteration. The second feature-fitting

results in Figure 3.6 (b-1) show that the density-based outlier detection method is used to detect the outliers. Two outliers are detected for the second outlier detection and marked as red stars as shown in Figure 3.6 (b-2). According to the outlier detection result, three corresponding feature points are deleted as shown in Figure 3.6 (b-3), which are from the features of defect area 2. After taking out the outliers, the maximal distance between two corresponding features of nominal and worn models is about 0.04 mm. The feature-fitting becomes better than the first iteration. The new features will be used for the third feature-fitting iteration. The third feature-fitting results as shown in Figure 3.6 (c-1), again density-based outlier detection method is used to detect the outliers. Only one outlier is detected for the second outlier detection and marked as red stars as shown in Figure 3.6 (c-2). According to the outlier detection result, three feature corresponding points are deleted as shown in Figure 3.6 (c-3) and those three points are the features of defect area 2. After taking out the outliers, the maximal distance between two corresponding features of nominal and worn models is about 0.004 mm. The feature-fitting becomes 10 times better than the second iteration. For this example, the threshold of acceptable maximal distance between corresponding features is defined as 0.01 mm. Therefore, the feature-fitting result after three iterations can be used to fit the cross-sections, and the outliers can be used to figure out which cross-sections are from the defect area. The results of using the feature-fitting algorithm for the cone shape are shown in Figure 3.7. The fitted features are shown in Figure 3.7 (a), fitted cross-sections are shown in Figure 3.7 (b), and worn-area cross-sections are shown in Figure 3.7 (c). As can be seen from this example, the feature-fitting algorithm in this paper can guarantee the efficiency and the accuracy through coupling the

least square method and the density-based outlier detection method, especially if the component dimension is large or uss high-resolution features.

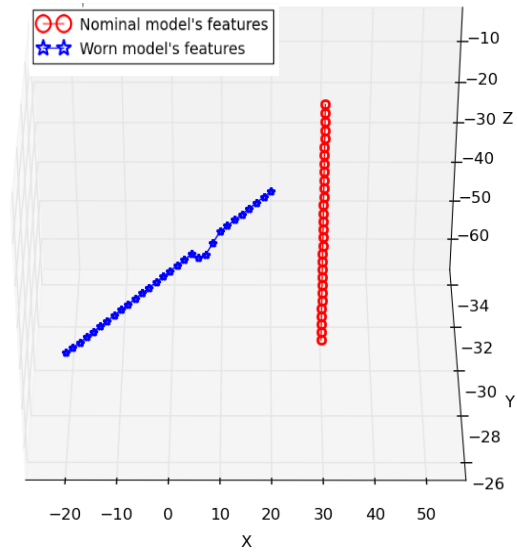
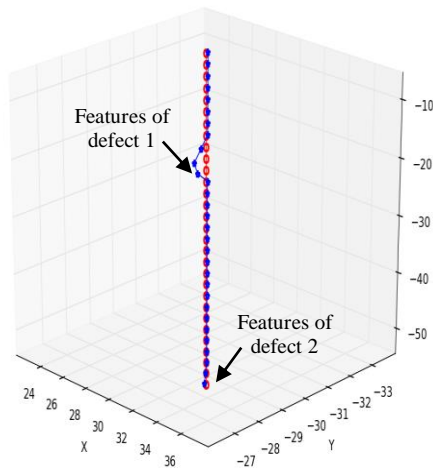
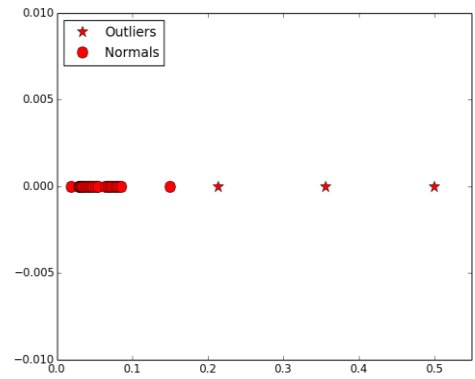


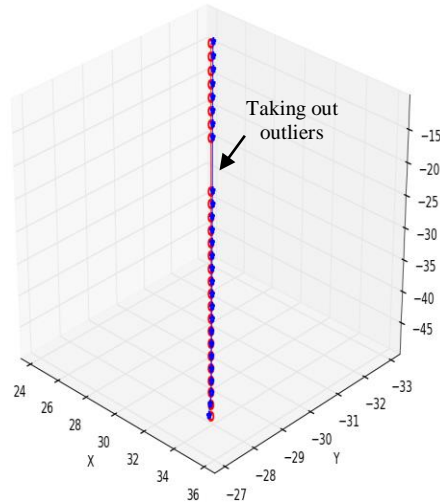
Figure 3.5 The initial spatial relationship of nominal and worn model's features



(1) The first feature-fitting by least-square method

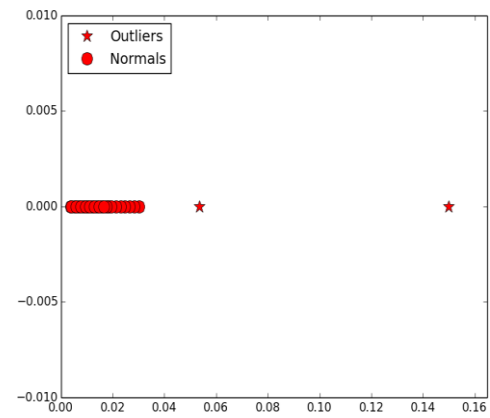
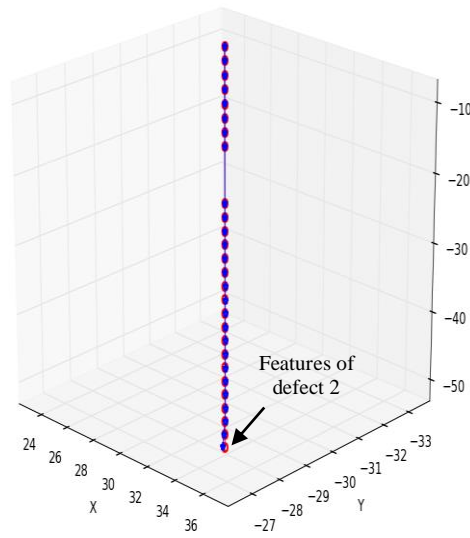


(2) The first outlier-detection after feature-fitting



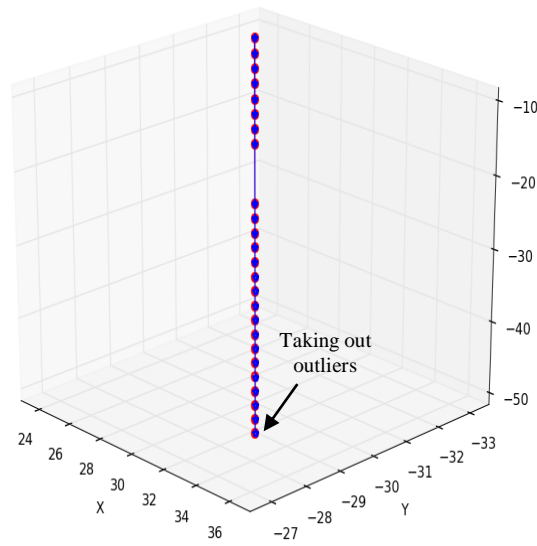
(3) Features after taking out outliers

Figure 3.6 An example of feature-fitting algorithm based on least-square and density-based outlier-detection. (a) The first iteration result of feature-fitting and outlier detection.



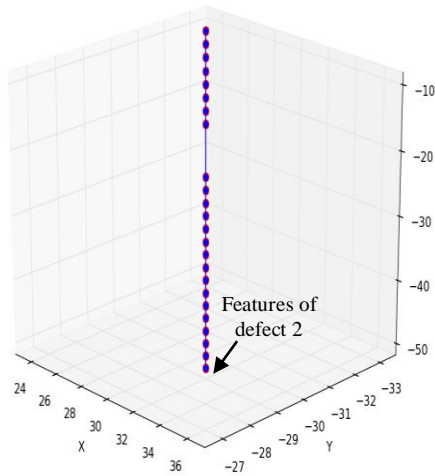
(1) The second feature-fitting by least-square method

(2) The second outlier-detection after feature-fitting

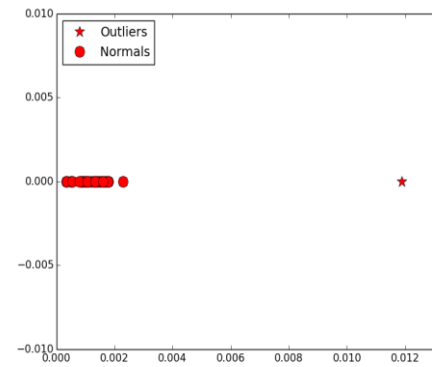


(3) Features after taking out outliers

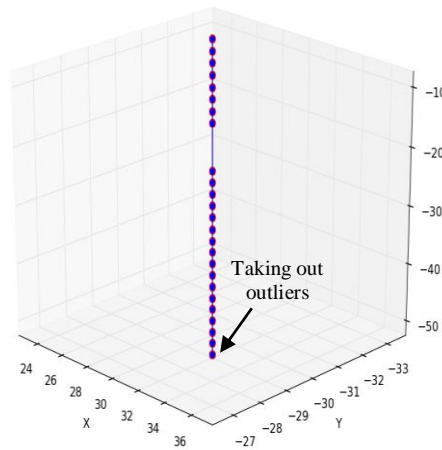
Figure 3.6 An example of feature-fitting algorithm based on least-square and density-based outlier-detection. (b) The second iteration result of feature-fitting and outlier detection. (cont.)



(1) The third feature-fitting by least-square

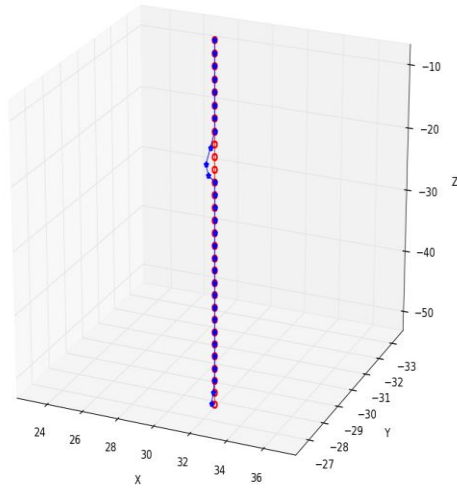


(2) The third outlier-detection after feature-

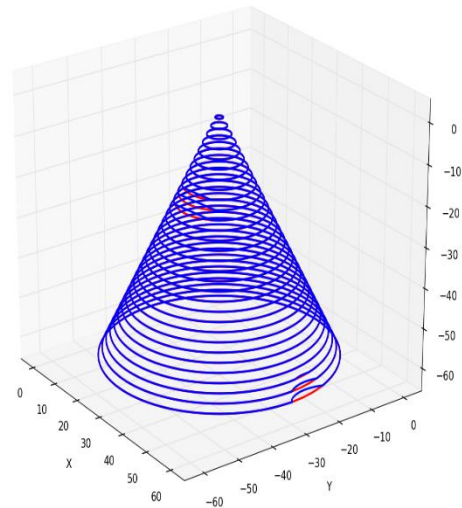


(3) Features after taking out outliers

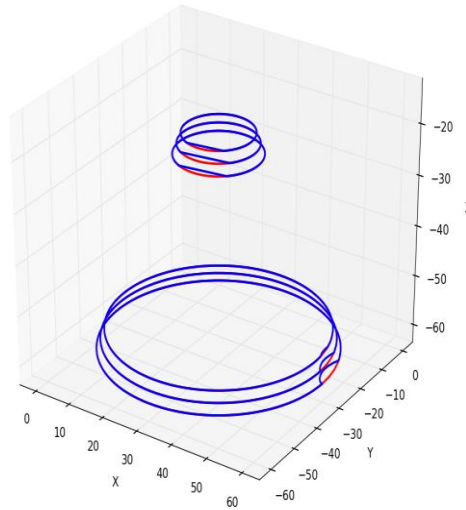
Figure 3.6 An example of feature-fitting algorithm based on least-square and density-based outlier-detection. (c) The third iteration result of feature-fitting and outlier detection. (cont.)



(a) Best-fitted features



(b) Fitted cross-sections after feature-fitting algorithm



(c) Fitted worn-area cross-sections

Figure 3.7 The results of using feature-fitting algorithm

3.4.SHAPE ADAPTION ALGORITHM

This section explains the shape adaption algorithm to reconstruct the defect geometry. In this paper, the shape adaption algorithm includes two stages shown in Figure 3.8, which are cross-section comparison and defect reconstruction. The best-fit models and detected worn area slices are input for the shape adaption algorithm. At the first stage, the

best-fitted worn area slices from the nominal component model and the worn component model are compared to identify the defect segments of the worn model's cross-sections. The goal of this stage is to construct the fracture surface of the defect area according to the defect segments. A 'point-line-surface' cross-section comparison algorithm is proposed and realized in this paper to construct fracture surface. The second stage is to trim the nominal model using fracture surface for defect reconstruction. Because the fracture surface obtained from stage 1 doesn't not have intersection with the nominal model, the fracture surface needs to be dilated firstly. The dilation parameters can be defined by the user. Mesh trim is adopted to obtain accurate defect geometry using dilated fracture surface.

3.4.1. Cross-section Comparison. A 'point-line-surface' cross-section comparison algorithm is proposed and implemented in this paper. The main idea is to use scan lines to detect the fracture segments of the worn area slices, then use the fracture segments to inversely derive fracture surface of the worn component model. The steps of cross-section comparison algorithm are described below:

Step 1: Import models, best-fitted slices, and define parameters. Import nominal model M_n , best-fitted worn model M_w for slicing. Define layer thickness and direction for slicing, threshold value for detection and etc.

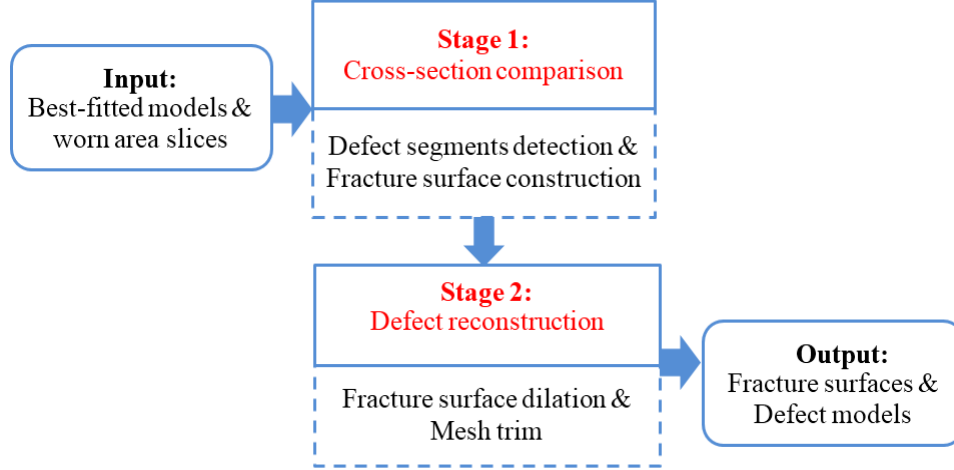


Figure 3.8 Stages of shape adaption algorithm

Step 2: Detect the first fracture segment with scan lines. For each cross-section pairs S_n, S_w which from M_n and M_w . S_n is consisted of u lines set $l_{1,n}, l_{2,n}, \dots, l_{u-1,n}, l_{u,n}$, S_w is consisted of v lines set $l_{1,w}, l_{2,w}, \dots, l_{v-1,w}, l_{v,w}$. A series of scan planes SP are adopted to get intersection with S_n, S_w . For each scan plane, intersection points set IPS_n, IPS_w with S_n, S_w are calculated. For each intersection point IP_w in IPS_w , calculate the distance from IP_w to each point in IPS_n , $DIS = \|IP_w - IPS_n\|$. If minimal distance of the $DIS > T_d$ (the threshold value for the first fracture segment detection), the first intersection point we define it as $IP_{f,w}$, which is from the first fracture segment which we can define it as $l_{f,w}$ in S_w as shown in Figure 3.9 (a).

Step 3: Extend the first fracture segment to construct the whole fracture segments. As Figure 3.9 (b) shows, after the first detected fracture point and segment, the algorithm

will do detection forward and backward along the cross-section to construct the whole fracture segments. The detection process is similar with Step 2.

Step 4: Construct fracture surface. All the fracture segments detected in Step 3 are used to construct fracture surface. As Figure 3.9 (c) shows, the fracture segments are from the intersection between slice plane with the worn component model (STL model in this paper). In the cross-section comparison algorithm, the fracture segment is indexed to which triangle it is from. In this way, fracture triangles are constructed according to the fracture segments.

Step 5: Slice the models in two additional directions and repeat Step 2, 3, 4. In some cases, the cross-sections from one slice direction is not enough to detect all the fracture triangles to construct the fracture surface, two addition orthogonal slice directions may be used repeat Step 2, 3 and 4 again to construct fracture surface. Finally, all detected fracture triangles which constitutes the fracture surface are exported to an STL file for the ensuing defect reconstruction.

Figure 3.10 shows an example of fracture surface construction. Figure 3.10 (a) shows the first fracture segment detection processes of the worn-area cross-sections of defect 1, a series scan planes are adopted to do detection from y negative to positive direction. The black dash lines represent the intersection between the scan planes and the cross-sections, the red dash line is the intersection between the scan plane and the first detected fracture segment. The constructed fracture segments are shown in Figure 3.10 (b) and Figure 3.10 (c) shows corresponded fracture surface of defect 1, and Figure 3.10 (d) is the fracture surface of defect 2.

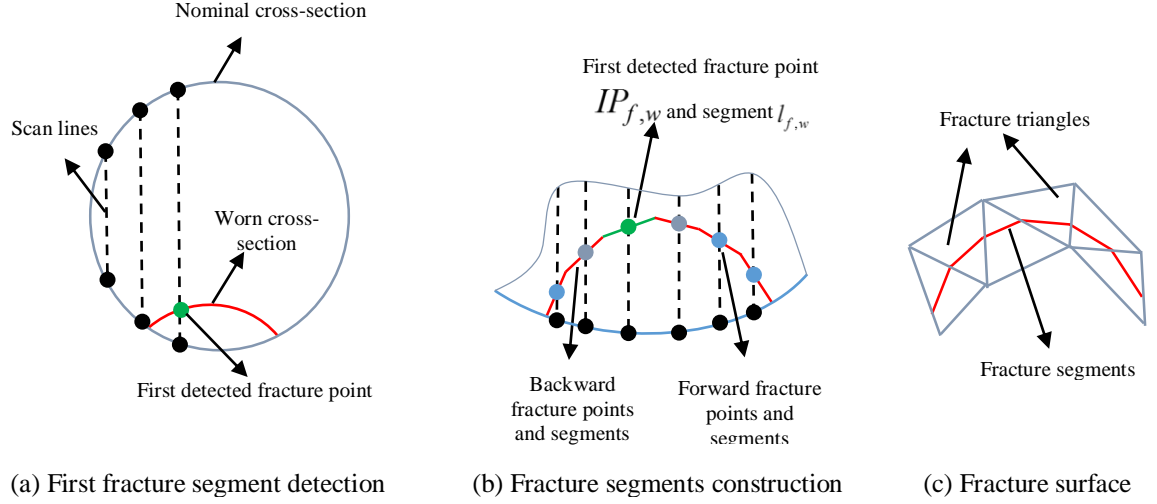
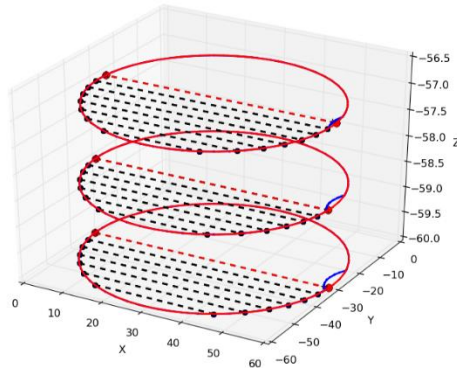


Figure 3.9 ‘Point-line-surface’ cross-section comparison processes

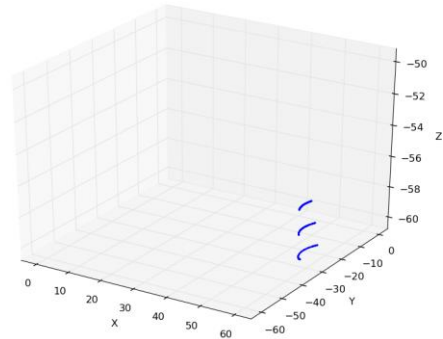
3.4.2. Defect Reconstruction. The basic idea for defect reconstruction in this paper is to use fracture surface to trim the nominal component model. However, the constructed fracture surface in the previous section cannot be directly used to trim nominal model because there is no intersection between them. Therefore, the vertices of the fracture surface boundary are dilated to get intersection. As Figure 3.11 (a) shows, P_{i-1}, P_i, P_{i+1} are three connective vertices on the fracture surface boundary, \vec{n}_{i-1}, \vec{n}_i are the normal direction of the triangles at the boundary. \vec{l} is the unit vector of $P_i - P_{i-1}$, \vec{m} is the unit vector of $P_{i+1} - P_i$, $\vec{u} = \vec{n}_{i-1} \times \vec{l}$, $\vec{v} = \vec{n}_i \times \vec{m}$. The dilated vertex P'_i of P_i can be obtained by following Equation (9). The dilated result shown as Figure 3.11 (b).

$$P'_i = P_i + t * \vec{d}_v \quad (9)$$

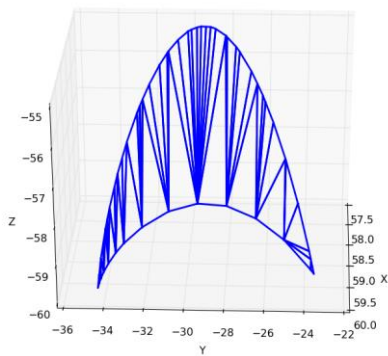
Where t is dilation length, $\vec{d}_v = \vec{u} + \vec{v}$.



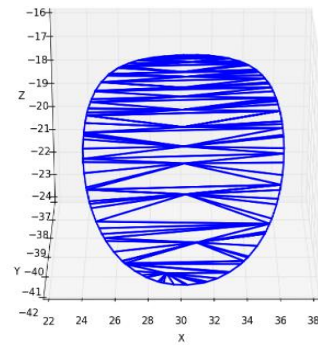
(a) Fracture point detection for worn cross-sections of defect 1



(b) Fracture segments construction of defect 1



(c) Fracture surface construction of defect 1



(d) Fracture surface construction of defect 2

Figure 3.10 An example of cross-section comparison and fracture surface construction

Using the vertices dilation algorithm, the dilated fracture surface of defect 1 and defect 2 are shown in Figure 3.12 (a) and (b). The dilated fracture surfaces are used to trim the nominal model which is shown in Figure 3.13 (a). In this paper, the STL format mesh model is used for mesh trim and the mesh trim operation is realized in Rhino as shown in Figure 3.13 (b). Finally, the defect geometry can be obtained as shown in Figure 3.14. Figure 3.14 (a) shows the assembled defects with worn model, Figure 3.14 (b) and (c) represent geometry of defect 1 and defect 2.

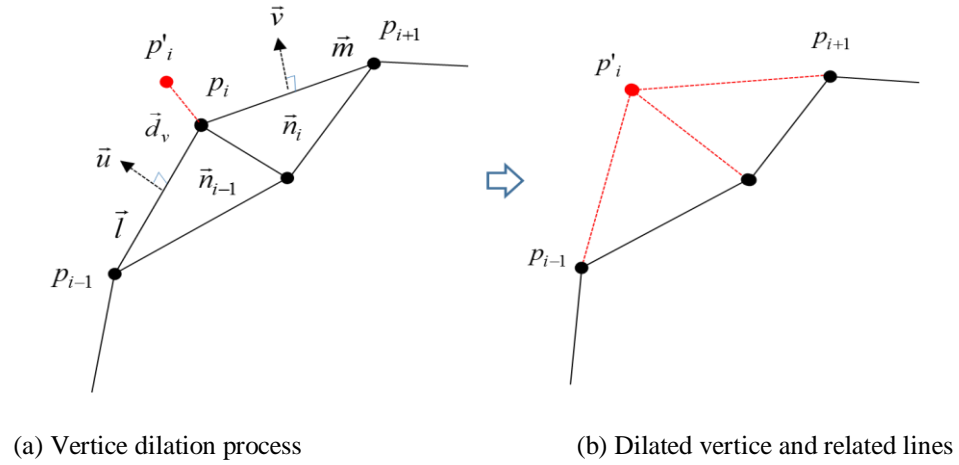


Figure 3.11 Vertices dilation for fracture surface boundary

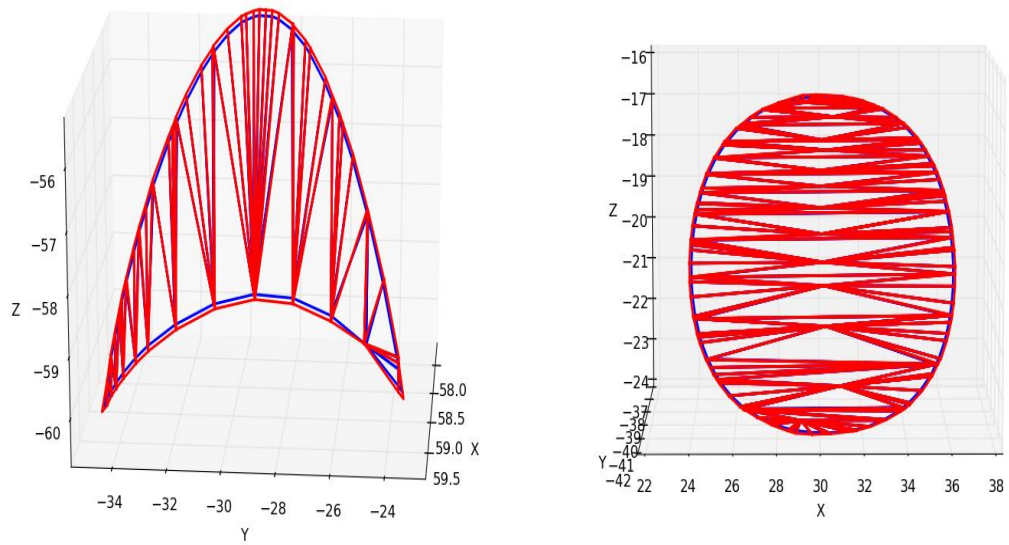
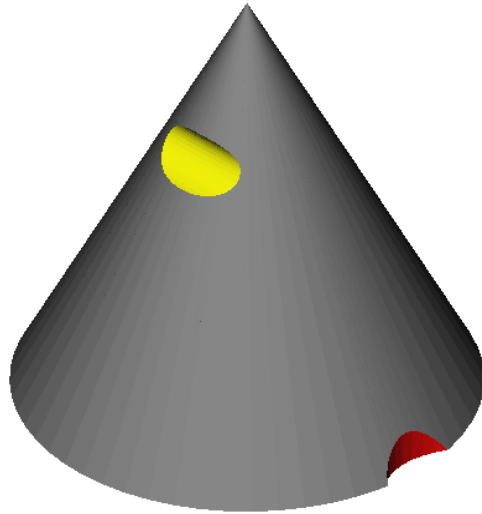
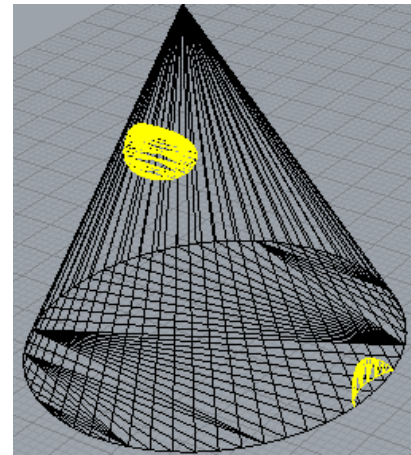


Figure 3.12 An example of fracture surface boundary dilation



(a) Fracture surface on the worn component model

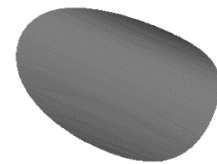


(b) Use dilated fracture surface to trim nominal

Figure 3.13 Mesh trim in Rhino for defect reconstruction



(a) Assemble defects with worn model



(b) Defect 1



(c) Defect 2

Figure 3.14 Mesh trim result for the example of a cone shape

4. ILLUSTRATIVE EXAMPLES

There are different kinds of defects and damages [30] which can be broken parts, worn out surface, corroded surface, and deformed parts. This section uses different illustrative examples to demonstrate the flexibility and robustness of the methods developed in this paper for different kinds of geometries and defects. Depends on the geometry of the component, the feature-fitting process and feature's selection may be different. For example, if the geometry is symmetric and the feature is one dimensional feature, cross-section level's feature-fitting maybe needed to best-fit the model after model level's feature-fitting. As for defect construction, the defect reconstruction strategy also can be different depends on the defect types. Such as for worn out surface or broken surface, the defect can be obtained using fracture surface to trim nominal model. But for deformed parts, it needs to build the intersection surface between the nominal model and the deformed model to get the deformed geometry and the missed geometry. This section will discuss how to use multi-feature fitting and defect reconstruction for different kinds components and defects. The software for cross-section and feature construction, feature-fitting, cross-section comparison and fracture surface construction and dilation are developed in Python, with Scipy, Matplotlib, and etc.

4.1.ILLUSTRATIVE EXAMPLES FOR BROKEN COMPONENTS

As presented in Section 3, the cone shape is central symmetric geometry and centroids of the cross-sections is one dimensional feature. Model level's feature fitting is used to best-fit features. Because each cross-section is circle, model level's feature fitting

is sufficient to best-fit the model. But for other case, such as for the bearing house model shown in Figure 4.1 (a), it needs combine model level's feature-fitting with cross-section level's feature-fitting to obtain the best-fit result. Figure 4.1 (a) and (b) shows the nominal model and worn component model, and the bottom surface is defined as the reference surface for cross-sections and features construction shown in Figure 4.1 (c). The geometry of bearing house is also symmetric and the feature is in one dimension, but each cross-section has inner holes. After model level's feature-fitting, the features are best-fitted as shown in Figure 4.2 (b). As can be seen from Figure 4.2 (c), the transformation matrix is used to transform the worn model's cross-sections. The outside cross-sections are not best-fitted, but the inner holes on the cross-sections are not best-fitted. According Lemma 1, there is one rotation freedom left after model level's feature fitting. Figure 4.3 (a) shows one un best-fitted cross-section from nominal model and worn model, then the centroids of the inner holes are calculated for the cross-section level's feature fitting. As Figure 4.3 (a) shows, the red dots represent the features from nominal model's cross-section, and blue stars represent the features from worn model's cross-section. Cross-section level's feature-fitting is adopted to best-fit the features and the result shows in Figure 4.3 (b). Combine model level's feature-fitting with cross-section level's feature-fitting, the inner holes on the cross-sections are fitted and the worn bearing house model is best-fitted with the nominal model as shown in Figure 4.3 (c). After that, cross-section comparison algorithm is adopted to construct the fracture surface. For this bearing house model, cross-section comparison algorithm for the initial slice direction as shown in Figure 4.4 (a) is not sufficient to construct the whole fracture surface. Therefore, another slice direction which is perpendicular to the first slice direction is adopted for the second cross-section

comparison. Generally, three orthogonal slice direction for shape adaption algorithm will cover the whole fracture surface depends on the geometry. Otherwise, it needs to decrease the layer thickness for slicing. The fracture surface construction result is shown in Figure 4.4 (c). Then the fracture surface boundary vertices are dilated as shown in Figure 4.5 and the dilated fracture surface is used for mesh trim. Finally, the defect geometry is reconstructed as shown in Figure 4.6. Other illustrative examples for broken parts are bracket and turbine rotor. As Table 4.1 shows, the feature of bracket is in three dimension and model level's feature fitting is used to best-fit the model. Two fracture surfaces are constructed and then to trim the nominal model to obtain the defect geometry. For the turbine rotor, the feature is in one dimensional without inner holes. For the cross-section level's feature-fitting, the corners of the minimal area bounding box of the cross-section are defined as features for the feature-fitting. The feature-fitting and defect reconstruct result is shown in Table 4.1.

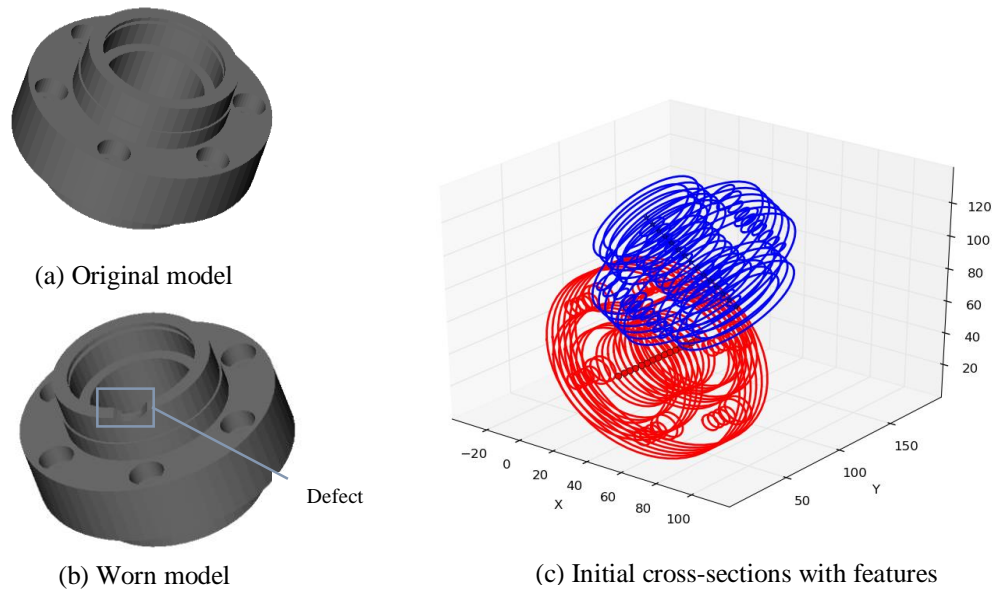


Figure 4.1 Bearing house model and cross-sections with features

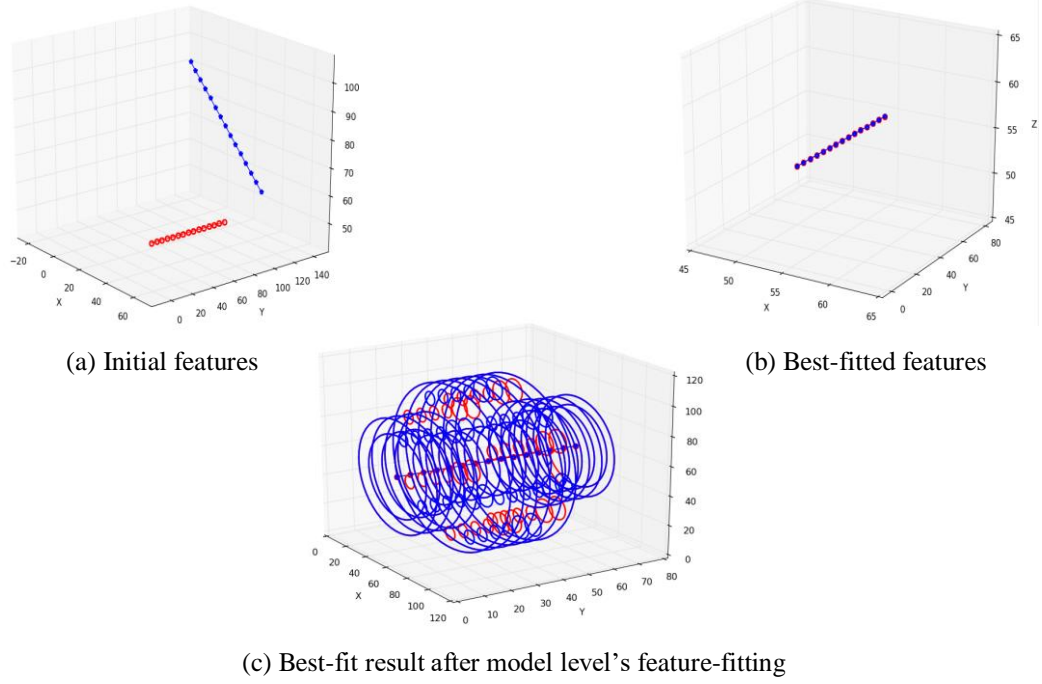


Figure 4.2 Model level's feature-fitting for 1D feature—Bearing house

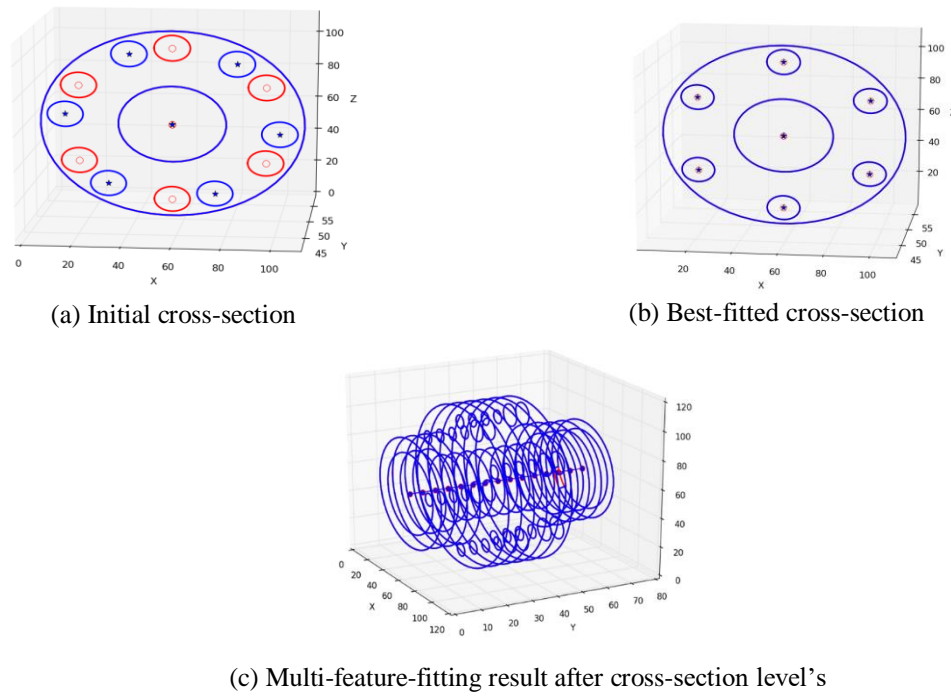
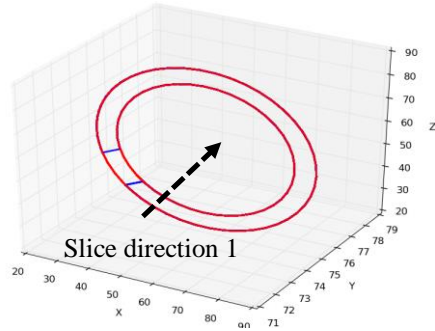
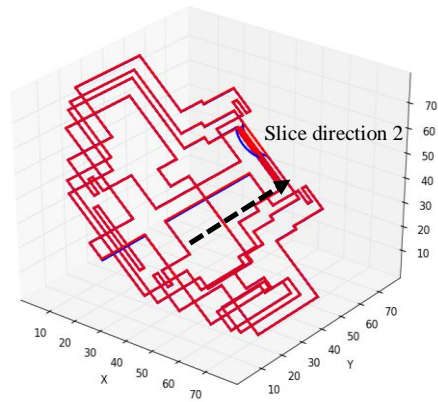


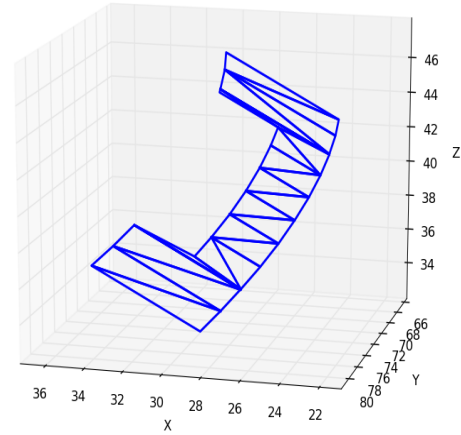
Figure 4.3 Cross-section level's feature-fitting—Bearing house



(a) Cross-section comparison along the first axis

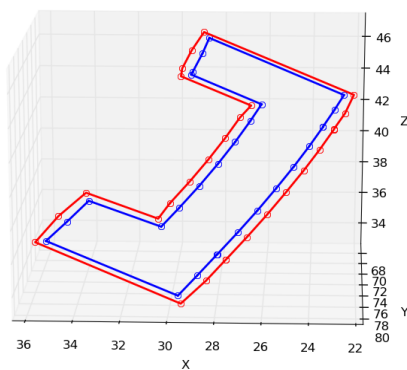


(b) Cross-section comparison along the second axis

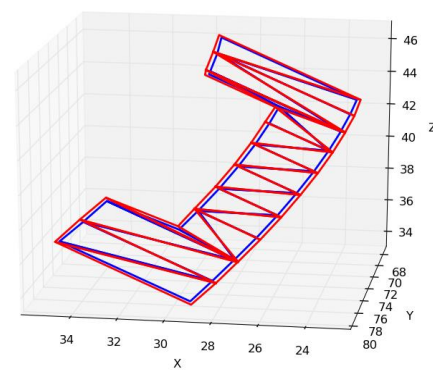


(c) Fracture surface

Figure 4.4 Shape adaption algorithm—Bearing house



(a) Dilated boundary vertices



(b) Dilated fracture surface

Figure 4.5 Fracture surface dilation—Bearing house

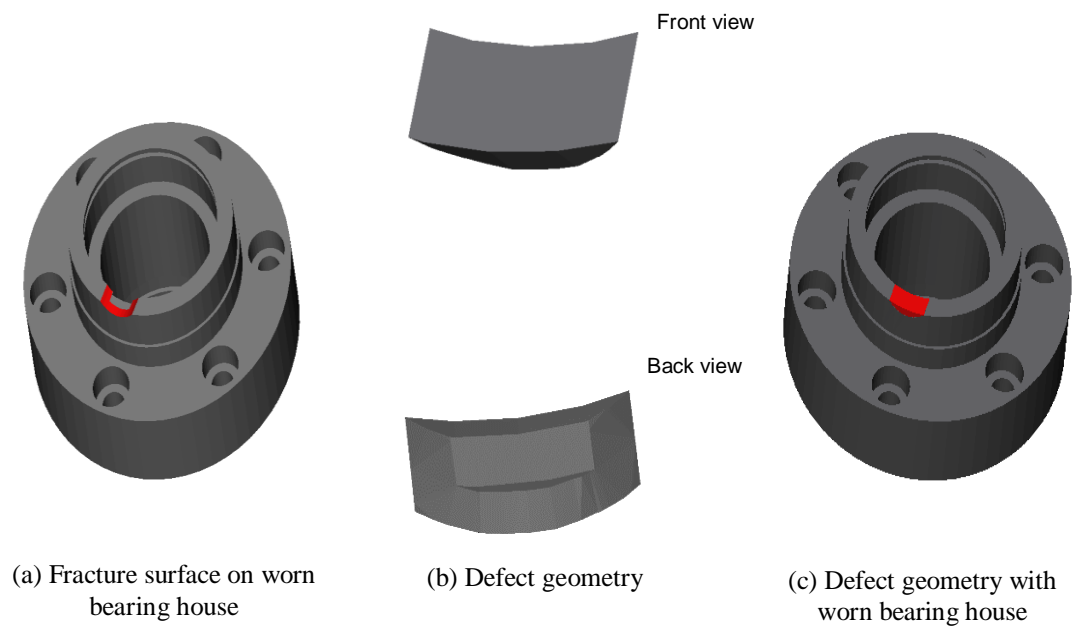


Figure 4.6 Mesh trim and defect reconstruction—Bearing house

Table 4.1 Multi-feature fitting and shape adaption algorithm for broken parts.
(a) Bracket.



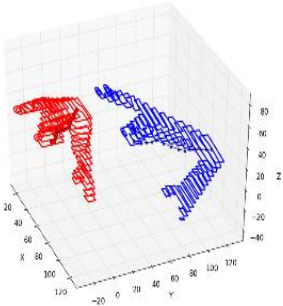
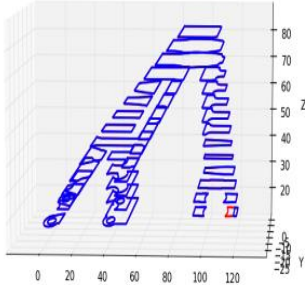
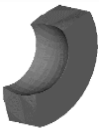
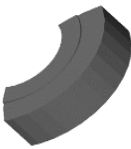

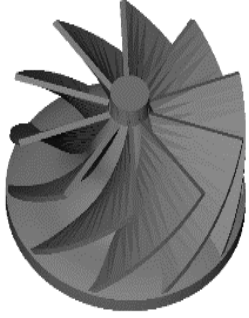
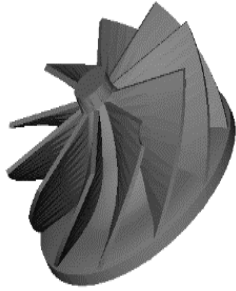
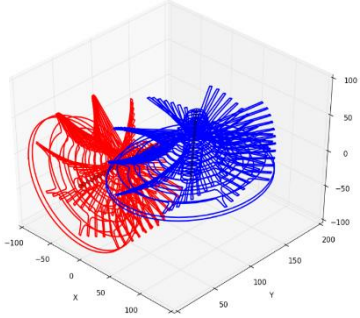
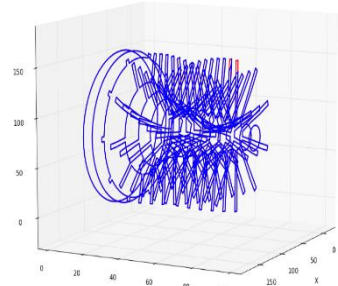


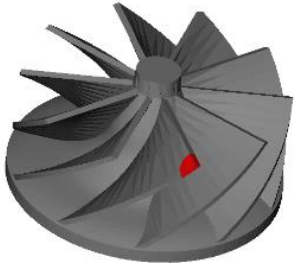
Part name	(a) Bracket	
Input	 <p data-bbox="581 743 834 772">Nominal bracket model</p>	 <p data-bbox="1057 751 1279 781">Worn bracket model</p>
Feature-fitting	 <p data-bbox="532 1226 889 1255">Initial cross-sections and features</p>	 <p data-bbox="1036 1226 1307 1255">Best-fitted cross-sections</p>
Defect reconstruction	<p data-bbox="699 1352 792 1373">Side view 1</p>  <p data-bbox="699 1570 792 1591">Side view 2</p>  <p data-bbox="618 1787 802 1816">Defect geometry</p>	 <p data-bbox="943 1787 1398 1816">Defect geometry with worn bracket model</p>

Table 4.1 Multi-feature fitting and shape adaption algorithm for broken parts.
(b) Turbine rotor. (cont.)

Part name	(b) Turbine rotor	
Input	 <p data-bbox="557 779 862 806">Nominal turbine rotor model</p>	 <p data-bbox="1032 772 1305 800">Worn turbine rotor model</p>
Feature-fitting	 <p data-bbox="532 1255 889 1283">Initial cross-sections and features</p>	 <p data-bbox="1036 1255 1307 1283">Best-fitted cross-sections</p>
Defect reconstruction	<p data-bbox="716 1325 797 1346">Side view 1</p>  <p data-bbox="721 1570 802 1591">Side view 2</p>  <p data-bbox="621 1728 802 1755">Defect geometry</p>	 <p data-bbox="954 1682 1386 1766">Defect geometry with worn turbine rotor model</p>

4.2. ILLUSTRATIVE EXAMPLES FOR DEFORMED COMPONENTS

This subsection will discuss the strategy of applying the methodology for the deformed components. Blades are the most critical components in an aero engine and a small change of the blade geometry can lead to a large change in engine performance [31, 32]. A lot of researches focus on developing the automated repair processes for aero-engine components in the papers [2, 5, 12, 13, 18-22, 33, 34], especially for blades. In this paper, a curved blade model is used to demonstrate the worn area modeling processes developed in this paper. As Figure 4.7 (a) and (b) shows, a nominal curved blade mesh model and a deformed mesh model are input for the feature-fitting and defect reconstruction. A triangle on the blade top surface is selected for the reference to define the slice direction and initial slice point. Adaptive slicing and multiple features are used for the cross-section and feature construction. Non-uniform slice layer thickness is defined for the deformed and non-deformed geometry. As can be seen from Figure 4.7 (c), a higher resolution cross-sections are obtained by defining smaller slice layer thickness for the non-deformed geometry. The red cross-sections and dots represent the cross-sections. The same adaptive slicing strategy can also be applied for the non-complete geometry repair. Since each cross-section of curved blade is not symmetric, the centroid of the cross-section and the centroid of the minimal area bounding box are constructed for features. The strategy of adaptive slicing and multiple features construction will provide more features from the non-deformed geometry than the deformed area to expedite the feature-fitting iterations. The initial spatial relationship of nominal and worn model features are shown in Figure 4.8 (a). The feature-fitting result is shown in Figure 4.8 (b) and (c). After the cross-sections are best-fitted, the whole shape adaption algorithm is adopted to construct fracture surface on nominal blade

and deformed blade surface as shown in Figure 4.9 and Figure 4.10. The fracture surface of the blade surface is composed of top surface and side surface. Instead of using fracture surface to trim nominal surface to get defect geometry for broken part, intersection surface is used to trim fracture surface to get defect geometry for deformed part. The intersection surface between side surface of fracture surface on nominal blade surface and the side surface of fracture surface on deformed blade surface is defined as the intersection surface. As shown in Figure 4.11 (a), dilated side surface on the deformed blade model is used to trim side surface on nominal model to get intersection surface on the nominal blade model as shown in Figure 4.11 (b) and (c). Similarly, intersection surface on the deformed blade model as shown in Figure 4.12 (b) and (c) can be obtained using dilated side surface on the nominal blade model is used to trim side surface on deformed blade model as shown in Figure 4.12 (a). Finally, intersection surface on nominal model is dilated to trim fracture surface on deformed model as shown in Figure 4.13 (a) to get deformed geometry as shown in Figure 4.13 (b) and (c). And intersection surface on deformed model is dilated to trim fracture surface on nominal model as shown in Figure 4.14 (a) to get the missing geometry as shown in Figure 4.14 (b) and (c). The final defect reconstruction result shows in Figure 4.15, the deformed geometry shown in Figure 4.15 (b) needs to be machined and missed geometry shown in Figure 4.15 (c) needs to be rebuilt.

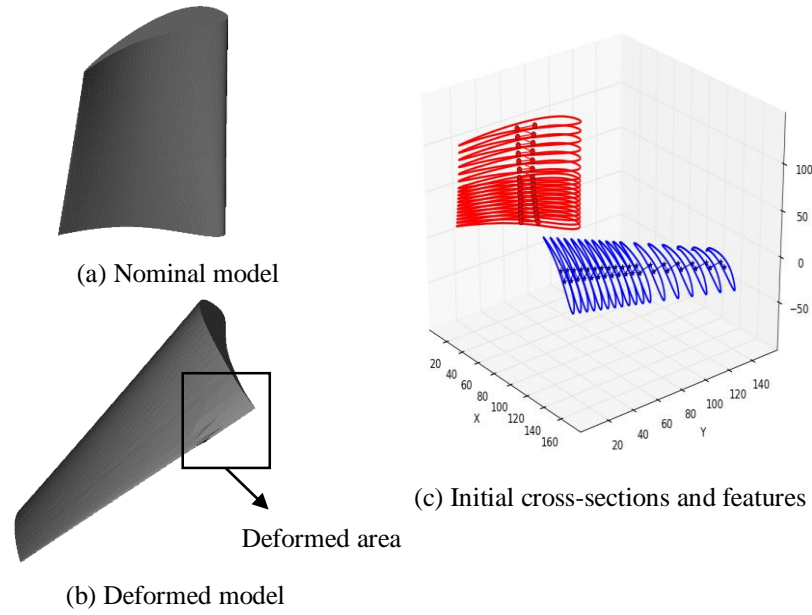


Figure 4.7 Curved bladed model, adaptive slicing and feature construction

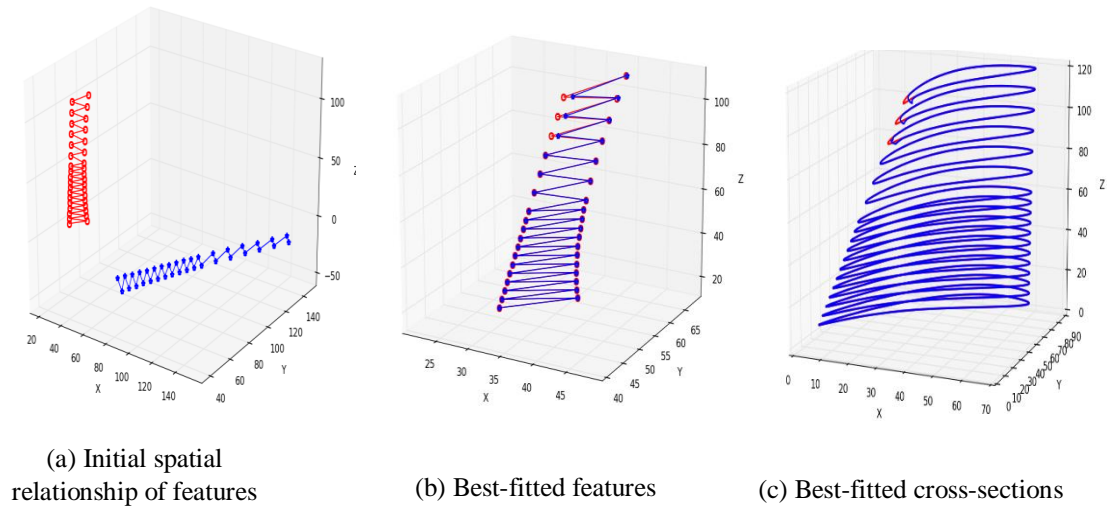


Figure 4.8 Multi-feature fitting results

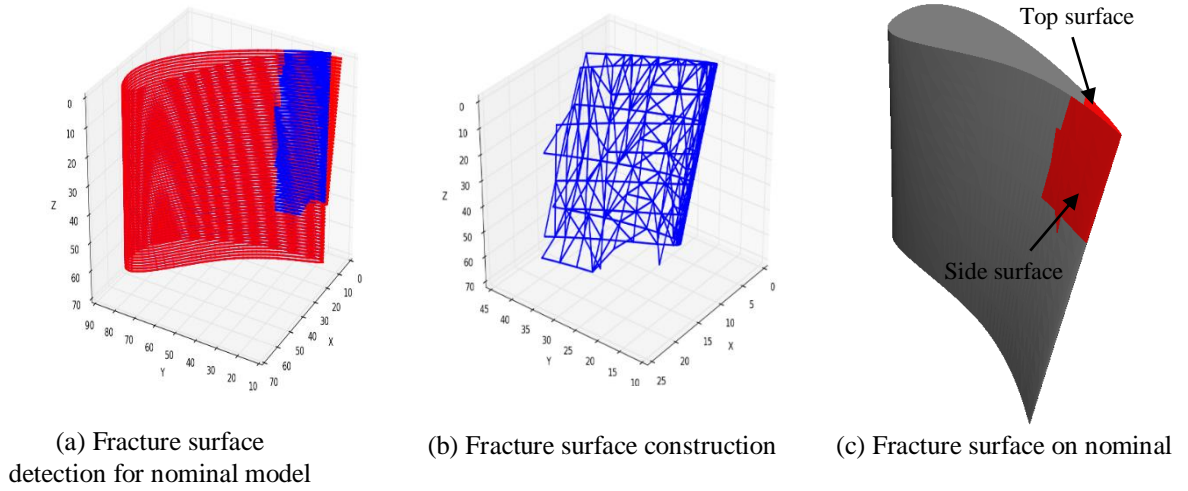


Figure 4.9 Fracture surface construction on nominal blade model

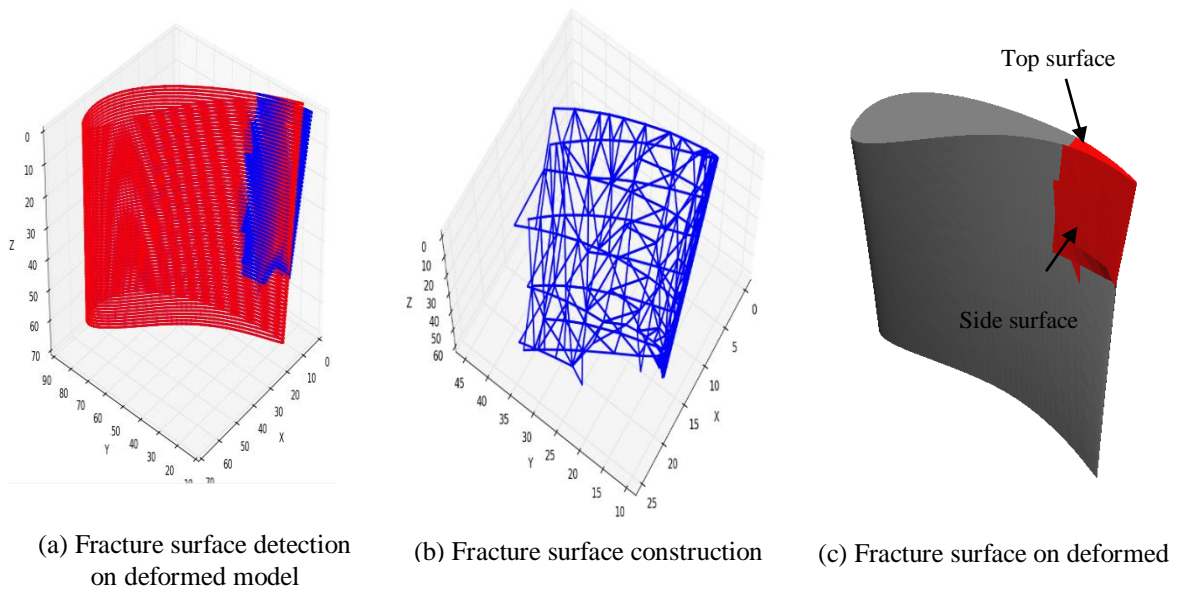


Figure 4.10 Fracture surface construction on deformed blade model

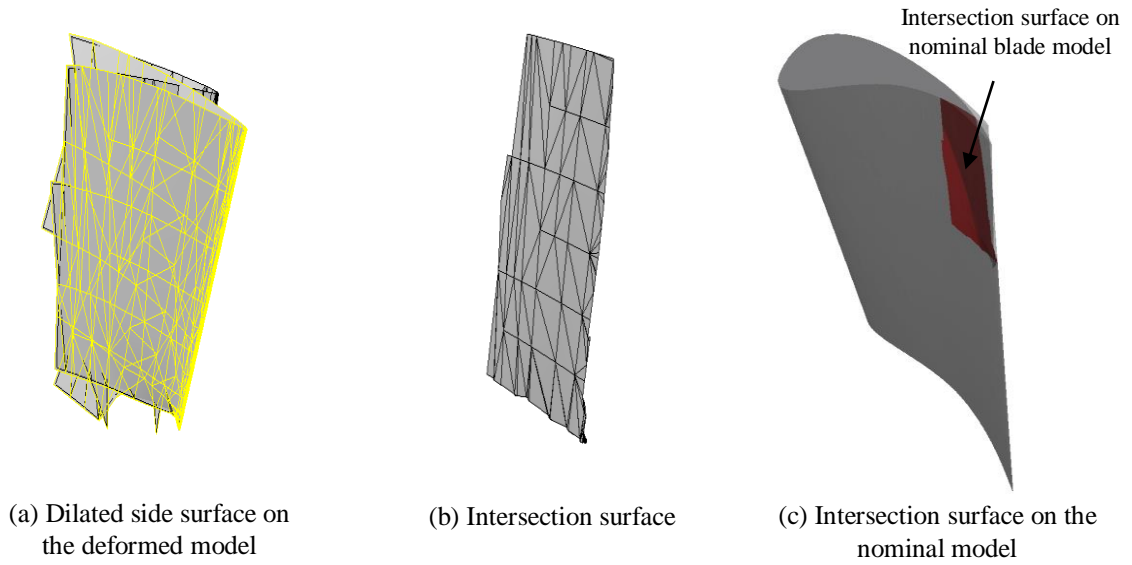


Figure 4.11 Intersection surface on nominal blade

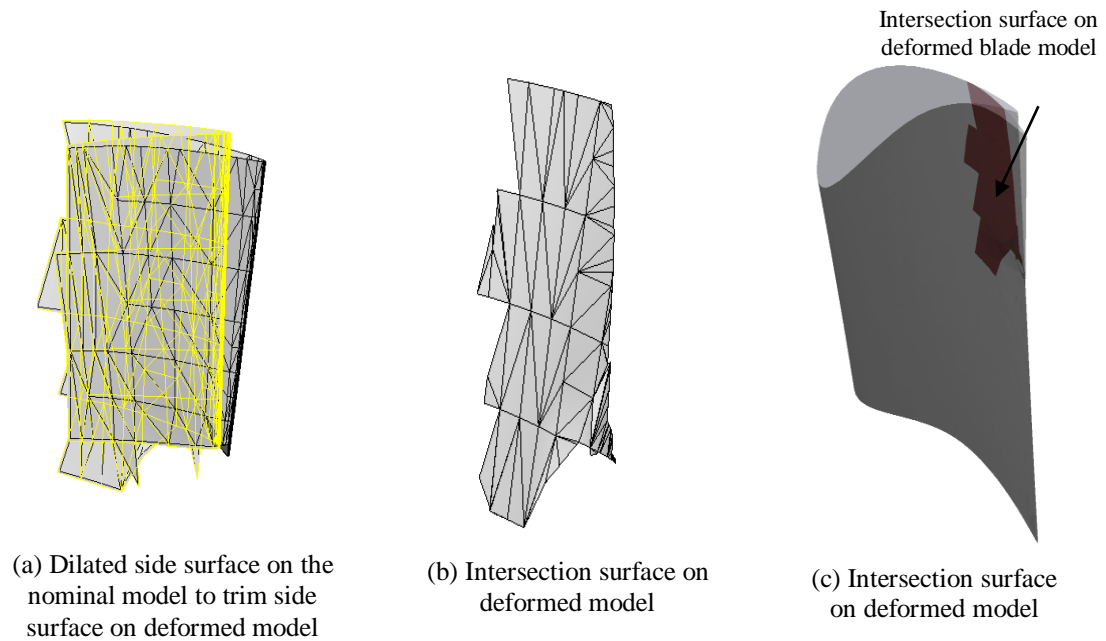


Figure 4.12 Intersection surface on deformed blade

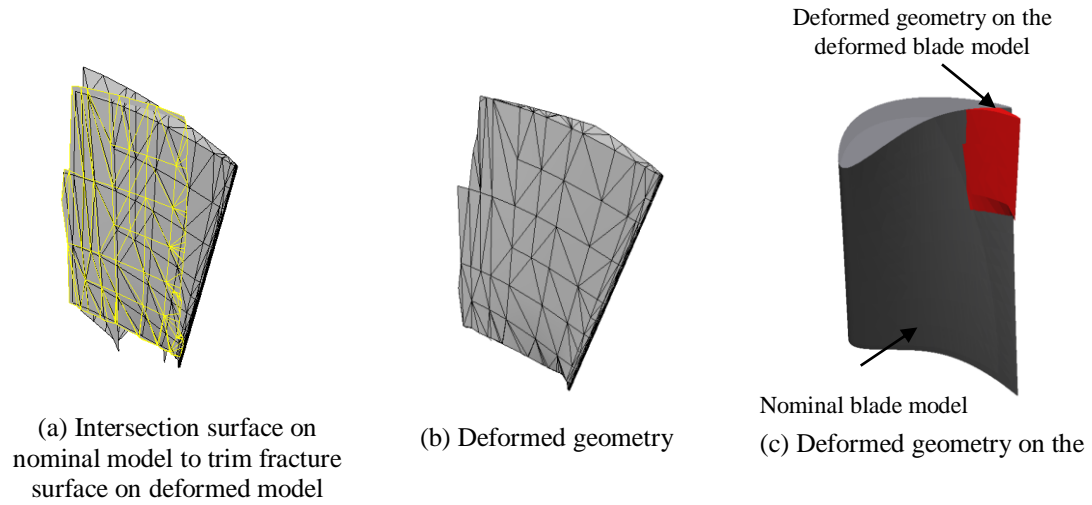


Figure 4.13 Intersection surface trim fracture surface on deformed blade

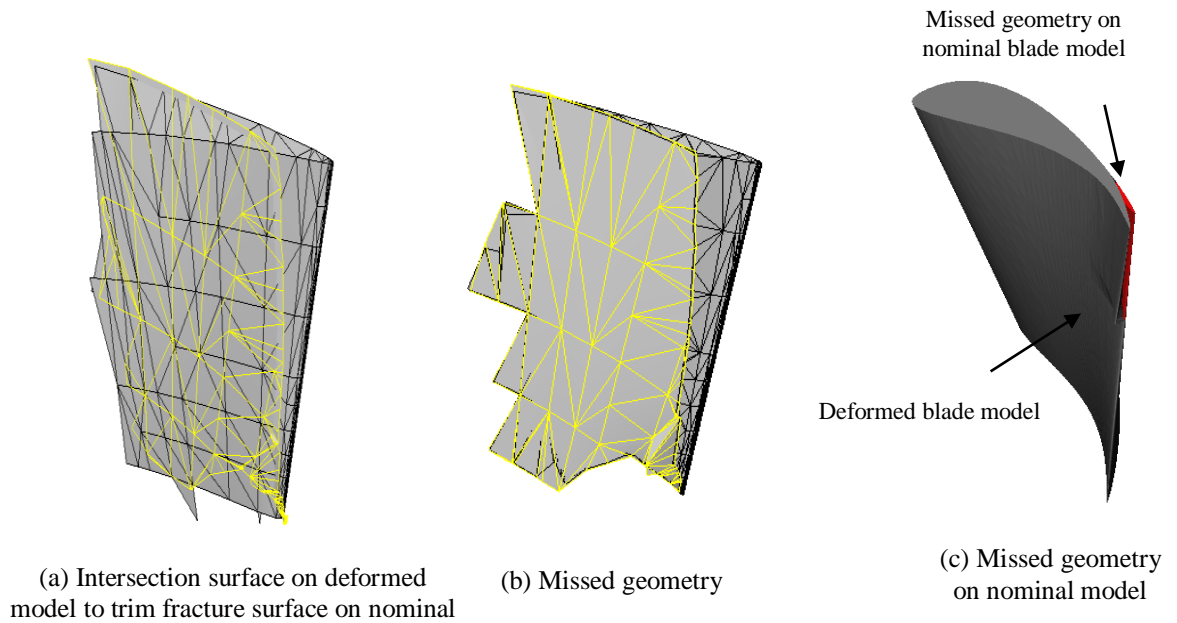


Figure 4.14 Intersection surface trim fracture surface on original blade

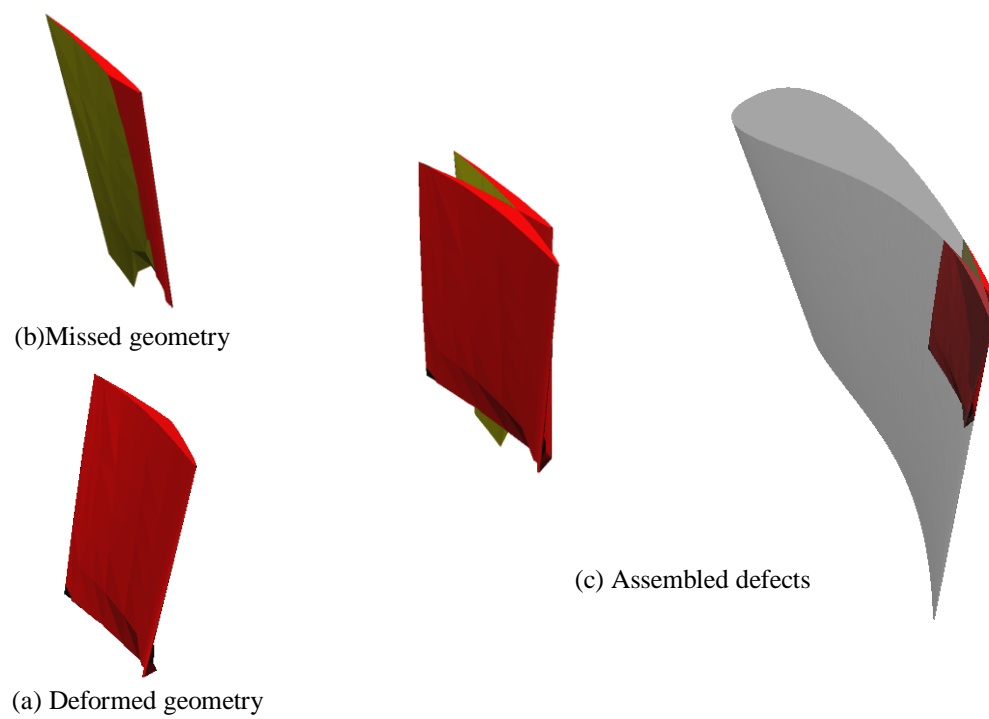


Figure 4.15 Defect reconstruction result for deformed geometry

5. CONCLUSION

In this paper, a multi-feature fitting and shape adaption algorithm is proposed to best-fit the scanned mesh model of worn component and its nominal model and for defect reconstruction. This paper discussed the basic principle, rigid-body best-fit lemma, of multi-featuring-fitting. Multiple features can be used for feature-fitting according to the geometry of the component. Model level's feature fitting and cross-section level's feature-fitting can be combined depends on the dimension of the features and the symmetry of the geometry. The feature-fitting algorithm couples the least-square method and the density-outlier-detection method to approach the best-fit result. Compare with the point-to-surface and surface-to-surface, the feature-fitting method proposed in this paper is much efficient since features are fewer than point cloud or meshes. Meanwhile, the iteration of least-square method and density-based outlier detection method can eliminate the disturbance of defect geometry for the best-fit result. The shape adaption algorithm is based on the cross-section comparison and mesh trim for the defect reconstruction. A fracture 'point-line-surface' detection method is proposed to construct fracture surface of the worn component and then the fracture surface boundary is dilated to trim the nominal 3D model to obtain defect geometry. The whole methodology developed in this paper is illustrated with typical components with different defects. For the broken components, a bearing house, bracket and turbine rotor are demonstrated using the methodology in this paper for symmetric or non-symmetric component, model level feature-fitting solely or with cross-section level-feature fitting to shows the flexibility and capability using the methodology for different geometries. For the deformed geometry, adaptive slicing is used for the curved blade feature construction. The adaptive slicing can be potentially used for the non-complete

geometry's feature construction. As for the shape adaption, intersection surface on the nominal model and deformed model is used to obtained the deformed geometry and missed geometry for defect reconstruction.

ACKNOWLEDGMENT

This research was supported by National Science Foundation Grants IIP-1046492, CMMI-1301414, CMMI-1547042, GNK Aerospace, and Intelligent Systems Center and Material Research Center at Missouri University of Science and Technology. Their support is greatly appreciated.

REFERENCE

- [1] K. Nakata, et al., *Re-weldability of neutron-irradiated stainless steels studied by multi-pass TIG welding*. Journal of Nuclear materials, 2002. 307: p. 1578-1583.
- [2] M. Henderson, et al., *Nickel based superalloy welding practices for industrial gas turbine applications*. Science and Technology of Welding & Joining, 2004. 9(1): p. 13-21.
- [3] J. Tan, L. Looney, and M. Hashmi, *Component repair using HVOF thermal spraying*. Journal of Materials Processing Technology, 1999. 92: p. 203-208.
- [4] A. Gasser, et al., *laser metal deposition (LMD) and selective laser melting (SLM) in turbo-engine applications*. Laser Technik Journal, 2010. 7(2): p. 58-63.
- [5] C. Bremer. *Automated repair and overhaul of aero-engine and industrial gas turbine components*. in *ASME Turbo Expo 2005: Power for Land, Sea, and Air*. 2005. American Society of Mechanical Engineers. p. 841-846.
- [6] J. Wang, et al. *Laser aided part repair-a review*. in *Proceedings of the Thirteenth Annual Solid Freeform Fabrication Symposium, Austin, TX*. 2002.
- [7] W.T. Welsh. *Introduction to CAD-driven reverse engineering*. in *Society of Manufacturing Engineers IMTS Conference*. 2000.
- [8] W.B. Thompson, et al. *Constructing high-precision geometric models from sensed position data*. in *Proceedings 1996 ARPA Image Understanding Workshop*. 1996. p. 987-994.
- [9] R. Sitnik and M. Kujawinska. *Modified high-accuracy 3D shape data conversion system for reverse engineering applications*. in *Lasers in Metrology and Art Conservation*. 2001. International Society for Optics and Photonics. p. 75-82.
- [10] F. Bernardini, et al., *The ball-pivoting algorithm for surface reconstruction*. Visualization and Computer Graphics, IEEE Transactions on, 1999. 5(4): p. 349-359.
- [11] K. Bon-Ki, *Shrink-wrapped boundary face (SWBF) algorithm for mesh reconstruction from unorganized 3D points*. IEICE TRANSACTIONS on Information and Systems, 2004. 87(9): p. 2283-2285.
- [12] C. Bremer. *Adaptive strategies for manufacturing and repair of blades and blisks*. in *ASME Turbo Expo 2000: Power for Land, Sea, and Air*. 2000. American Society of Mechanical Engineers. p. V004T01A010-V004T01A010.

- [13] J. Zheng, Z. Li, and X. Chen, *Worn area modeling for automating the repair of turbine blades*. The International Journal of Advanced Manufacturing Technology, 2006. 29(9-10): p. 1062-1067.
- [14] J. Zheng, Z. Li, and X. Chen, *Broken area modeling for repair automation*. Journal of Advanced Manufacturing Systems, 2004. 3(02): p. 129-140.
- [15] V. Avagyan, A. Zakarian, and P. Mohanty, *Scanned three-dimensional model matching and comparison algorithms for manufacturing applications*. Journal of Manufacturing Science and Engineering, 2007. 129(1): p. 190-201.
- [16] B. Stimper, *Using laser powder cladding to build up worn compressor blade tips*. 2003, Technical report MTU Aero engines.
- [17] ISOTEK. *Aerospace cladding applications*. Available from: <http://www.isotek.co.uk>.
- [18] J. Gao, et al., *An integrated adaptive repair solution for complex aerospace components through geometry reconstruction*. The International Journal of Advanced Manufacturing Technology, 2008. 36(11-12): p. 1170-1179.
- [19] J. Gao, et al., *Adaptive restoration of complex geometry parts through reverse engineering application*. Advances in Engineering Software, 2006. 37(9): p. 592-600.
- [20] G. Jian, et al., *Adaptive repair approach for recovering components from defects*. Chinese Journal of Mechanical Engineering, 2008. 21(1).
- [21] O. Yilmaz, N. Gindy, and J. Gao, *A repair and overhaul methodology for aeroengine components*. Robotics and Computer-Integrated Manufacturing, 2010. 26(2): p. 190-201.
- [22] C. Piya, et al. *Virtual repair: geometric reconstruction for remanufacturing gas turbine blades*. in *ASME 2011 International Design Engineering Technical Conferences and Computers and Information in Engineering Conference*. 2011. American Society of Mechanical Engineers. p. 895-904.
- [23] J. He, L. Li, and J. Li. *Research of key-technique on automatic repair system of plane blade welding*. in *Control, Automation and Systems Engineering (CASE), 2011 International Conference on*. 2011. IEEE. p. 1-4.
- [24] P. Bourke, *Calculating the area and centroid of a polygon*. 1988.
- [25] C.B. Barber, D.P. Dobkin, and H. Huhdanpaa, *The quickhull algorithm for convex hulls*. ACM Transactions on Mathematical Software (TOMS), 1996. 22(4): p. 469-483.

- [26] H. Freeman and R. Shapira, *Determining the minimum-area encasing rectangle for an arbitrary closed curve*. Communications of the ACM, 1975. 18(7): p. 409-413.
- [27] M.W. Spong and M. Vidyasagar, *Robot dynamics and control*. 2008: John Wiley & Sons.
- [28] C.J. Taylor and D.J. Kriegman, *Minimization on the Lie group $SO(3)$ and related manifolds*. Yale University, 1994. 16: p. 155.
- [29] M.M. Breunig, et al. *LOF: identifying density-based local outliers*. in *ACM sigmod record*. 2000. ACM. p. 93-104.
- [30] K. Eiamsa-ard, et al. *Part repair using a hybrid manufacturing system*. in *Proceedings of the Sixteenth Annual Solid Freeform Fabrication Symposium, Austin, TX*. 2005.
- [31] C.-H. Richter, *Structural design of modern steam turbine blades using ADINA™*. Computers & structures, 2003. 81(8): p. 919-927.
- [32] K. Mohaghegh, M. Sadeghi, and A. Abdullah, *Reverse engineering of turbine blades based on design intent*. The International Journal of Advanced Manufacturing Technology, 2007. 32(9-10): p. 1009-1020.
- [33] J. Gao, et al., *Investigation of a 3D non-contact measurement based blade repair integration system*. Aircraft Engineering and Aerospace Technology, 2005. 77(1): p. 34-41.
- [34] J. Jones, et al. *Remanufacture of turbine blades by laser cladding machining and in-process scanning in a single machine*. in *Twenty-Third International Solid Freeform Fabrication Symposium in Austin, . 2012. Austin, TX, USA*. p. 821-827.

PAPER

II. A SMOOTH TOOLPATH GENERATION METHOD FOR LASER METAL DEPOSITION

Renwei Liu, Zhiyuan Wang, Yunlu Zhang, Todd Sparks, Frank Liou

Department of Mechanical and Aerospace Engineering,
Missouri University of Science and Technology, Rolla, MO, 65401

ABSTRACT

The conventional contour and zigzag toolpath pattern for laser metal deposition are not smooth at turn points or corner points. The unsmooth toolpath causes uneven deposition, which brings height variation and porosity problems. This paper aims to develop a smooth toolpath generation method for laser metal deposition to improve the deposition quality. A parametric curve equation based on trigonometric functions is derived and built. It can be used for arbitrary smooth connections or transitions in toolpath planning and provide constant feedrate for deposition. The proposed method was applied to a patch deposition experiment and a component repair experiment with Ti-6Al-4V powder. The experimental results show that the smooth toolpath can noticeably improve the dimensional accuracy and surface roughness and reduce porosity.

Keywords: Laser metal deposition; Tool path generation; Additive manufacturing.

1. INTRODUCTION

Additive Manufacturing (AM) is defined by ASTM F42 Technical Committee as the “process of joining materials to make objects from 3D model data, usually layer upon layer, as opposed to subtractive manufacturing methodologies” [1]. Traditional manufacturing processes require analysis of the part geometry to determine the order in which different features can be fabricated and if tools and fixtures may be needed. In contrast, AM technology significantly simplified the process of producing complex 3D objects directly from CAD data and needs only some basic understanding of how the AM machine works, the materials that are used to build the part, and dimensional details [2]. Among AM processes, Laser Metal Deposition (LMD) is an additive process that can build up full density metallic components directly from the CAD model using a focused laser beam to locally melt metal powder or wire. The applications of the LMD process include the direct metallic components fabrication [3, 4]; Functionally graded materials (FGM) parts with multiple powder hoppers with different materials [5, 6]; repair for high value components like turbine blades, engine combustion chambers, and etc [7, 8].

For the AM process to be widely accepted by the industry, the ability of predictable, repeatable, consistent, uniform fabrication is critical. The building process-structure-property relationships modeled and integrated with CAD/E/M tools for each material and process are needed [9]. A desirable depositing toolpath can not only improve dimensional accuracy and obtain desired material microstructure properties, but also save the building time and forming materials. The LMD process is dynamically complex process with phase change and usually requires sophisticated model to describe the relationships between the process input (e.g., laser power, scan speed and material mass flow rate) and the quantities

of interest, which include the melt pool dimension and temperature [10]. Therefore, the path planning for LMD is not only a geometric problem to generate the guide path for the nozzle move along, but also a physical problem which combine the path with the process input to obtain dimensional accuracy and material microstructure properties. Precious research for LMD path planning mainly on optimizing the path planning method about solving the geometric problem. Adaptive slicing with non-uniform layer thickness was proposed in paper [11, 12] to save building time, multi-axis path planning with changing slice direction and without building support structure for overhang part [13, 14]. For single layer path planning, there are two main toolpath planning strategies in LMD path planning generation, also for AM: the zigzag toolpath pattern and contour offsetting toolpath pattern as shown in Figure 1.1 [15]. As can be seen from Figure 1.1 (a), the nozzle moves back and forth along zigzag path pattern to deposit material to fill up each single layer. Different from zigzag path pattern, the offsetting toolpath pattern in Figure 1.1 (b) adopts successive offsets of the cross-section boundary as the toolpath elements. Since linear connection or transition in the toolpath at the turn points and corner points, both of zigzag path pattern and contour offsetting path pattern are discontinuous. Due to the discontinuity of the zigzag path pattern and contour offsetting path pattern, the nozzle undergoes acceleration and deceleration at the turning points (i.e., decelerate the nozzle to zero speed at the turn point and accelerate to the predefined speed from the turn point). As Figure 1.2 shows, the feedrate change at a turn point or corner point is correlated with the angle between adjacent path segments with the assumption that keep the constant feedrate value. The change of the vector feedrate f is $2f * \sin(\alpha/2)$, where f is the feedrate, and α is the angle between the current path segment and the extension of the previous segment. Therefore, the non-smooth

path pattern may cause overfilling or vibration at the turn points or the corner points from the beginning of the acceleration process to the end of the deceleration process. For repair, it may also cause uneven surface and porosities at the boundary between deposited area and base material [16, 17]. The discontinuity problem that also exists in pocketing milling, especially for high-speed machining (HSM), was discussed in the papers [18-20]. Arc or bi-arc segments were used to connect or transit the zigzag toolpath or contour-offsetting path for pocketing milling. However, arc segments might not be robust enough for arbitrary toolpath connection or transition in AM tool path planning.

There has been a little work on smooth tool path generation for LMD. In order to improve the evenness of adjacent passes or layers, the focus of this work is to find a general solution to realize any kinds of connection or transition for 2D/3D deposition toolpaths and get an entire smooth toolpath. Vibration test with the tool path planning is also studied and the proposed method was applied to a patch deposition experiment and a component repair experiment.

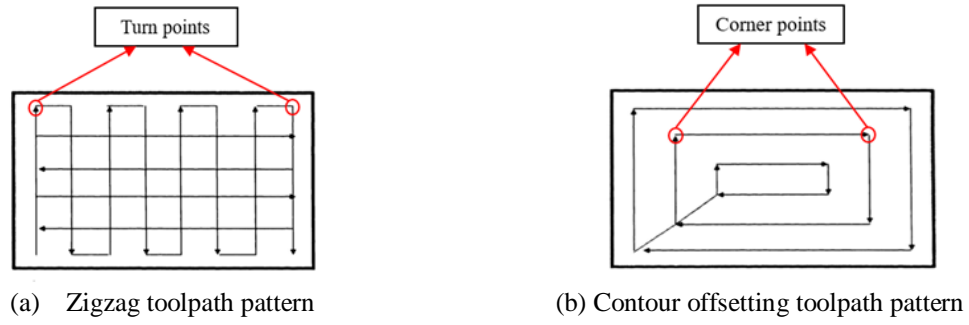


Figure 1.1 Two main toolpath planning strategies in AM

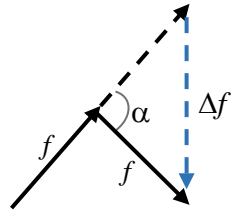


Figure 1.2 Feedrate change at turning/corner points

2. RELATED WORKS

Toolpath for LMD is a predefined trajectory along which the nozzle is driven to deposit metallic powder or wire melt by focused laser beam to build 3D component layer by layer. As depositing quality (e.g. surface roughness, dimensional accuracy and mechanical properties) are influenced by the toolpath as well as some other deposition parameters, many efforts involving toolpath planning to optimize it. Currently, offset toolpath pattern and zigzag toolpath pattern are mainly employed in LMD with their own pros and cons respectively. In the offset pattern, offset segments of the geometry boundaries are constructed and used as trajectory for the nozzle to move along. It mainly includes contour-parallel path and spiral-like offsetting path. Therefore, offset toolpath pattern can get better surface accuracy of the boundary. The problem is the computation cost to detect the intersection of offset edges and removing invalid loops and numerically stable [21-23]. When the geometry has multi-cavity structures, the shapes of boundaries tend to be comparatively complex for offset toolpath planning. Meanwhile, offset toolpath may bring about more uncut toolpaths when it comes to sharp corner points in the toolpath. To reduce the computation complexity for toolpath planning for the whole deposition layer, an optimized method which divides the deposition layer into several regions for while the offsetting paths is generated for every single region component [3]. The geometry skeleton based offsetting toolpath generation method was introduced to reduce void and gap area brings by uncut toolpath [24]. By contrast, zigzag toolpath contains series path segments corresponding to back and forth motion in a fixed direction within the boundary to fill up the interior part. This approach is comparatively simple and fast to realize at the expense of manufacturing accuracy. The common zigzag pattern follows the longest side of the

geometry results in the shortest deposition path. The problem for zigzag pattern is the existence of vast number of turn points in the toolpath to bring about exacerbation of fabricating quality and efficiency. With different direction angle of the zigzag path, the total path length and idle path number could be different. Optimal direction angle for zigzag path generation was studied in paper [25] to reduce the ratio of the idle path. Another problem of zigzag path pattern is the warpage of forming material as the tool-path is along the same direction in one specific layer, which can be alleviated by the offset toolpath. In order to fulfill the merits of these two approaches, it is suggested that offset toolpath be used for the boundaries for achieving good surface smoothness and zigzag toolpath filling be used for the interior regions for achieving required part strength as well as acceptable machining efficiency.

The previous research for the LMD path planning mainly focus on optimize the toolpath generation algorithm to simplify the computation complexity, short the building time and improve the dimensional accuracy. But the conventional zigzag toolpath and contour toolpath pattern are still discontinuous at turn points or corner points. The unsmooth toolpath causes uneven deposition, which brings height variation and porosity problems. On the other aspect, the toolpath is not independent from the deposition parameters (e.g., laser power, scan speed and material mass flow rate). For example, a predefined layer thickness and toolpath interval needs to match the actual values which determined by the input parameters and also the material itself. Otherwise, the deposited material geometry will be different with the desired geometry defined by toolpath and cause the whole deposition fail.

The objective of this paper is to improve the evenness of adjacent passes or layers through a smooth toolpath generation method. The smooth toolpath motion will provide a constant deposition feedrate for the entire deposition toolpath. With the smooth toolpath, deposition idle time is also controlled for each single deposition pass to obtain an even deposition during whole deposition process. Vibration test is adopted to measure the acceleration along the deposition toolpath motion. The rest of this paper is organized as following: Section 3 discuss the discontinuity problem definition of toolpath planning in AM and gives a general solution for the problem. The laser metal deposition experiment, vibration test and microstructure study are presented in Section 4. Finally, it gives a conclusion.

3. METHODOLOGY

This section will first discuss and define the discontinuous problem in toolpath planning of AM and then derive a general solution according to the problem definition. Smooth toolpath examples will be given by applying the proposed method.

3.1. PROBLEM DEFINITION AND SOLUTION

The discontinuous problem happens in the turn points or corner points in the toolpath planning. Because the zigzag toolpath pattern and the contour offsetting toolpath pattern are two main toolpath planning strategies, an example of an outside contour toolpath with an inner zigzag toolpath example shown in Figure 3.1 is presented to analyze different types of connection or transition that need to be dealt with. As shown in Figure 3 (a), there is a 3D model of the number '3' with several corner points at the contour. Conventional contour and zigzag toolpaths are generated according to the slice of the 3D model. As shown in Figure 3 (b), there are four types of connections or transition discussed as follows:

- Connection between zigzag toolpath as shown at position ①. Turn points existed from depositing path to non-depositing path and vice versa. Linear connection makes the zigzag toolpath discontinuous.
- Connection of toolpath elements as shown at position ②. It is usually impossible to fill up a layer with only one piece of zigzag toolpath or contour toolpath when handling complex shapes. After the generation of sub-paths,

these sub-paths need to be connected or contour toolpaths need to be connected with zigzag paths.

- Connection of adjacent layers as shown at position ③. When finished with the current layer manufacturing, the nozzle needs to be moved to the next layer.
- Transition of corner points for contour toolpath as shown at position ④. Corner points happen in the non-smooth contour toolpath; it needs a smooth transition to avoid discontinuous problems.

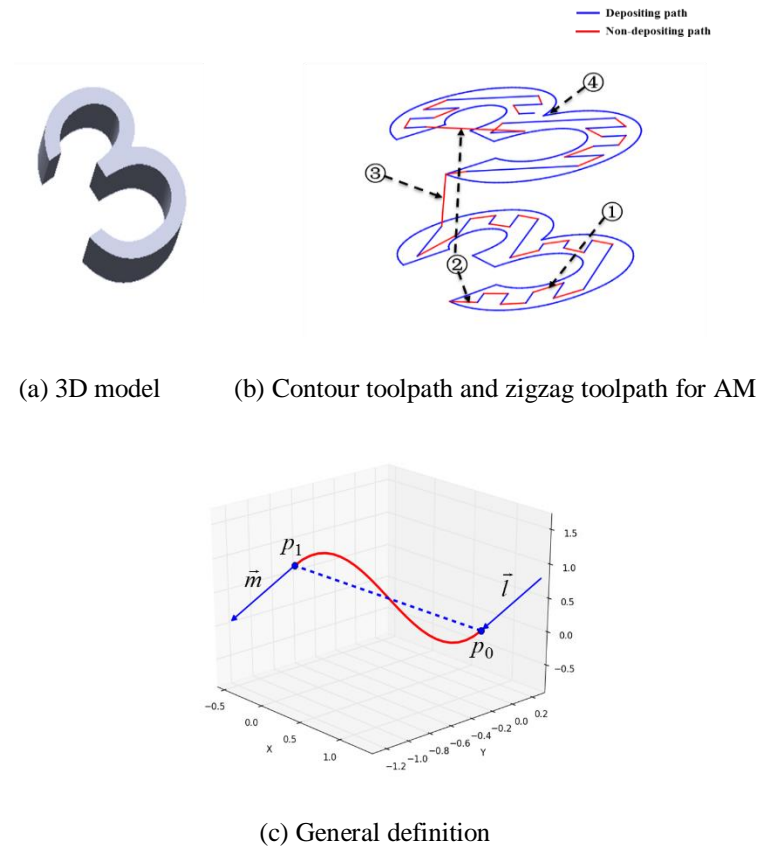


Figure 3.1 Problem definition of discontinuous toolpath in AM

As Figure 3.1 (c) shows, the connection or transition problem can be generally defined as building a curve instead of linear connection to connect arbitrary start point p_0 with travel direction \vec{l} and end point p_1 with travel direction \vec{m} . The curve also should share common tangent direction with travel direction \vec{l} , \vec{m} at the joint points p_0, p_1 . When $p_0 \neq p_1$, it is connection problem; otherwise, it is transition problem. A parametric curve equation described in Equation (1) is derived and built based on three trigonometric functions and three vectors to provide a general solution for smooth connection or transition.

$$\vec{s}(t) = \vec{p} + f(t) * \vec{u} + g(t) * \vec{v} + l(t) * \vec{w} \quad (1)$$

where \vec{p} is the start point p_0 ; the parameter of the curve is $t \in [0, \pi/2]$; the three trigonometric functions are $f(t) = \sin(t)$, $g(t) = 1 - \cos(t)$, $l(t) = (1 - \cos(2t))/2$; the three vectors are $\vec{u} = r * \vec{l}$, $\vec{v} = r * \vec{m}$, $\vec{w} = p_1 - p_0 - r * \vec{l} - r * \vec{m}$; and r is the scale coefficient to control the size of the curve. There are four main properties of this parametric curve equation:

- (1) The parametric equation satisfies the problem definition: when $t=0$, $\vec{s}(0) = p_0$ and $\vec{s}'(0) = \vec{l}$; when $t = \pi/2$, $\vec{s}(\pi/2) = p_1$, $\vec{s}'(\pi/2) = \vec{m}$.
- (2) The parametric curve is C^n continuous and meets with the depositing toolpath with C^1 continuity [26].
- (3) When scale parameter r is 0, the curve equation becomes a linear equation.
- (4) When $p_0 \neq p_1$, it is connection curve; when $p_0 = p_1$, it is transition curve.

Mathematically, the connection or transition of a conventional toolpath is C^0 continuous. The parametric curve generated by Equation (1) has infinite derivatives, which is C^n continuous and meets with the depositing toolpath at the joint point with C^1 continuity. As discussed before, the feedrate change at a turn point or a corner point depends on the angle between adjacent path segments in the conventional zigzag tool path or contour tool path. Using the smooth curve, the angle between adjacent path segments at a turn point or a corner point is close to zero after interpolation. Therefore, the smooth toolpath offers a constant speed for the depositing toolpath. The scale parameter r in the three vectors of Equation (1) can control the size of the curve, which can potentially provide adaptive idle time for each single path during the deposition. The parametric curve is a robust, flexible, and efficient solution for arbitrary 2D/3D toolpath connection or transition.

3.2.SMOOTH TOOLPATH EXAMPLES

This subsection gives smooth toolpath examples generated by the proposed method. A smooth zigzag toolpath example is generated for a patch deposition as shown in Figure 3.2 (b), compared with a conventional non-smooth toolpath as shown in Figure 3.2 (a). A smooth curve is adopted to connect each single path in each layer and adjacent layers (the blue line represents the depositing toolpath and the red line represents the non-depositing toolpath). The raster direction of adjacent layers changed to get interlaced zigzag toolpath and to shorten the travel time from current layer to the next layer. A smooth transition toolpath example for contour toolpath is shown in Figure 3.3. Smooth transitions for corner points and smooth connections between connective layers are obtained using the proposed smooth toolpath generation method. Different transition curve sizes are defined

corresponding to the different scale coefficients described in Figure 3.3 (a), (b), and (c). The smooth toolpath generation method is also applied to optimize the toolpath generation for a component repair. As shown in Figure 3.4 (a), there is a hole defect in the component. The defect area is scanned to get point cloud as described in Figure 3.4 (b). Then, the convex hull algorithm is used to obtain the slices and the toolpath, which includes the outside contour toolpath and the inside zigzag toolpath can be generated by the raster toolpath generation method [16]. Figure 3.4 (c) shows the optimized toolpath by smooth connection and transition.

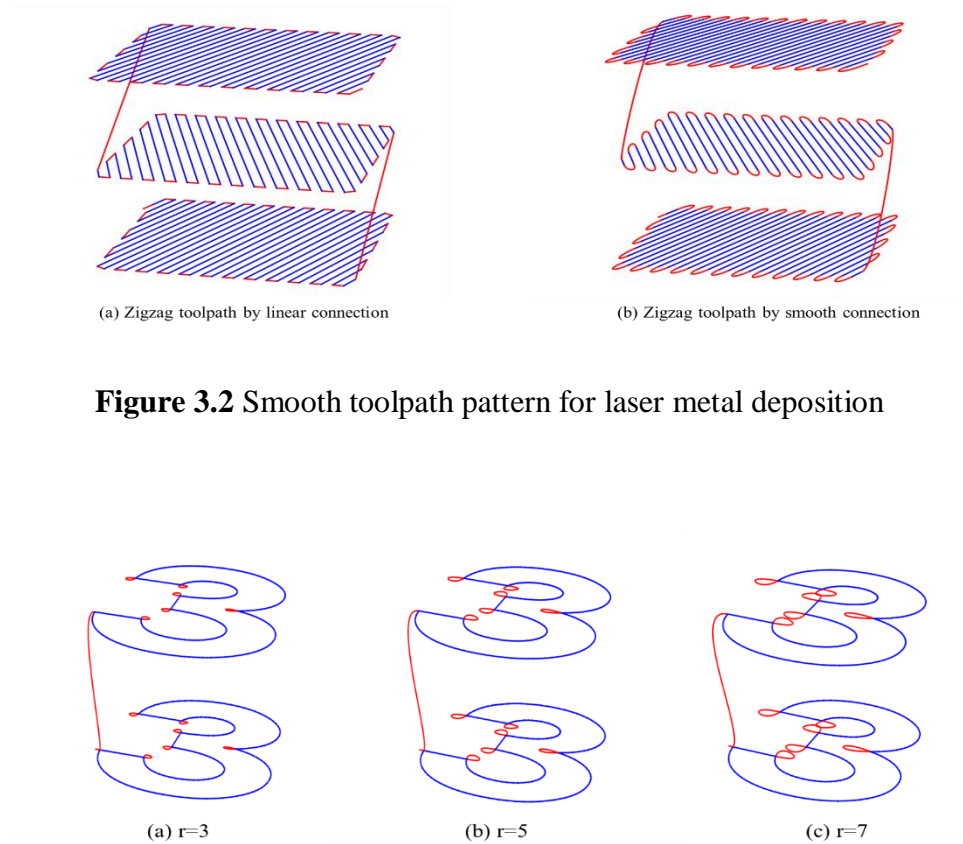
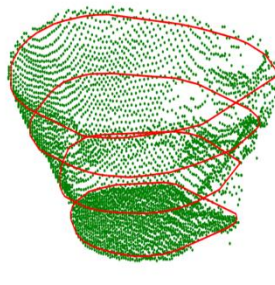


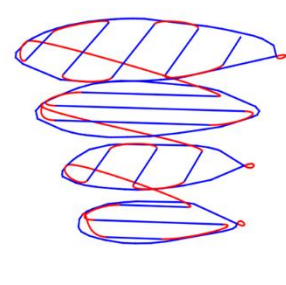
Figure 3.3 Contour toolpaths by smooth transition with different curve size



(a) A hole defect area on component



(b) Convex hull of point-cloud



(c) Smooth toolpath pattern for repair

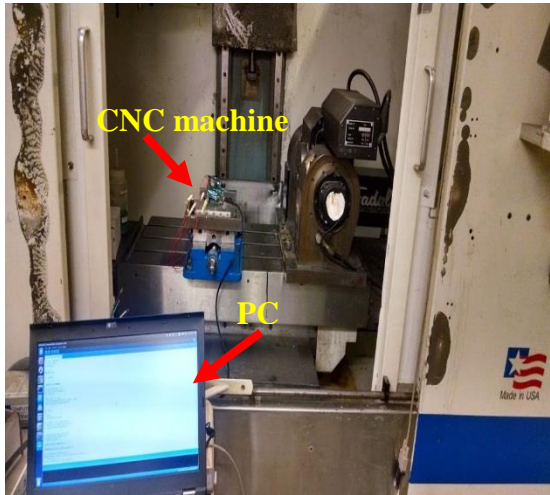
Figure 3.4 Optimized toolpath using smooth toolpath generation for repair

4. EXPERIMENTS

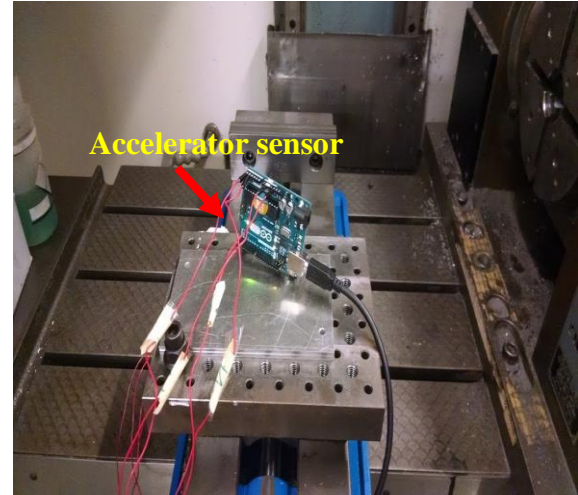
4.1.VIBRATION TEST

Vibration test is implemented to measure the vibration of non-smooth and smooth zigzag tool path. The overview of the vibration test system layout as shown in Figure 4.1. The hardware includes CNC machine, a three-axis ADXL345 accelerometer, Arduino board, and a laptop PC. The deposition tool path is uploaded to CNC for the motion, meanwhile, accelerometer doing measurement, Arduino board acquires data and transfers data to laptop for data collection. Along with the motion of the deposition path, the acceleration of X, Y, Z axis was measured respectively. In this paper, the vibration test was adopted to measure the acceleration of two layers' non-smooth zigzag toolpath and its smooth zigzag toolpath generated by proposed method as shown in Figure 4.2. The inclination angle with respect to x-axis in this toolpath generation is $\alpha = 45^\circ$. For the whole deposition path, the feedrate is keep in constant value 1000 mm/min. Three-axis acceleration measurement plot is shown in Figure 4.3. From the plot in Figure 4.3 (a) we can see the peak acceleration value happens at each turn point of the non-smooth zigzag toolpath since the change of the vector feedrate f is $2f * \sin(\alpha/2)$ at the turn point. But for the smooth zigzag toolpath, the angle change of the vector feedrate is close to 0. But it still has acceleration because of the smooth connection curve is interpolated with small linear segments. The peak acceleration value of the smooth zigzag path happens at the intermediate point of linear segments of the smooth connection curve. The acceleration range of those toolpath is summarized in Table 4.1 and the maximal acceleration value

reduce 40% in X axis and 20% in Y axis. Since the only acceleration happens at adjacent layers' connection, we don't consider Z axis acceleration for the comparison.



(a) CNC machine and PC



(b) Arduino board and accelerometer sensor

Figure 4.1 The layout of vibration test system

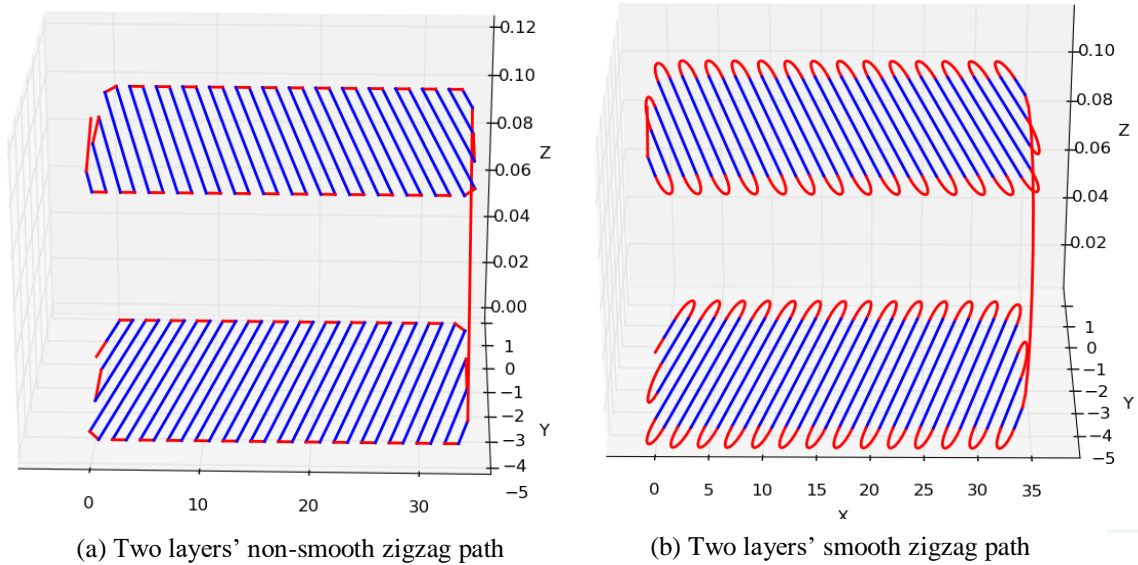
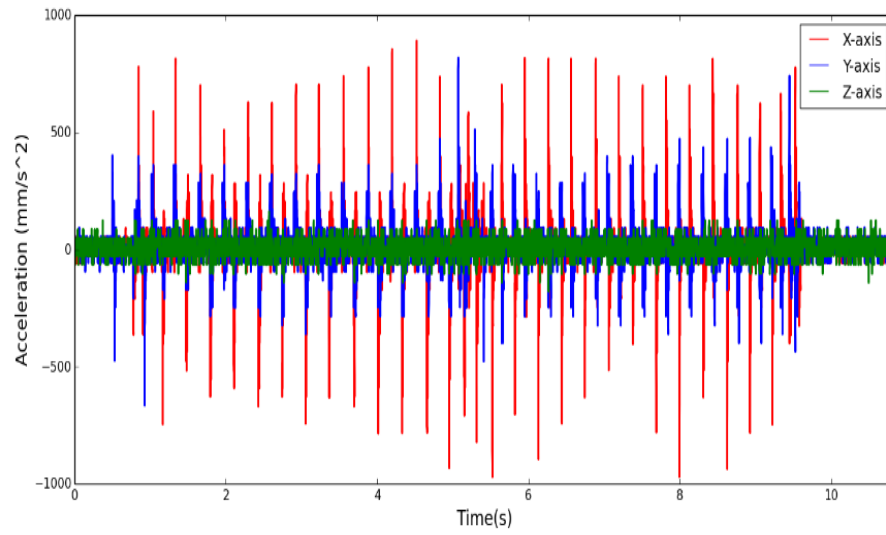
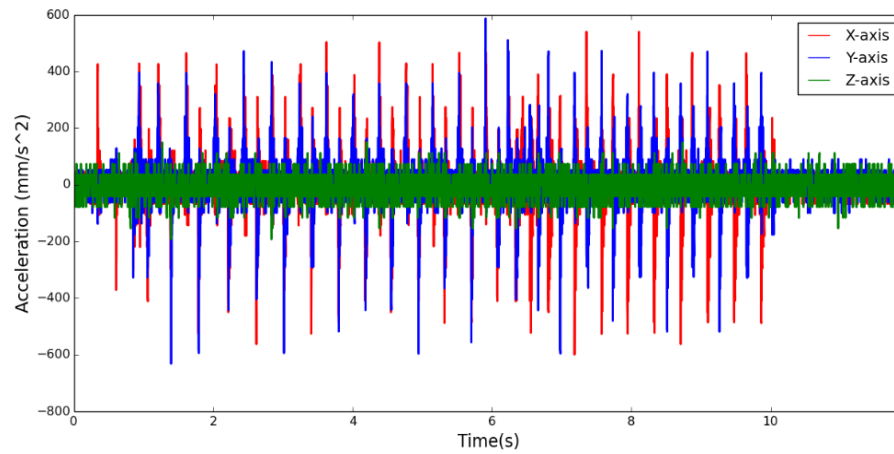


Figure 4.2 Tool path for vibration test



(a) Non-smooth tool path



(b) Smooth tool path

Figure 4.3 Acceleration measurement plot

Table 4.1 Acceleration measurement result

Axis	Acceleration range of non-smooth zigzag path (Unit: mm/S²)	Acceleration range of smooth zigzag path (Unit: mm/S²)
X	[-977.119, 884.607]	[-599.681, 540.099]
Y	[-669.295, 815.593]	[-631.543, 586.731]
Z	[-171.399, 169.549]	[-192.512, 149.627]

4.2.LASER METAL DEPOSITION EXPERIMENT

Deposition experiments were implemented at Missouri S&T laser-aided manufacturing process (LAMP) lab using the LMD system, which consists of an argon-purged chamber, a 1 kW Nd-YAG fiber laser, a side nozzle powder feeder, and 3-axis numerical control work table. Figure 4.4 shows the experimental set-up of the LAMP LMD system.

A patch deposition experiment using Ti-6Al-4V powder was implemented to demonstrate the difference using the smooth zigzag toolpath and the non-smooth zigzag toolpath described in Figure 3.2. The metal powder used for this experiment is Ti-6Al-4V alloy with a size distribution of -60 +120 mesh. It has a chemical composition of 6.33% aluminum, 4.1% vanadium, 0.17% iron, 0.19% oxygen, and the remainder is titanium. The parameters for the patch deposition are shown in Table 4.2 and the parameters are chosen according to previous deposition tests. As shown in Figure 4.5, the deposition experimental results demonstrate that the surface roughness and dimensional evenness is noticeably improved using the smooth zigzag toolpath compared with the non-smooth zigzag toolpath. During the deposition, the tool path come out for non-depositing

movement (instead of moving along the deposited edge) and then come in for depositing movement. It avoids add more powders to the melt pool on the edge. The smooth parametric curve provides smooth transition from the depositing path to the non-depositing path. In other words, it provides constant deposition feedrate for the depositing tool path to reduce the height variation causes from feedrate change. Another experiment using smooth tool path is for component repair, hybrid manufacturing process which integrates LMD process with CNC machining process is adopted to repair a hole defect. As Figure 4.6 (a) shows, there is a hole defect on a Ti-6Al-4V component. After scanning, the deposition toolpath is generated and described in Figure 3.4 (c). Figure 4.6 (b) shows the deposition result after filling the defect area, and Figure 4.6 (c) shows the result after machining and polishing. The repair experiment results show that there are no obvious porosities inside the deposition area or at the boundary between base material and deposition material using the optimized toolpath.

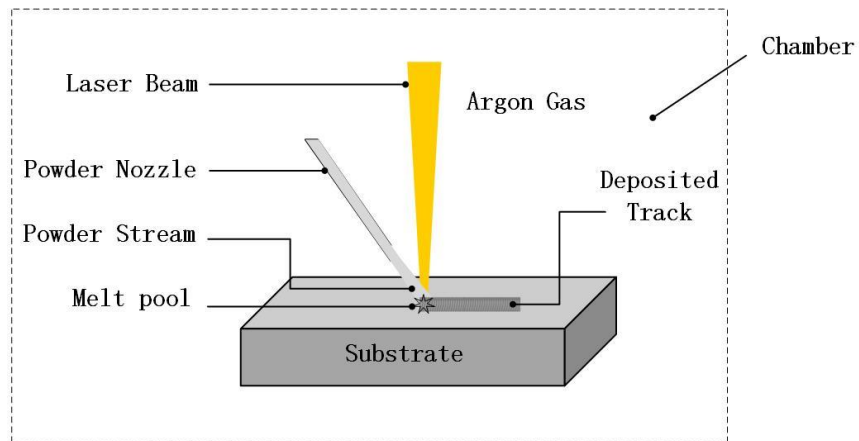
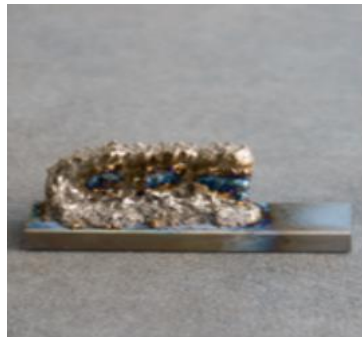


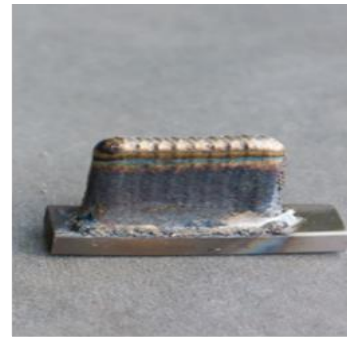
Figure 4.4 Schematic of the MST-LAMP LMD system

Table 4.2 Parameters for patch deposition

Parameter	Value
Power feed rate	20 g/min
Traverse speed	600 mm/min
Deposition power	1.0 kw
Layer thickness	0.15 mm
Track width	2.0 mm
Overlap	0.5



(a) Deposition with non-smooth zigzag toolpath



(b) Deposition with smooth zigzag toolpath

Figure 4.5 Experimental results by smooth toolpath generation for laser metal deposition



(a) A hole defect on component

(b) After deposition

(c) After machining and polishing

Figure 4.6 Repair experimental results**Table 4.3** Parameters for repair experiment

Parameter	Value
Power feed rate	20 g/min
Traverse speed	1000 mm/min
Preheat power	0.7 kw
Deposition power	1.0 kw
Layer thickness	0.035 mm
Track width	2.0 mm
Overlap	0.5

4.3.MICROSTRUCTURE STUDY

The repaired part was cut into four slots (① ② ③ ④) as shown in Figure 4.7 (a), which contain the repaired area, deposition affected area and substrate to evaluate the microstructure features of the samples. The view angle for each sample is specified in Figure 4.7 (b) showing that cross section of all four samples were examined.

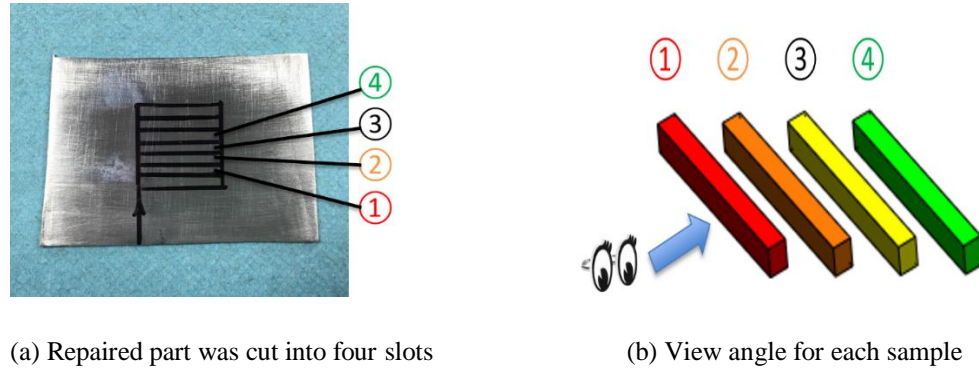


Figure 4.7 View angle for samples

Figure 4.8 shows images obtained by optical microscope of four samples ((1) (2) (3) (4)) of the repaired part, in which, I shows the transition edge of heat affected zone and substrate, II shows the central region of melting pool and III shows the heat affected zone which below the melting pool and not melt during laser deposition process.

It can be noted from Figure 4.8 (I) that each layer of the repaired area combined well with each other which ensuring the strength between each layer and the repaired area has metallurgically combined well with Ti-64 substrate. No defects were detected. Due to the phase grows from one layer to another and combined well with each other, there is no obvious layer characteristic among the deposition area. Figure 4.8 (II) shows that the melting pool area is dominated by martensite with mixed α and β phase and shows typical basket weave structure. The acicular α phases were developed when cooling down from the β transition temperature and the volume of α phases increases in the subsequent laser passes due to decrease of cooling rate. It can be observed from Figure 4.8 (III) that there are columnar crystal grain boundaries. Further investigation shows that the heat affected zone was consisted of primary equiaxed α phase as well as some α martensite.

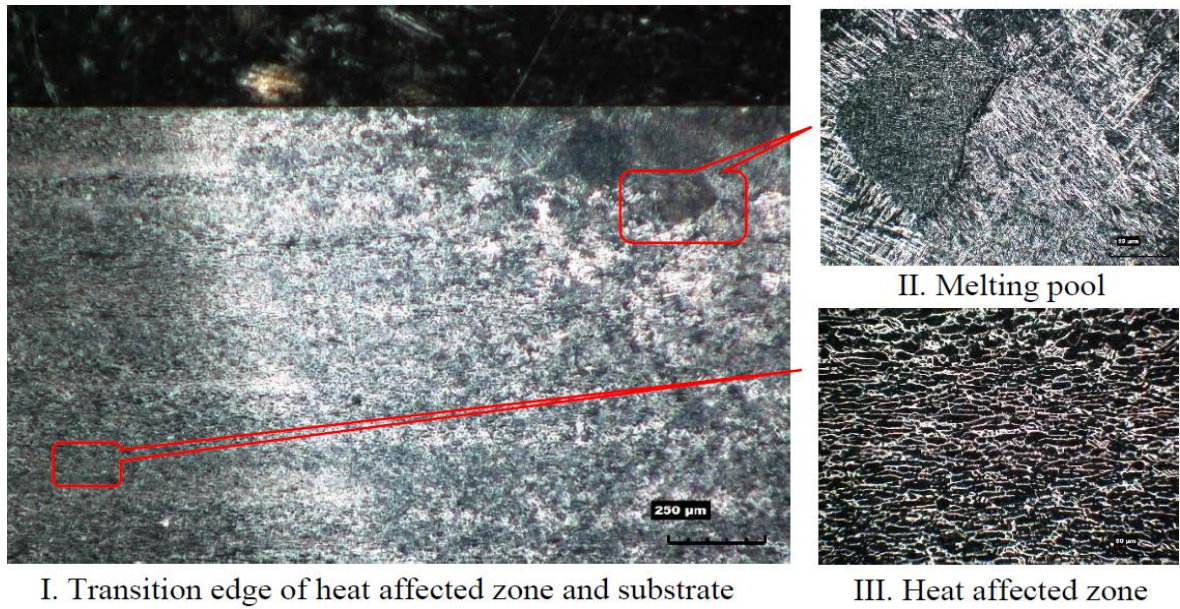


Figure 4.8 Sample microstructure of the repaired part. (a) Microstructure of sample 1.

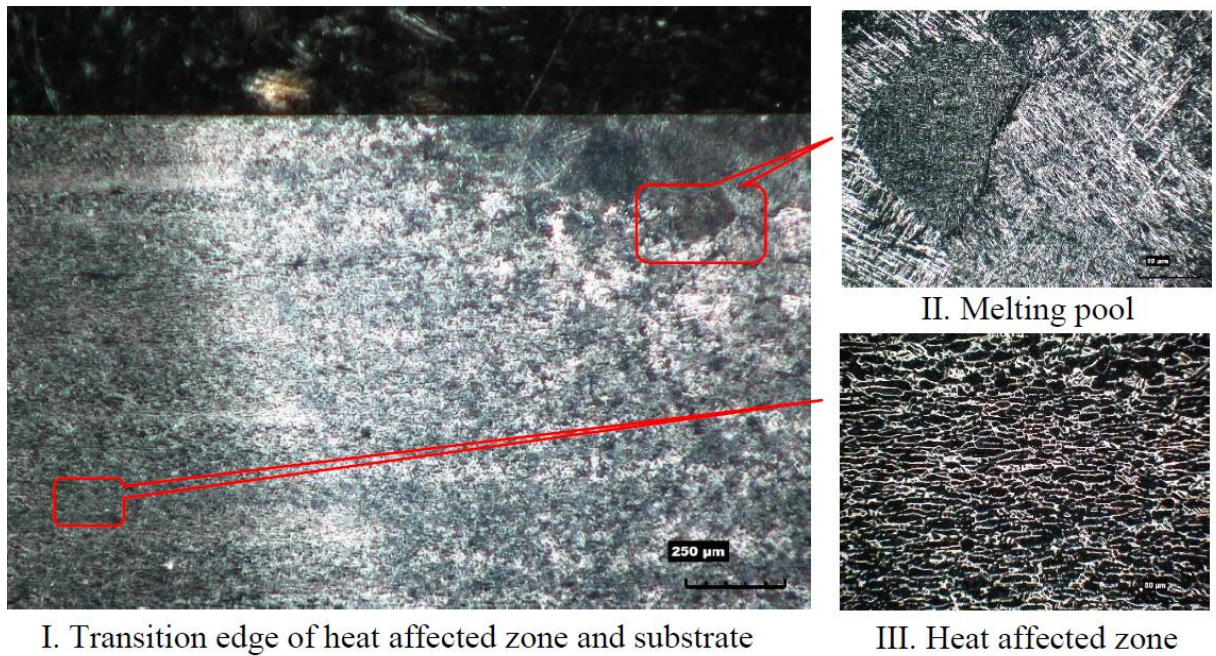


Figure 4.8 Sample microstructure of the repaired part. (b) Microstructure of sample 2.
(cont.)

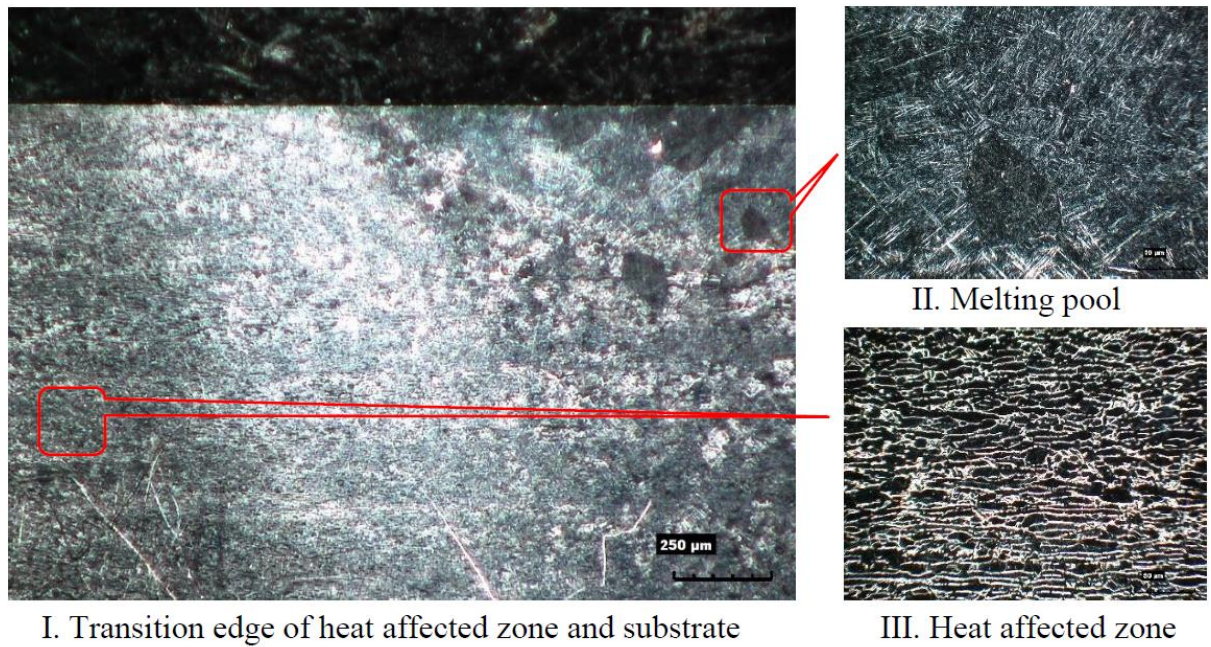


Figure 4.8 Sample microstructure of the repaired part. (c) Microstructure of sample 3.
(cont.)

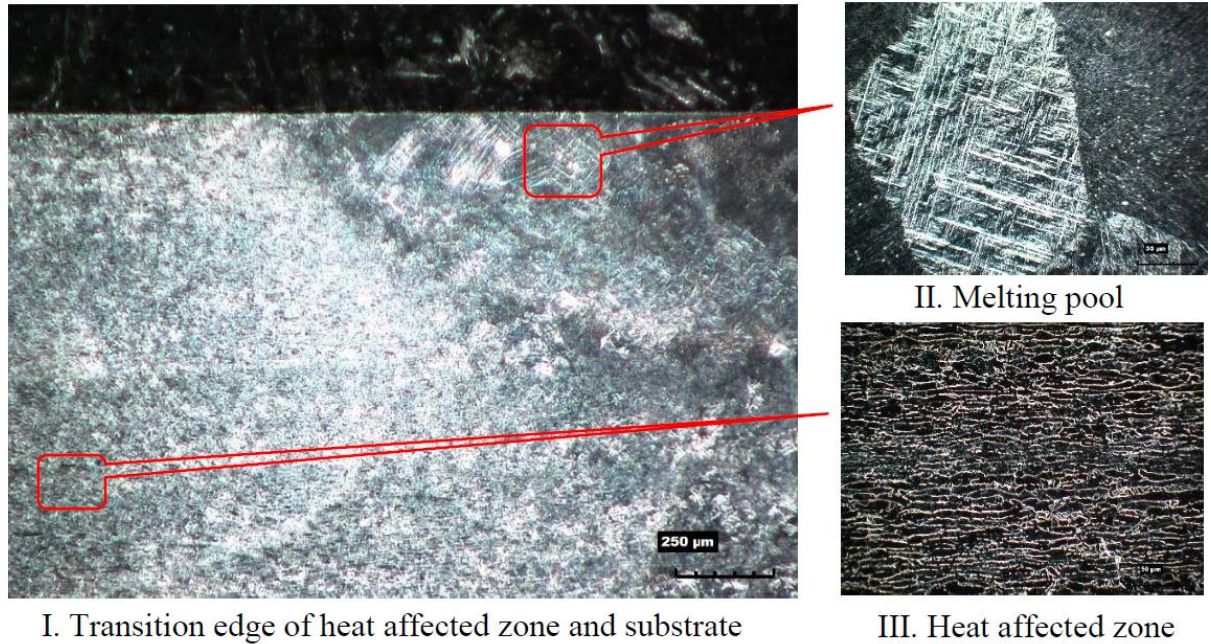


Figure 4.8 Sample microstructure of the repaired part. (d) Microstructure of sample 4.
(cont.)

5. CONCLUSION

In this paper, a smooth toolpath generation method is proposed for laser metal deposition. A parametric curve equation based on trigonometric functions is built to provide general solution for smooth connection or transition. Compared with arc or bi-arc solution, the parametric curve solution in this paper is a robust, flexible, and efficient solution for arbitrary 2D/3D toolpath connection or transition. It provides constant feedrate for depositing tool path. Meanwhile, the scale coefficient of the curve also makes the curve size controllable. Experiments were implemented for a patch deposition experiment and a component repair experiment with Ti-6Al-4V metal powder. The experimental results show that the smooth toolpath pattern can noticeably reduce porosity and improve the dimensional accuracy and surface roughness for laser metal deposition.

ACKNOWLEDGMENTS

This research was supported by National Science Foundation Grants IIP-1046492, CMMI-1301414, CMMI-1547042, GNK Aerospace, and Intelligent Systems Center and Material Research Center at Missouri University of Science and Technology. Their support is greatly appreciated.

REFERENCES

- [1] ASTM, *ASTM International Committee F42 on Additive Manufacturing Technologies, ASTM F2792–10 Standard Terminology for Additive Manufacturing Technologies*. 2009, ASTM: West Conshohocken, PA.
- [2] J. Edgar and S. Tint, *Additive Manufacturing Technologies: 3D Printing, Rapid Prototyping, and Direct Digital Manufacturing*. Johnson Matthey Technology Review, 2015. 59(3): p. 193-198.
- [3] F.W. Liou, et al. *Research and development of a hybrid rapid manufacturing process*. in *Proceedings of the Solid Freeform Fabrication Symposium*. 2001. Citeseer. p. 138-145.
- [4] L. Xue and M.U. Islam, *Laser consolidation-a novel one-step manufacturing process for making net-shape functional components*. 2006, DTIC Document.
- [5] V.K. Balla, et al., *Fabrication of compositionally and structurally graded Ti–TiO₂ structures using laser engineered net shaping (LENS)*. *Acta biomaterialia*, 2009. 5(5): p. 1831-1837.
- [6] F. Wang, J. Mei, and X. Wu, *Compositionally graded Ti6Al4V+ TiC made by direct laser fabrication using powder and wire*. *Materials & design*, 2007. 28(7): p. 2040-2046.
- [7] I. Kelbassa, et al. *Manufacture and repair of aero engine components using laser technology*. in *Proceedings of the 3rd Pacific International Conference on Application of Lasers and Optics*. 2008. p. 208-212.
- [8] J. Gao, et al., *Investigation of a 3D non-contact measurement based blade repair integration system*. *Aircraft Engineering and Aerospace Technology*, 2005. 77(1): p. 34-41.
- [9] N. Guo and M.C. Leu, *Additive manufacturing: technology, applications and research needs*. *Frontiers of Mechanical Engineering*, 2013. 8(3): p. 215-243.
- [10] P.M. Sammons, D.A. Bristow, and R.G. Landers, *Height dependent laser metal deposition process modeling*. *Journal of Manufacturing Science and Engineering*, 2013. 135(5): p. 054501.
- [11] E. Sabourin, S.A. Houser, and J. Helge Bøhn, *Adaptive slicing using stepwise uniform refinement*. *Rapid Prototyping Journal*, 1996. 2(4): p. 20-26.
- [12] R. Hope, R. Roth, and P. Jacobs, *Adaptive slicing with sloping layer surfaces*. *Rapid Prototyping Journal*, 1997. 3(3): p. 89-98.

- [13] J. Ruan, et al. *Automatic process planning of a multi-axis hybrid manufacturing system*. in *ASME 2002 International Design Engineering Technical Conferences and Computers and Information in Engineering Conference*. 2002. American Society of Mechanical Engineers. p. 965-971.
- [14] H. Zhang, et al. *Multi-axis path planning for hybrid plasma deposition and milling based on slicing characteristics*. in *International Conference on Intelligent Robotics and Applications*. 2008. Springer. p. 225-234.
- [15] Y.A. Jin, Y. He, and J.Z. Fu. *An adaptive tool path generation for fused deposition modeling*. in *Advanced Materials Research*. 2013. Trans Tech Publ. p. 7-12.
- [16] R. Liu, et al. *Stereo Vision Based Hybrid Manufacturing of Ti-6Al-4V in Component Repair Process*. in *2014 Annual International Solid Freeform Fabrication Symposium*. 2014. Austin, TX, USA. p. 1425-1431.
- [17] L. Ren, et al., *Three dimensional die repair using a hybrid manufacturing system*. Austin, TX, 2008.
- [18] Z. Zhao, et al., *Pocketing toolpath optimization for sharp corners*. Journal of materials processing technology, 2007. 192: p. 175-180.
- [19] Z. Lin, et al., *Smooth contour-parallel tool path generation for high-speed machining through a dual offset procedure*. The International Journal of Advanced Manufacturing Technology, 2015. 81(5-8): p. 1233-1245.
- [20] T.T. El-Midany, A. Elkeran, and H. Tawfik. *Toolpath pattern comparison: Contour-parallel with direction-parallel*. in *Geometric Modeling and Imaging--New Trends, 2006*. 1993. IEEE. p. 77-82.
- [21] W. Tiller and E.G. Hanson, *Offsets of two-dimensional profiles*. IEEE COMP. GRAPHICS APPLIC., 1984. 4(9): p. 36-46.
- [22] R. Rohmfeld, *IGB-offset for plane curves—loop removal by scanning of interval sequences*. Computer Aided Geometric Design, 1998. 15(4): p. 339-375.
- [23] S.C. Park and B.K. Choi, *Uncut free pocketing tool-paths generation using pairwise offset algorithm*. Computer-Aided Design, 2001. 33(10): p. 739-746.
- [24] J.-H. Kao and F.B. Prinz. *Optimal motion planning for deposition in layered manufacturing*. in *Proceedings of DETC*. 1998. p. 13-16.

- [25] S. Routhu, et al. *2-D path planning for direct laser deposition process*. in ASME 2010 International Design Engineering Technical Conferences and Computers and Information in Engineering Conference. 2010. American Society of Mechanical Engineers. p. 415-423.
- [26] L. Biagiotti and C. Melchiorri, *Trajectory planning for automatic machines and robots*. 2008: Springer Science & Business Media. 514.

PAPER

III. STEREO VISION-BASED REPAIR OF METALLIC COMPONENTS

Renwei Liu, Zhiyuan Wang, Todd Sparks, Frank Liou, and Cedo Nedic

Department of Mechanical and Aerospace Engineering

Missouri University of Science and Technology, Rolla, Missouri 65409, U.S.A.

GKN Aerospace, Hazelwood, Missouri 63042, U.S.A.

ABSTRACT

The work presented in this paper aimed to investigate a stereo vision-based hybrid (additive and subtractive) manufacturing process using direct laser metal deposition, CNC machining and in-process scanning to repair metallic components automatically. The focus of this work was to realize automated alignment and adaptive tool path generation that can repair metallic components after a single setup. Stereo vision was used to detect the defect area for automated alignment. After the defect is located, a laser displacement sensor is employed to scan the defect area before and after laser metal deposition. The scan is then processed by an adaptive algorithm to generate a tool path for repairing the defect. The hybrid manufacturing processes for repairing metallic component combine the advantages of free-form fabrication from additive manufacturing with the high-accuracy offered by CNC machining. A Ti-6Al-4V component with a manufacturing defect was repaired by the proposed process. Compared to previous research on repairing worn components,

introducing stereo vision and laser scanning dramatically simplifies the manual labor required to extract and reconstruct the defect area's geometry. This paper demonstrates an automated metallic component repair process by integrating stereo vision and a laser displacement sensor into a hybrid manufacturing system. Experimental results and microstructure analysis shows that the defect area could be repaired feasibly and efficiently with acceptable heat affected zone using the proposed approach.

Keywords: Additive Manufacturing, Stereo vision, Repair, Automation

1. INTRODUCTION

During the service life, components may be subject to corrosion, impacts, variable thermal cycles, stresses or other conditions that could cause defects or cracking [1]. Fatigue and stress cracks are common initiators of failures that cause high-performance and high-value components to be scrapped [1, 2]. On the other hand, defects such as milling ball indentation, cutter pull out may occur during manufacturing process. Since large quantities energy and capital are put into high-value components, discarding such parts is not a good option.

Conventional methodologies for repairing these components require several labor-intensive and operator skill-sensitive processes. Moreover, most of them have obvious disadvantages. For example, electron beam (EB) welding [3] needs a vacuum environment which is expensive and difficult to apply to larger parts. The depth and spread of deposited material are hard to control using the high velocity oxyfuel (HVOF) thermal spraying technique [4]. Tungsten inert gas (TIG) [5] is relatively easy to apply. However, it produces a lot of heat and causes high residual stresses, resulting in distortion and heat-related effects in the base metal.

In recent years, the use of laser metal deposition for repair has become a research hotspot. Pinkerton analyzed the direct laser metal deposition process for tool steel component repair in terms of the mass deposition rate, deposition microstructure, evidence of porosity, size of the heat-affected zone, and micro hardness [6]. His work provided evidence that this method can produce high-quality repairs but porosity can form at the boundaries between the original part and the added material. Graf analyzed the feasibility of using laser metal deposition for re-filling milled grooves for repairing stainless steel and

Ti-6Al-4V [7]). The deposition result showed no defects and good side-wall fusion, as long as the groove is wide enough for good powder jet accessibility. Dey studied the mechanical properties (UTS, YS, percentage elongation) of Ti-6Al-4V samples that were repaired using hybrid manufacturing [8]. The data from the tested samples showed an enhancement of properties of the repaired components. These above studies indicate that direct laser metal deposition can fill the defect area well within reasonable powder jet accessibility, and has a small and limited heat-affected zone compared with the conventional repair methodologies. The mechanical properties of repaired components can be even better than base material. Modern CNC technology offers a high-accuracy, high flexibility and effective process planning technique. Consequently, the effective combination of AM and CNC can be very powerful. The current state of the art consists of AM and CNC machining in the same manufacturing cell for hybrid manufacturing [9-11].

Although the introduction of automation has advanced repair productivity, quality, and reduced costly re-work on a stepwise basis, most repair processes still rely on manual initial and final inspection. This evokes researchers to make efforts to integrate the repair cycle (deposition/cladding, machining, scanning/inspection) into an automated process on one working platform. The studies that have been performed mainly on specific aspects of repairing worn out component are summarized below.

- Automated repair process. Gao proposed an automated repair system that contains digitizing, building up, machining, and inspection. A 3D digitizing system and welding/cladding process were integrated, and the worn blade could be detected automatically. However, the component needed to be transferred with the fixture to the CNC machine for the machining operation after the worn

blade was built up (Gao et al., 2005). Jason Jones developed an integrated production system that combines laser cladding, machining and in-process inspection in a single machine for flexible and lean remanufacturing. However, the system uses a touch probe to scan the defect, the alignment is not efficient, and it is difficult to access complex repair areas [12].

- Extraction and reconstruction of worn area. Zheng proposed a strategy to capture the geometry of the worn area by comparing the point cloud of the worn part with its nominal CAD model [13]. Gao proposed an adaptive solution to recreate the nominal geometry of an individual worn component using a reverse engineering-based surface extension approach to achieve an automated repair process using laser cladding/machining [14]. He and Li developed a curved surface extension approach to construct a three-dimensional shape of the worn area in blades using a CCD camera measurement system [15].

The previous studies focused on repairing worn components, especially on worn turbine blades. The main and crucial work is extracting and reconstructing the worn area by comparing it to its nominal CAD model and generating tool path for repair. Recently, Wang presented a stereo vision-based hybrid manufacturing process to produce fully dense metal parts with CNC level precision [16]. Bracun developed a stereo vision- based measuring system for online welding path inspection of the critical welds or weld deposits in multi-pass and repair welding [17]. Ryberg et al [18] adopted a stereo vision system to capture the weld joint for correcting off-line programmed nominal robot trajectories. This paper proposes a stereo vision-based hybrid manufacturing repair process to implement automated metallic components repair. The whole system integrates stereo vision, a laser

displacement sensor, laser metal deposition, and machining. The adoption of stereo vision allows the hybrid manufacturing system to quickly target the defect area boundary on the component. A precise laser displacement sensor is mounted to the hybrid manufacturing system and navigated to the defect area to scan this area before and after laser metal deposition process. Adaptive deposition and machining tool path is generated according to the scanned point cloud. The approach is applied to repairing metallic components with a defect caused during the manufacturing process. Compared with the worn turbine blade repair in the previous research, the approach in this paper doesn't need to scan the whole worn component, fit the scanned data with its nominal CAD model, or extract and reconstruct the worn area. Combining stereo vision and the laser displacement sensor dramatically simplifies the work for extracting and reconstructing the defect area for repair.

2. METHOD AND PROCESS

2.1.OVERVIEW OF AUTOMATED COMPONENT REPAIR PROCESS

Additive manufacturing has the capability of free-form fabrication, which is useful for component repair because the defect geometry on a component is usually arbitrary and random. As shown in Figure 2.1, hybrid manufacturing system includes two major systems: a laser metal deposition system and a CNC milling machine system. When using the hybrid manufacturing processes for component repair, the major problem is automation such as automated defect region detection and measurement, and alignment between the component and machine.

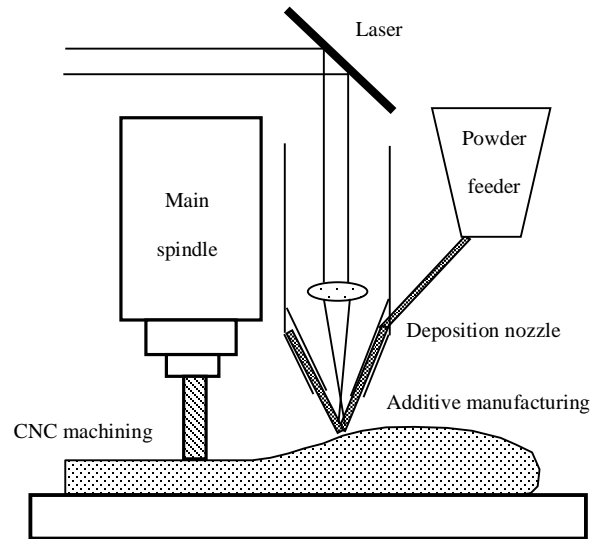


Figure 2.1 A hybrid manufacturing system: Additive manufacturing and CNC machining

This paper introduces a stereo vision-based hybrid manufacturing process [16] to realize automated metallic component repair. The automated component repair process

includes automated defect detection, alignment, scanning/inspection, adaptive tool path generation, and hybrid manufacturing. Figure 2.2 shows an overview of the process for stereo vision-based automated component repair. Stereo vision is used to detect the defect area of the component and align the component within the hybrid manufacturing system. After alignment, a laser displacement sensor is implemented to accurately scan the geometry of the defect. A deposition and machining tool path is then generated based on the scan. Finally, G-code of the deposition and milling tool path is imported to the hybrid manufacturing system to finish the repair work.

2.2.STEREO VISION AND CALIBRATION

Stereo vision is the extraction of 3D information from two different 2D images. The two main problems of stereo vision are stereo matching and reconstruction. As the linear camera model illustrated in Figure 2.3 (a) and (b), an ideal object point has two projections in two cameras' image planes. The problem with stereo matching is a correspondence problem: A projection point in the left image, correspondence problem is to find corresponding point in the right image. Stereo disparity d can be calculated based on stereo matching. Points in two dimensions can also be reprojected into three dimensions given their image coordinates and the camera intrinsic parameters. The reprojection matrix and equation can be expressed as [19]:

$$Q = \begin{bmatrix} 1 & 0 & 0 & -c_x \\ 0 & 1 & 0 & -c_y \\ 0 & 0 & 0 & f \\ 0 & 0 & -1/T_x & (c_x - c'_x)/T_x \end{bmatrix} \Rightarrow Q \begin{bmatrix} x \\ y \\ d \\ 1 \end{bmatrix} = \begin{bmatrix} X \\ Y \\ Z \\ W \end{bmatrix} \quad (1)$$

The 3D coordinates are then $(X/W, Y/W, Z/W)$. Here, (c_x, c_y) is the principal point as the left image's origin, f is the focal length, c'_x is the principal point x coordinate in the right image, T_x is the translation vector of stereo camera in the x direction, $d = x_l - x_r$ is the disparity (the coordinate difference between corresponding points in two 2D images.)

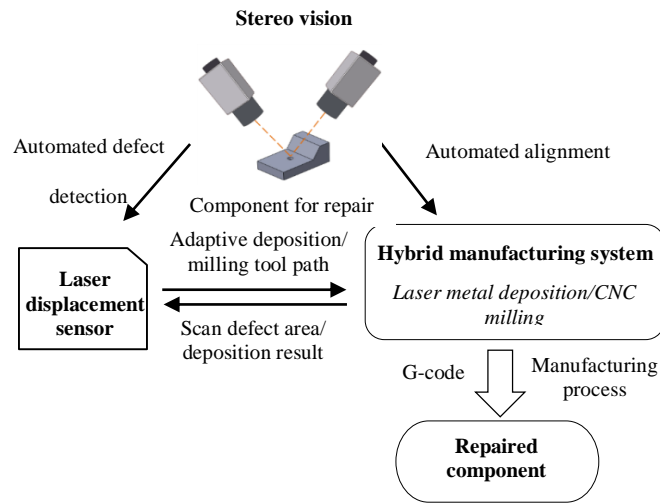


Figure 2.2 Process of automated component repair

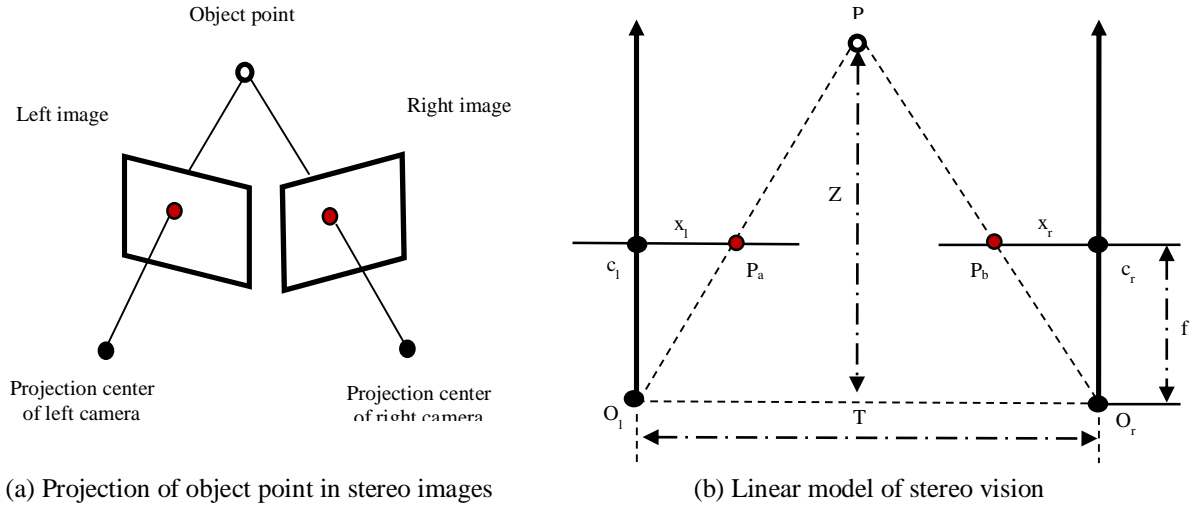


Figure 2.3 Principle of stereo vision

As we can see from equation (1), camera intrinsic and extrinsic parameters need to be calibrated to extract 3D information. The process of determining intrinsic and extrinsic camera parameters is camera calibration. The intrinsic parameters include focal length, principal point, and distortion parameters, while the extrinsic parameters are the rotation matrix and translation vector between left and right camera coordinate systems. As shown in Figure 2.4, a chessboard, which is viewed by the stereo camera at different viewing angles and distances, was adopted for calibration. The calibration method was developed by Zhang [20].

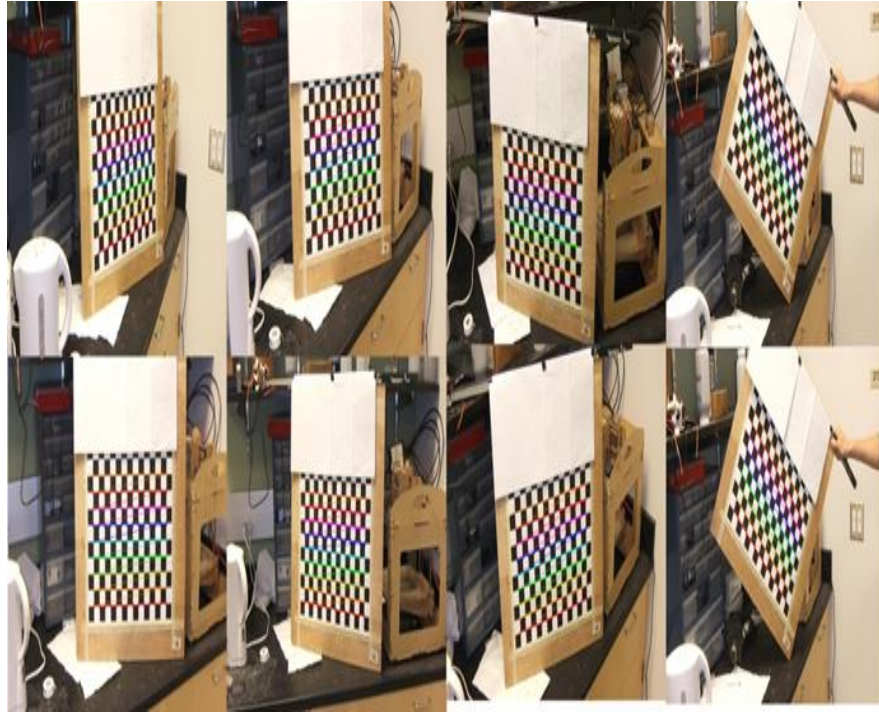


Figure 2.4 Chessboard viewing at different angles and distances by stereo vision camera with founded corners for calibration

2.3.AUTOMATED DEFECT DETECTION AND ALIGNMENT

After calibration, a stereo vision camera is used to obtain spatial information of the defect area. This includes two steps. The first step is automated boundary detection of the defect area in the camera coordinate system. The second step is aligning camera coordinate system and hybrid manufacturing coordinate system. Finally, the boundary information about the defect is transformed to a hybrid manufacturing coordinate system.

In order to automatically detect the defect, circle marks are put around the defect area, as shown in Figure 2.5. The marks allow the image processing algorithm to more easily identify the defect. And then 3D coordinates of circle marks in camera coordinate system can be calculated by stereo vision algorithm illustrated in Section 2.2. Figure 2.5 describes the automated defect detection process. Table 2.1 is the result of the 3D

measurement example above. By using stereo vision, we can see the measurement result is accurate enough (less 0.5mm error in this example) to target the defect area.

Table 2.1 An example of circle centers detection and 3D measurement by stereo vision

	Coordinates in stereo vision (Unit: mm)		Distance by stereo vision (Unit: mm)	Actual distance (Unit: mm)
P0	[25.01, -0.75, 123.74]	P0P1	9.12	9
P1	[25.36, 8.31, 124.76]	P1P2	15.32	15
P2	[40.65, 7.39, 124.24]	P2P3	9.41	9
P3	[38.38, -1.65, 125.53]	P3P0	13.52	13

The next step is to align camera coordinate system with the hybrid manufacturing coordinate system. Actually, alignment determines the transformation matrix, which includes the rotation matrix and translation vector between those two coordinate systems. The transformation matrix is a homogeneous transformation matrix for two Cartesian coordinate systems [21]. The following Equation (2) explain the method to calculate transformation matrix T_{cam}^{hm} . Four spatial positions, which are not in one plane on the hybrid manufacturing system, are used to calculate T_{cam}^{hm} . Read each coordinate of those four positions in hybrid manufacturing system and then calculate the corresponding coordinate of those four positions in the camera coordinate system by stereo vision.

$$\begin{bmatrix} P_{1x}^{hm} & P_{2x}^{hm} & P_{3x}^{hm} & P_{4x}^{hm} \\ P_{1y}^{hm} & P_{2y}^{hm} & P_{3y}^{hm} & P_{4y}^{hm} \\ P_{1z}^{hm} & P_{2z}^{hm} & P_{3z}^{hm} & P_{4z}^{hm} \\ 1 & 1 & 1 & 1 \end{bmatrix} = T_{cam}^{hm} * \begin{bmatrix} P_{1x}^{cam} & P_{2x}^{cam} & P_{3x}^{cam} & P_{4x}^{cam} \\ P_{1y}^{cam} & P_{2y}^{cam} & P_{3y}^{cam} & P_{4y}^{cam} \\ P_{1z}^{cam} & P_{2z}^{cam} & P_{3z}^{cam} & P_{4z}^{cam} \\ 1 & 1 & 1 & 1 \end{bmatrix}$$

$$\Leftrightarrow points^{hm} = T_{cam}^{hm} * points^{cam} \quad (2)$$

$$\Rightarrow T_{cam}^{hm} = points^{hm} * inv(points^{cam})$$

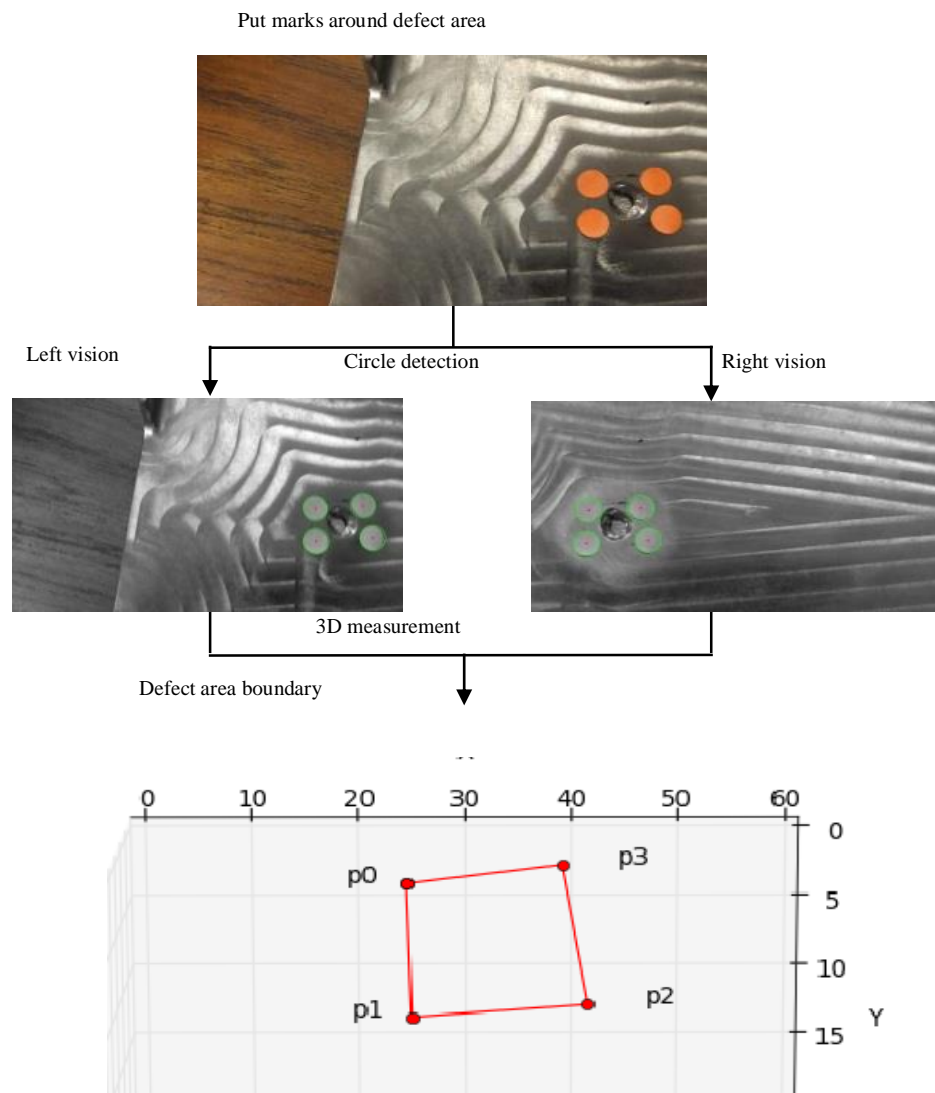


Figure 2.5 Automated defect detection in camera coordinate system

2.4.ADAPTIVE TOOL PATH GENERATION

During the whole repair process, stereo vision tells the hybrid manufacturing system where the defect area boundary is. The laser displacement sensor is then employed to scan the defect area precisely. It tells what the geometry of the defect area is. Even though stereo vision could do 3D reconstruction of the defect area, it is sensitive to the surface and viewing angle and requires a high computation cost for processing the required data. In contrast with stereo vision, the laser displacement sensor is more reliable, efficient and accurate. On the other hand, it is a non-contact measurement method, unlike the touch probe. The laser displacement sensor is commanded to scan the defect area based on the automated defect detection and alignment result. The zigzag scanning tool path is generated, and a scanned point cloud of the defect area is obtained as shown in Figure 2.6. In this paper, the adaptive tool path generation algorithm is developed for both deposition and machining. The whole algorithm is explained as follows:

Step 1: Set up deposition parameters such as layer thickness, deposition track width, overlap, and tolerance.

Step 2: Find the boundary in the Z axis and project the point cloud into parallel planes normal to the Z direction within the boundary.

Step 3: Use convex hull algorithm for each plane to find convex hull of those points in this plane as shown in Figure 2.7 (a).

Step 4: Adopt the raster tool path algorithm to generate the deposition tool path according to the convex hull as shown in Figure 2.7 (b).

Step 5: Repeat Steps 3 and 4 until the total paths for all layers are completed.

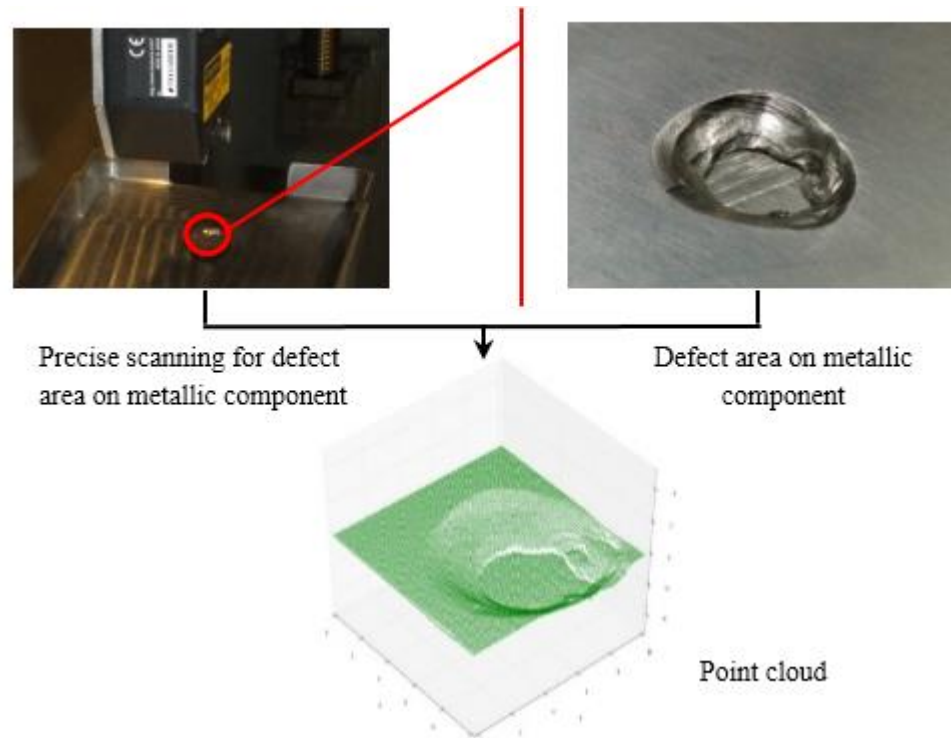


Figure 2.6 Precise scanning with laser displacement sensor and the scanned point cloud of defect area

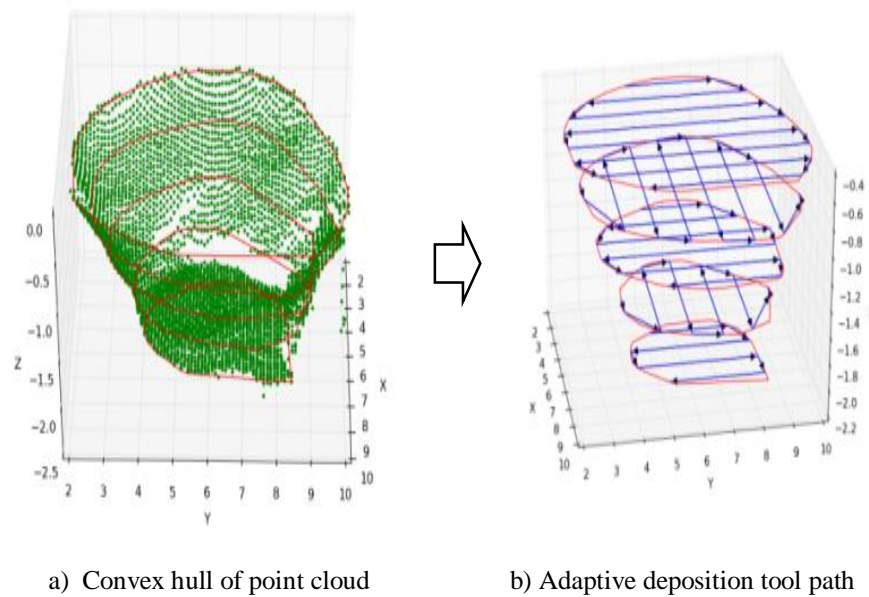


Figure 2.7 Adaptive tool path generation: convex hull extraction of point cloud and raster tool path generation

3. EXPERIMENTS

3.1. EXPERIMENT SETUP AND RESULT

A stereo vision based hybrid manufacturing system was built for metallic components repair as shown in Figure 3.1 [16]. A laser deposition machine (Rofin – Sinar 025) and a 5-axis CNC milling machine (Fadal VMC-3016L) were integrated for the hybrid manufacturing process [9]. A Fujifilm 3D camera with wireless data transfer for stereo vision and a laser displacement sensor were employed for precise scanning. The main software for the experiments, including camera calibration, image processing, 3D measurement, tool path generation, and post-processing were developed in the Python environment with libraries including StereoVision, OpenCV, Scipy, Matplotlib, etc.

Component repairing is usually implemented for recycling worn components like turbine blades. In this paper, we apply our approach to repair Ti-6Al-4V component with a manufacturing defect. The metal powder used for this experiment is a Ti-6Al-4V alloy with a size distribution of -60 +120 mesh. It has a chemical composition of 6.33% aluminum, 4.1% vanadium, 0.17% iron, 0.19% oxygen, and the remainder is titanium. The parameters in Table 3.1 were chosen for the laser metal deposition experiment, CNC milling operation and tool path generation for the Ti-6Al-4V component repair. Figure 3.2 shows the component with the defect mounted on the hybrid manufacturing system. After aligning and scanning the defect area, Ti-6Al-4V component was closed in a region with an argon shielding gas environment for laser metal deposition. The defect area on the Ti-6Al-4V component that needed to be repaired is shown in Figure 3.3 (a). After repair by the hybrid manufacturing process, the defect area was well-covered by the deposition

material, which can be seen in Figure 3.3 (b) and (c). And after machining process, we found the porosities in the deposition area as shown in Figure 3.3 (c). The deposition parameters may need to be optimized to eliminate porosity in the intermediate region for future study. In this paper, we focused on the automated alignment and adaptive tool path generation using stereo vision-based hybrid manufacturing process.

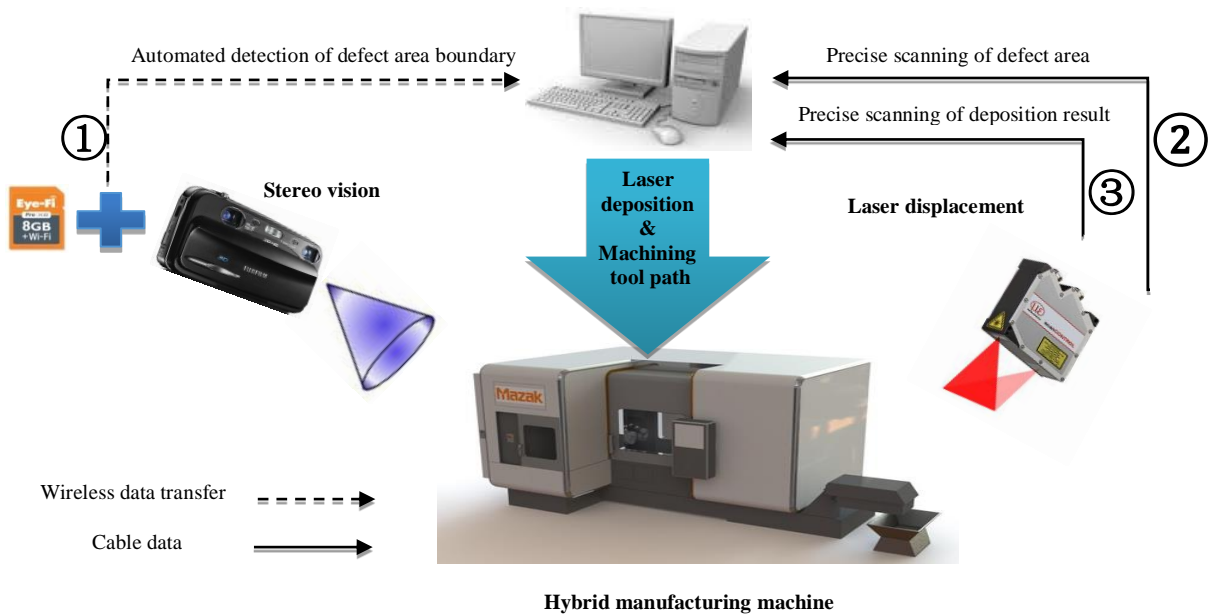


Figure 3.1 Stereo vision-based hybrid manufacturing system

Table 3.1 Parameters for laser metal deposition and milling experiment for Ti-6Al-4V component repair

Laser metal powder deposition		CNC milling	
Power feed rate	0.33 rpm	Milling tool	0.5 inch diameter
Scan speed	150 mm/min	Tool velocity	200 mm/min
Layer thickness	0.25 mm	Spindle speed	800 rpm
Track width	2 mm		
Track width overlap	0.5		



Figure 3.2 Ti-6Al-4V component be closed in shielding gas mounted on the hybrid manufacturing system

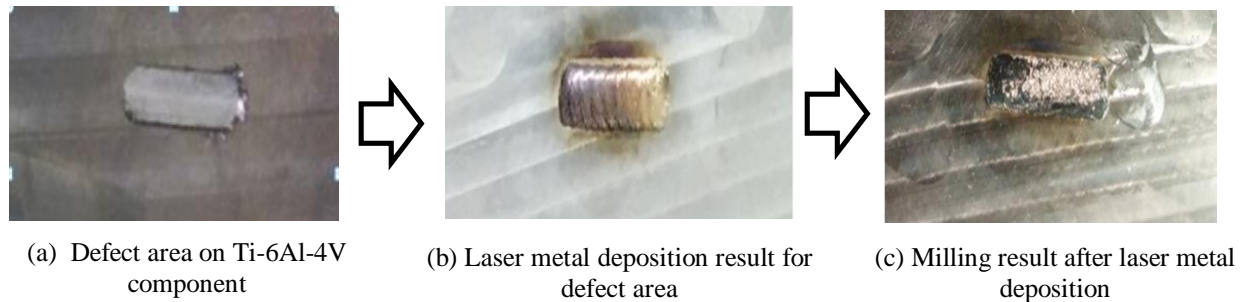
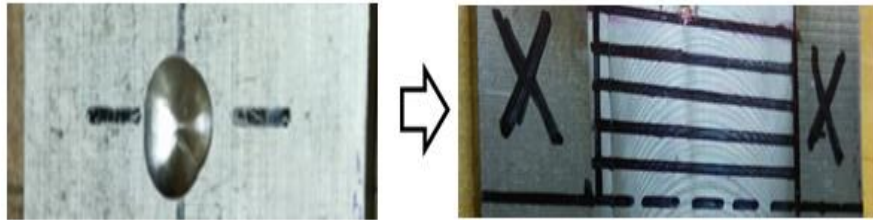


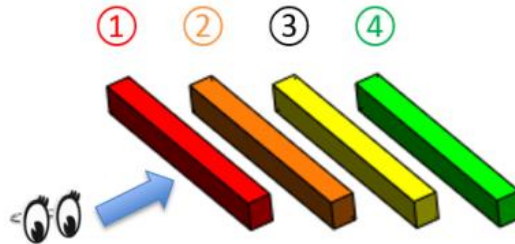
Figure 3.3 Experimental results by stereo vision-based hybrid manufacturing repair process

3.2. MICROSTRUCTURE STUDY OF REPAIRED SAMPLES

To study the microstructure of the repaired component, a sample with a ball indentation defect was repaired using proposed process as shown in Figure 3.4 (a). As Figure 3.4 (b) shows, this sample was cut into four slots using an EDM machine and polished to observe the metal microstructure of the heat-affected zone.



a) A repaired sample with ball indentation defect on Ti-6Al-4V component



b) View angle of four slots cutting for microstructure study

Figure 3.4 Repaired sample for microstructure study

As shown in Figure 3.5, the item number (① ② ③ ④) is the index for each sample slot and the item number (I II III) is the index for position of different feature on each cross section. I shows the transition edge of the heat affected area and the original material area. The edge is smooth between these two areas. II shows the center area of the laser metal deposition. This area is dominated by martensite. III shows the heat affected zone, which is below the melting pool, but this area is not melted during the deposition

process. These photos indicate that this automatic repair process could satisfy the requirements of restoring the geometry of the metallic component with a small heat affected zone and no obvious inner porosity.

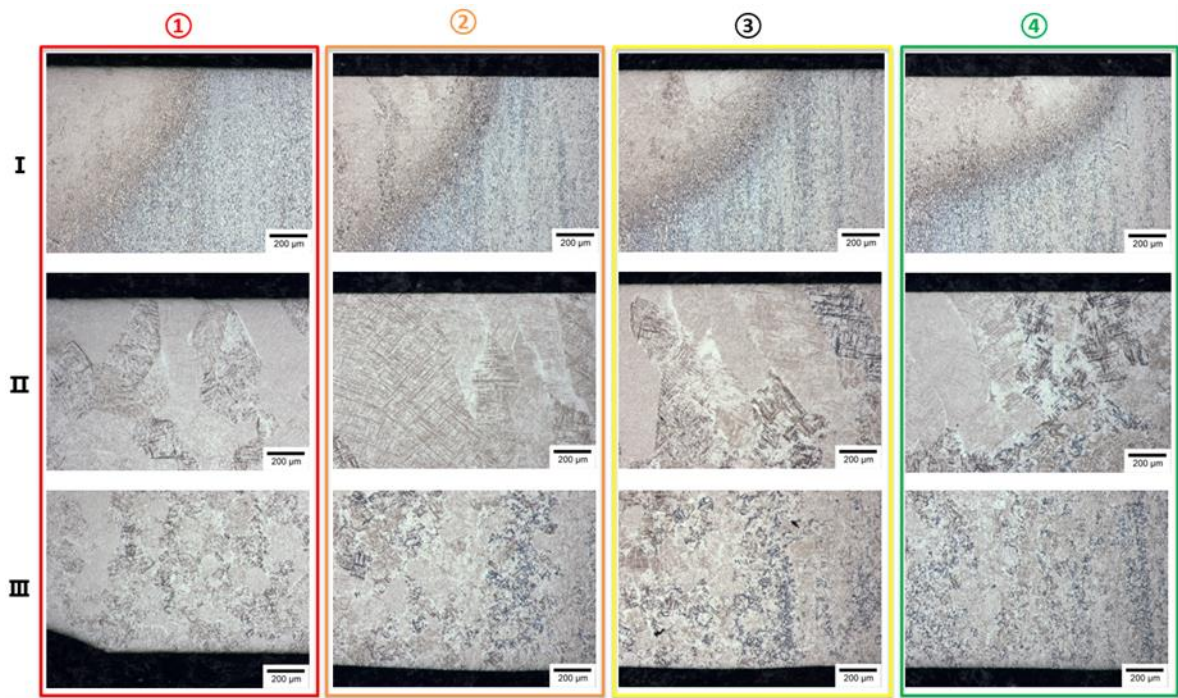


Figure 3.5 Microstructure study of repaired samples

4. CONCLUSIONS AND FUTURE WORK

In this paper, a stereo vision-based hybrid manufacturing process was proposed for repairing metallic components. This method combines the advantages of a one-setup process from AM and the high-accuracy offered by CNC machine. Stereo vision and a laser displacement sensor were employed to realize the automated defect boundary detection, alignment, precise scanning, and adaptive tool path generation. We applied this approach to repair metallic components with defects caused during the manufacturing process. Ti-6Al-4V component repairing experiment was performed to verify the proposed approach, and microstructure was studied for the repaired sample. The experiment results show that the proposed automated repair process is feasible and efficient for repairing metallic components. Compared with previous research on worn components, it dramatically simplifies the work for extracting and reconstructing the defect area geometry. However, deposition parameters may need to be optimized in the future experiments to achieve a good density quality of the repaired area. To implement the repair task at more flexible and larger scale, these processes will adopt a robot arm as the moving mechanism.

ACKNOWLEDGMENT

This research was supported by GKN Aerospace and National Science Foundation Grant IIP-1046492, Intelligent Systems Center and Material Research Center at Missouri University of Science and Technology. Their support is greatly appreciated.

REFERENCE

- [1] S.J. Balsone, M. Khobaib, and G.W. Watt. *Effect of stress on the hot corrosion of inconel 718*. in *114th Annual Meeting of the Metallurgical Society of AIME*. 1985. New York. p. 16.
- [2] G. Li, X. Li, and J. Wu, *Study of the thermal fatigue crack initial life of H13 and H21 steels*. *Journal of materials processing technology*, 1998. 74(1): p. 23-26.
- [3] M. Henderson, et al., *Nickel based superalloy welding practices for industrial gas turbine applications*. *Science and Technology of Welding & Joining*, 2004. 9(1): p. 13-21.
- [4] J. Tan, L. Looney, and M. Hashmi, *Component repair using HVOF thermal spraying*. *Journal of Materials Processing Technology*, 1999. 92-93: p. 203-208.
- [5] K. Nakata, et al., *Re-weldability of neutron-irradiated stainless steels studied by multi-pass TIG welding*. *Journal of Nuclear materials*, 2002. 307: p. 1578-1583.
- [6] A. Pinkerton, W. Wang, and L. Li, *Component repair using laser direct metal deposition*. *Proceedings of the Institution of Mechanical Engineers, Part B: Journal of Engineering Manufacture*, 2008. 222(7): p. 827-836.
- [7] B. Graf, A. Gumenyuk, and M. Rethmeier, *Laser metal deposition as repair technology for stainless steel and titanium alloys*. *Physics Procedia*, 2012. 39: p. 376-381.
- [8] N.K. Dey. *Additive manufacturing laser deposition of Ti-6Al-4V for aerospace repair application*. in *The Twenty-Fourth International Solid Freeform Fabrication Symposium*. 2013. Austin, TX, USA. p. 853-858.
- [9] F.W. Liou, et al. *Research and development of a hybrid rapid manufacturing process*. in *Proceedings of the Solid Freeform Fabrication Symposium*. 2001. Austin, TX, USA: Citeseer. p. 138-145.
- [10] J. Hur, K. Lee, and J. Kim, *Hybrid rapid prototyping system using machining and deposition*. *Computer-Aided Design*, 2002. 34(10): p. 741-754.
- [11] K. Boivie, et al. *Development of a Hybrid Manufacturing Cell; Integration of Additive Manufacturing with CNC Machining*. in *Twenty-Second Annual International Solid Freeform Fabrication Symposium-An Additive Manufacturing Conference*. 2011. Austin, TX, USA. p. 153-163.
- [12] J. Jones, et al. *Remanufacture of turbine blades by laser cladding machining and in-process scanning in a single machine*. in *Twenty-Third International Solid Freeform Fabrication Symposium in Austin*,. 2012. Austin,TX, USA. p. 821-827.

- [13] J. Zheng, Z. Li, and X. Chen, *Worn area modeling for automating the repair of turbine blades*. The International Journal of Advanced Manufacturing Technology, 2006. 29(9-10): p. 1062-1067.
- [14] J. Gao, et al., *An integrated adaptive repair solution for complex aerospace components through geometry reconstruction*. The International Journal of Advanced Manufacturing Technology, 2008. 36(11-12): p. 1170-1179.
- [15] J. He, L. Li, and J. Li. *Research of key-technique on automatic repair system of plane blade welding*. in *Control, Automation and Systems Engineering (CASE), 2011 International Conference on*. 2011. IEEE. p. 1-4.
- [16] Z. Wang, et al., *Stereo vision based hybrid manufacturing process for precision metal parts*. Precision Engineering, 2014. 42: p. 1-5.
- [17] D. Bračun and A. Sluga, *Stereo vision based measuring system for online welding path inspection*. Journal of Materials Processing Technology, 2015(223): p. 328-336.
- [18] A. Ryberg, et al. *Stereo vision for path correction in off-line programmed robot welding*. in *Industrial Technology (ICIT), 2010 IEEE International Conference on*. 2010. IEEE. p. 1700-1705.
- [19] G. Bradski and A. Kaehler, *Learning OpenCV: Computer vision with the OpenCV library*. 2008: O'Reilly Media, Inc.
- [20] Z. Zhang, *A flexible new technique for camera calibration*. Pattern Analysis and Machine Intelligence, IEEE Transactions on, 2000. 22(11): p. 1330-1334.
- [21] M.W. Spong, S. Hutchinson, and M. Vidyasagar, *Robot modeling and control*. Vol. 3. 2006: Wiley New York.

SECTION

2. CONCLUSION

Since each repair case is unique, manual operation is not only labor intensive but it is also not satisfactory in terms of time, cost, reliability, and accuracy. Therefore, it is very challenging and important to investigate and develop efficient methods and automated repair processes for best-fit and defect reconstruction, toolpath generation and manufacturing processes integration and automation when applying hybrid manufacturing for metallic component repair. A multi-feature fitting algorithm and a cross-section comparison based shape adaption algorithm are developed to best-fit the scanned mesh model of worn component and its nominal model and for defect reconstruction. The basic mathematical principle of rigid-body best-fit using features is presented. Multiple features can be constructed for feature-fitting according to the geometry of the component. Model level's feature fitting and cross-section level's feature-fitting are combined to best-fit the worn component model with its nominal model. The feature-fitting algorithm couples the least-square method and the density-outlier-detection method to approach the best-fit result. Compare with the point-to-surface and surface-to-surface, the feature-fitting method proposed in this dissertation is much efficient since features are fewer than point cloud or meshes. Meanwhile, the iteration of least-square method and density-based outlier detection method can eliminate the disturbance of defect geometry for the best-fit result. The shape adaption algorithm is based on the cross-section comparison and mesh trim for the defect reconstruction. A fracture 'point-line-surface' detection method is proposed to construct fracture surface of the worn component and then the fracture surface boundary is dilated to trim the nominal 3D model to obtain defect geometry. The whole methodology

is illustrated with typical components with different defects. For the broken components, a bearing house, bracket and turbine rotor are demonstrated using the methodology in this paper for symmetric or non-symmetric component, model level feature-fitting solely or with cross-section level-feature fitting to shows the flexibility and capability using the methodology for different geometries. For the deformed geometry, adaptive slicing is used for the curved blade feature construction. The adaptive slicing can be potentially used for the non-complete geometry's feature construction. As for the shape adaption, intersection surface on the nominal model and deformed model is used to obtained the deformed geometry and missed geometry for defect reconstruction.

In order to improve the deposition quality for metallic component fabrication and repair, a smooth toolpath generation method is proposed and implemented for laser metal deposition. A parametric curve equation based on trigonometric functions is built to provide general solution for smooth connection or transition. Compared with arc or bi-arc solution, the parametric curve solution is a robust, flexible, and efficient solution for arbitrary 2D/3D toolpath connection or transition. It provides constant feedrate for depositing toolpath. Meanwhile, the scale coefficient of the curve also makes the curve size controllable. Experiments were implemented for a patch deposition experiment and a component repair experiment with Ti-6Al-4V metal powder. The experimental results show that the smooth toolpath pattern can noticeably reduce porosity and improve the dimensional accuracy and surface roughness for laser metal deposition.

To integrate and automate the hybrid manufacturing processes for repair, a stereo vision-based hybrid manufacturing process was investigated and developed for repairing metallic components. This method combines the advantages of a one-setup process from

AM and the high-accuracy offered by CNC machine. Stereo vision and a laser displacement sensor were employed to realize the automated defect boundary detection, alignment, precise scanning, and adaptive tool path generation. We applied this approach to repair metallic components with defects caused during the manufacturing process. Ti-6Al-4V component repairing experiment was performed to verify the proposed approach, and microstructure was studied for the repaired sample. The experiment results show that the proposed automated repair process is feasible and efficient for repairing metallic components. Compared with previous research on worn components, it dramatically simplifies the work for extracting and reconstructing the defect area geometry.

The overall outcomes of this dissertation addressed several key issues which challenging the application of hybrid manufacturing for metallic component repair. It covers the processes from worn area modeling, toolpath generation, repair system integration and automation. The algorithm design for worn area modeling provides efficient and robust algorithm for worn component with different kinds of geometries and defects. And the smooth toolpath generation method improves the deposition evenness to obtain better dimensional accuracy and reduce the porosities. In addition, the stereo-vision based automated repair processes which integrate laser metal deposition, CNC machining, 3D scanning and adaptive toolpath generation into one single platform to improve the efficiency and reduce the manual operation for repair. The algorithms, methodologies, and processes developed in this dissertation also can be extended for the additive manufacturing, manufacturing and measurement automation, and part inspection.

VITA

Renwei Liu was born in Qiyang county, Yongzhou City, Hunan province, China. He received his Bachelor of Science degree in Mechanical Engineering in July 2009 from Shandong University, Jinan city, Shandong province, China. In July 2012, he received his Master of Science degree in Manufacturing System Information Engineering from Shandong University. In May 2017, he received his Doctor of Philosophy in Mechanical Engineering from Missouri University of Science and Technology, Rolla, Missouri, USA. His research interests include repair, additive manufacturing, hybrid manufacturing and CAD/CAM. During his Ph.D. study, he authored and co-authored seven journal papers, one book chapter, and four conference papers.